A Late Cretaceous-Eocene Geomagnetic Polarity Time Scale (MQSD20) that steadies spreading rates on multiple mid-ocean ridge flanks

Alberto Malinverno[1], Keegan W. Quigley[2], Alice Staro[3], and Jérôme Dyment[4]

[1]Lamont-Doherty Earth Observatory of Columbia University
[2]Brown University
[3]Università Statale di Milano
[4]Institut de Physique du Globe de Paris & CNRS, Sorbonne Paris Cité

November 23, 2022

Abstract

Magnetic anomalies over mid-ocean ridge flanks record the history of geomagnetic field reversals, and the width of magnetized crustal blocks can be combined with absolute dates to generate a Geomagnetic Polarity Time Scale (GPTS). We update here the current GPTS for the Late Cretaceous-Eocene (chrons C33-C13, ˜84-33 Ma) by extending to several spreading centers the analysis that originally assumed smoothly varying spreading rates in the South Atlantic. We assembled magnetic anomaly tracks from the southern Pacific (23 ship tracks), the northern Pacific (35), the southern Atlantic (33), and the Indian Ocean (55). Tracks were projected onto plate tectonic flow line, and distances to magnetic polarity block boundaries were estimated by fitting measured magnetic anomalies with a Monte Carlo algorithm that iteratively changed block model distances and anomaly skewness angles. Distance data from each track were then assembled in summary sets of block model distances over 13 ridge flank regions. We obtained a final MQSD20 GPTS with another Monte Carlo algorithm that iteratively perturbs ages of polarity chron boundaries to minimize the variability of spreading rates over all ridge flanks and fit an up-to-date set of radioisotopic dates. The MQSD20 GPTS highlights a major plate motion change at ˜47 Ma, when spreading rates decreased in the Indian Ocean as India collided with Eurasia while spreading rates increased in the South Atlantic and Northern Pacific and the Hawaii-Emperor seamount chain changed its orientation.

A Late Cretaceous-Eocene Geomagnetic Polarity Time Scale (MQSD20) that steadies spreading rates on multiple mid-ocean ridge flanks

A. Malinverno[1], K. W. Quigley[2], A. Staro[3*], and J. Dyment[4]

[1]Lamont-Doherty Earth Observatory of Columbia University, Palisades, New York, USA.
[2]Brown University, Providence, Rhode Island, USA.
[3]Dipartimento di Scienze della Terra, Università Statale di Milano, Italy.
[4]Université de Paris, Institut de Physique du Globe de Paris, CNRS, Paris, France.

Corresponding author: Alberto Malinverno (alberto@ldeo.columbia.edu)

*Current address: Department of Earth and Environment, Boston University, Boston, Massachusetts, USA.

Key Points:

- Estimated magnetic polarity block model distances over 13 ridge flank regions (Indian Ocean, S. and N. Pacific, S. Atlantic).
- Constructed a GPTS for chrons C33-C13 that minimizes global spreading rate variations and fits radioisotopic dates.
- At ~47 Ma, spreading rates decrease in the Indian Ocean (India-Eurasia collision) and increase in the N. Pacific (Hawaii-Emperor bend).

Abstract

Magnetic anomalies over mid-ocean ridge flanks record the history of geomagnetic field reversals, and the width of magnetized crustal blocks can be combined with absolute dates to generate a Geomagnetic Polarity Time Scale (GPTS). We update here the current GPTS for the Late Cretaceous-Eocene (chrons C33-C13, ~84-33 Ma) by extending to several spreading centers the analysis that originally assumed smoothly varying spreading rates in the South Atlantic. We assembled magnetic anomaly tracks from the southern Pacific (23 ship tracks), the northern Pacific (35), the southern Atlantic (33), and the Indian Ocean (55). Tracks were projected onto plate tectonic flow line, and distances to magnetic polarity block boundaries were estimated by fitting measured magnetic anomalies with a Monte Carlo algorithm that iteratively changed block model distances and anomaly skewness angles. Distance data from each track were then assembled in summary sets of block model distances over 13 ridge flank regions. We obtained a final MQSD20 GPTS with another Monte Carlo algorithm that iteratively perturbs ages of polarity chron boundaries to minimize the variability of spreading rates over all ridge flanks and fit an up-to-date set of radioisotopic dates. The MQSD20 GPTS highlights a major plate motion change at ~47 Ma, when spreading rates decreased in the Indian Ocean as India collided with Eurasia while spreading rates increased in the South Atlantic and Northern Pacific and the Hawaii-Emperor seamount chain changed its orientation.

Plain Language Summary

As the Earth's magnetic field reversed its polarity during geological time, seafloor spreading created a series of magnetized blocks on mid-ocean ridge flanks that give rise to magnetic anomalies, field highs and lows measured by survey ships. These reversal records are combined with age ties from radioisotopic dating to construct a Geomagnetic Polarity Time Scale (GPTS) that lists the ages of magnetic field reversals. Our study updates the GPTS in the Late Cretaceous-Eocene (~84-33 million years ago) by minimizing the variation of spreading rates in the southern Atlantic, Indian, southern and northern Pacific Oceans using an up-to-date set of 154 ship tracks. By providing independent age information, the new GPTS will aid the developing discipline of astrochronology, which is based on the correlation of sediment cycles with astronomical cycles in the Earth's orbit and spin axis orientation. The new GPTS also refines the global history of spreading rates and highlights a major change at about 47 million years ago. At that time, seafloor spreading in the Indian Ocean slowed down as India collided with Eurasia while spreading became faster in the northern Pacific, coinciding with a bend in the orientation of the Hawaii-Emperor seamount chain.

1 Introduction

1.1 Background

Accurate time scales are crucial to establish the history of tectonic plate motion and to determine past rates of change documented in the rock record. Magnetic measurements and radioisotopic dating of volcanic rocks led to the discovery of globally synchronous reversals of the Earth's magnetic field (see the historical overview of Glen, 1982). The history of these reversals was recorded by magnetic anomalies created by seafloor spreading on mid-ocean ridge flanks, allowing for the development of a geomagnetic polarity time scale (GPTS; acronyms used in this paper are listed in Table 1).

Table 1. List of acronyms.

Acronym	Definition
BMD	Magnetic polarity block model distance
CAPANT	Capricorn-Antarctica plate boundary
CAPSOM	Capricorn-Somalia plate boundary
CK95	GPTS of Cande & Kent (1992, 1995)
CV	Coefficient of variation (standard deviation/mean)
GPTS	Geomagnetic polarity time scale
GTS12	GPTS in Geological Time Scale 2012 (Gradstein et al., 2012)
MCMC	Markov chain Monte Carlo
MQSD20	GPTS of this paper
PACANT	Pacific-Antarctica plate boundary
PACBAN	Pacific-Bellingshausen-Antarctica plate boundary
PACFAR	Pacific-Farallon plate boundary
PACFAV	Pacific-Farallon-Vancouver plate boundary
PACVAN	Pacific-Vancouver plate boundary
SAMAFR	South America-Africa (Nubia) plate boundary

The first GPTS was based on the C-sequence (Late Cretaceous-present) magnetic anomalies in the South Atlantic with the assumption of a constant spreading rate determined by a single age tie at 3.35 Ma (Heirtzler et al., 1968). Cande and Kent (1992, 1995) derived an improved CK95 GPTS for the last 83 Ma that accounted for long-term variations in spreading rate. CK95 was based on a reference South Atlantic plate tectonic flow line defined by a detailed set of finite plate rotations (Cande et al., 1988). The finite rotations provided nine key magnetic polarity block model distances (BMDs); more detail was inserted from the relative widths of polarity blocks representative of uniform seafloor spreading in the South Atlantic and in faster spreading ridges of the North Pacific and Central Indian Oceans. The CK95 GPTS was obtained by interpolating BMDs between nine radioisotopic dates with a cubic spline, thus ensuring a smooth temporal variation in South Atlantic spreading rates. The South Atlantic BMDs of CK95 have been the key source of information from marine magnetic anomalies for time scale development over more than two decades, and have been repeatedly used to construct GPTSs with different age constraints (e.g., Ogg & Smith, 2004; Vandenberghe et al., 2012; Wei, 1995).

The last few decades also saw the development of astrochronology, based on sediment cycles that record Milankovitch periodicities in the Earth's orbit and the orientation of its spin axis (Hinnov & Hilgen, 2012). In the Neogene portion of the most recent GTS12 GPTS (Hilgen et al., 2012), information from marine magnetic anomalies has been mostly replaced by astronomical dating of sedimentary sections with a reliable magnetostratigraphy.

Astronomical dating of older intervals, however, is more challenging, and the marine magnetic anomaly record remains an independent source of information for time scale development. For example, in the Paleogene the GTS12 GPTS uses a combination of astrochronology (66-53 Ma and 37-23 Ma) and a GPTS based on the CK95 BMDs (53-37 Ma), and there are significant discrepancies in the Eocene and Paleocene (Vandenberghe et al., 2012). Many astrochronology studies used the CK95 GPTS to initially match sedimentary cycles with astronomical periods (Herbert et al., 1995; Röhl et al., 2003), to decide between alternative tuning options (Röhl et al., 2003), to estimate the duration of hiatuses (Pälike et al., 2001), to provide age constraints to floating time scales (Jovane et al., 2010), and to compare ages and durations of magnetic polarity chrons (Billups et al., 2004; Herbert et al., 1995; Husson et al., 2011; Westerhold et al., 2007, 2008, 2017).

1.2 Updating late Cretaceous-Eocene BMDs and GPTS

The two objectives of our work are 1) to generate a global set of BMDs obtained independently over a number of spreading centers and 2) to construct an updated GPTS that minimizes global spreading rate variations. The global record of magnetic anomalies has grown since it was analyzed by Cande and Kent (1992), and detailed finite plate rotations have been determined over a number of spreading centers besides the South Atlantic. We examine here a large data set of 154 marine magnetic anomaly ship tracks projected onto plate tectonic flow lines computed from finite rotations. The resulting up-to-date global BMDs will inform astrochronology interpretations and constrain GPTS construction.

A drawback of the CK95 GPTS is that the calculated spreading rates in other ocean basins vary more erratically than in the South Atlantic (e.g., Figure 42 of Cande & Kent, 1992). Huestis and Acton (1997) pointed out that there is no reason to expect that spreading rates change smoothly at one particular location while they are more variable at all other ridges. They argued for a "least favoritism" approach where a GPTS is constructed by minimizing the variation in spreading rates in all the magnetic anomaly profiles examined. Independent astronomical dating supports this suggestion: Wilson (1993) and Krijgsman et al. (1999) found that the spreading rates implied by astrochronology in the last ~10 Ma were less variable than rates computed from the CK95 GPTS. Astronomical age control steadies the spreading rates (see also Baksi, 1994; Gordon, 1993; Langereis et al., 1994), indicating that minimizing spreading rate fluctuations over several spreading centers will provide a more reliable GPTS.

We concentrate here on the late Cretaceous-Eocene (chrons C33-C13, ~84-33 Ma), which is the interval where the CK95 GPTS is most uncertain. Cande and Kent (Cande & Kent, 1992 p. 13,947-48) recognized that the "largest uncertainties in our new time scale are probably for the anomaly spacings in the late Cretaceous and early Cenozoic. This corresponds to the time interval of the most rapid change in spreading rate […] in the South Atlantic […] when there is the most potential for error." This time interval is also of great interest in paleoenvironmental studies, as it records a long-term warming trend in the Paleocene, a sudden warming event at the Paleocene-Eocene thermal maximum followed by a series of hyperthermals, the greatest Cenozoic warmth in the Early Eocene, and the onset of the cooling trend that resulted in the formation of the Antarctic ice sheets at the Eocene/Oligocene boundary (Vandenberghe et al., 2012; Zachos et al., 2001, 2008). An accurate time scale is critical to advance our understanding of these climatic changes. As noted earlier, astronomical calibration of the Late Cretaceous-Eocene is still in flux, and an updated GPTS would be most useful to constrain time scale development in this critical interval.

The GPTS we generate uses only an up-to-date set of radioisotopic dates and includes no astrochronological constraints. Our goal is to provide independent information to astrochronology that can help resolve time scale inconsistencies, for example around chrons C23 (Vandenberghe et al., 2012; Westerhold et al., 2017) and C28 (Hilgen et al., 2010; Westerhold et al., 2008). A GPTS that fully integrates information from the global marine magnetic anomaly record, radioisotopic dates, and astrochronology will be a future development.

In this paper, we first introduce the Monte Carlo procedure applied to obtain BMDs that match measured magnetic anomalies and a GPTS that fits radioisotopic dates and minimizes global spreading rate variations. We then describe the fundamental data used here for GPTS construction: BMDs obtained over 13 mid-ocean ridge flank regions and radioisotopic dates tied to magnetostratigraphy. A new MQSD20 GPTS is constructed following the approach previously applied by Malinverno et al. (2012) to the M-sequence magnetic anomalies (Late Jurassic-Early Cretaceous). We conclude by comparing the ages and chron durations in MQSD20 with those in existing GPTSs, exploring the impact of the newly obtained BMDs on testing astrochronology interpretations, and describing a global change in spreading rates at ~47 Ma, when India collided with Eurasia and the Hawaii-Emperor seamount chain changed its orientation.

1.3 Nomenclature

We use here the CK95 sequence of chrons to define a series of magnetic polarity crustal blocks that recorded field reversals, and do not consider magnetic field excursions such as tiny wiggles (Cande & Kent, 1992). Following general nomenclature (Gee & Kent, 2007; Opdyke & Channell, 1996), C-sequence magnetic anomalies are named 13n, 13r, etc., and the corresponding polarity chrons are C13n, C13r, etc. Magnetic polarity is denoted by "n" for normal and "r" for reversed. Boundaries of magnetic polarity blocks and chrons are denoted by appending "y" for the young boundary and "o" for the old (e.g., C13ny is the young end of chron C13n). We denote years of age as "a" and years of duration as "yr," with the usual prefixes (e.g., 1 Ma = 1 million years ago). We report uncertainties as one or two standard deviations (1σ or 2σ, respectively).

2 Markov chain Monte Carlo sampling

To determine best values and uncertainties of BMDs estimated from ship track magnetic anomalies and of a GPTS that minimizes the global variation of spreading rates, we use here a Markov chain Monte Carlo (MCMC) algorithm (Brooks et al., 2011; Gilks et al., 1996). The algorithm asymptotically generates a sample of model parameter vectors $\mathbf{m}$ (e.g., distances to polarity block boundaries) that are distributed as in a target probability density function (PDF). We follow a Bayesian formulation, where the target distribution is a posterior PDF proportional to the product of a prior PDF $p(\mathbf{m})$ that quantifies prior information on the parameters and a likelihood function $p(\mathbf{d}|\mathbf{m})$ that quantifies how closely the measured data in a vector $\mathbf{d}$ (e.g., magnetic anomalies) are fitted by data predicted by the parameters in $\mathbf{m}$. The posterior PDF is given by Bayes' rule as

$$p(\mathbf{m}|\mathbf{d}) = k\, p(\mathbf{m})\, p(\mathbf{d}|\mathbf{m}), \qquad (1)$$

where k is a normalizing constant. In our application, the parameter vector $\mathbf{m}$ also contains "hyperparameters," which are additional variables that affect the solution and are not closely constrained a priori (Gelman et al., 2004; Malinverno & Briggs, 2004). An example is the variance of the misfit between predicted and measured data, which is needed to define the likelihood function but is not known beforehand.

We apply here the Metropolis-Hastings MCMC algorithm (Chib & Greenberg, 1995; Metropolis et al., 1953), which performs a random walk in the space of the parameter vector $\mathbf{m}$. The algorithm first proposes a candidate parameter vector $\mathbf{m}^*$ that is a small perturbation on the current value of the parameters. The construction of candidate parameter vectors needs to perform a random walk that can go from any point to any other point in the space of the parameters. At each step of the random walk, the proposed candidate is accepted or rejected with a probability that depends on the ratio of the posterior PDF for the current and the candidate parameter vector (so that the normalizing constant k in Equation 1 is irrelevant). By applying this simple accept/reject rule, it can be shown that the resulting Markov chain will asymptotically sample the posterior PDF. This MCMC procedure has been widely used in geophysical inverse problems (e.g., Malinverno, 2002; Malinverno & Leaney, 2005; Piana Agostinetti & Malinverno, 2010; Sambridge & Mosegaard, 2002; Sen & Stoffa, 2013).

We implement here the simple MCMC scheme proposed by Mosegaard and Tarantola (1995). If the random walk that samples candidate model vectors is designed to sample the prior PDF of the parameters, then the probability of accepting the candidate simply depends on the ratio of the likelihoods. The sampling algorithm starts by defining an initial model parameter vector $\mathbf{m}$ and calculating its likelihood $p(\mathbf{d}|\mathbf{m})$. Each sampling iteration is as follows:

- Sample a candidate $\mathbf{m}^*$ following a random walk that samples the prior PDF of the model parameter vector;
- Compute the candidate likelihood $p(\mathbf{d}|\mathbf{m}^*)$;
- Accept the candidate with probability

$$P_{\mathrm{acc}} = \min\,[1, p(\mathbf{d}|\mathbf{m}^*) \,/\, p(\mathbf{d}|\mathbf{m})]; \qquad (2)$$

- If the candidate is accepted, set $\mathbf{m} = \mathbf{m}^*$ and $p(\mathbf{d}|\mathbf{m}) = p(\mathbf{d}|\mathbf{m}^*)$; if not, $\mathbf{m}$ and the likelihood stay the same.

Finally, to ensure that the parameter values output by the MCMC algorithm converge to sampling the posterior PDF, we compare the results of multiple independent sampling chains as suggested by Gelman et al. (2004). The detailed implementation of the MCMC sampling algorithm is described in the Supporting Information.

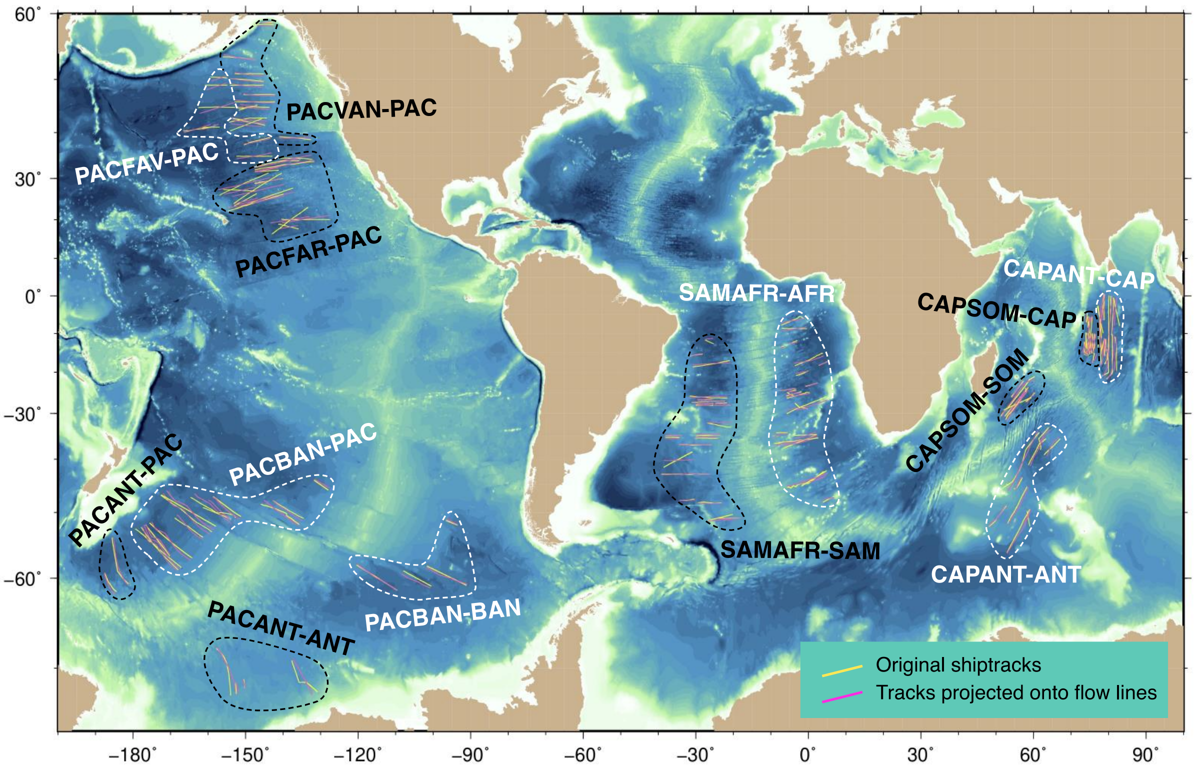

Figure 1. Location map of 153 ship tracks with measured magnetic anomalies over 13 ridge flank regions. Original tracks and tracks projected onto nearby plate tectonic flow lines are both shown. Detailed maps are in the Supporting Information.

3 Marine magnetic anomaly data

This section describes how magnetic anomaly ship tracks were processed to obtain distances along plate tectonic flow lines to the boundaries of modeled magnetic polarity blocks. These block model distances (BMDs) are the input to construct a GPTS that minimizes the global variability of spreading rates.

Ship tracks were selected over thirteen mid-ocean ridge flank regions that recorded anomalies between 13ny and 34ny at intermediate and fast spreading rates and that had previously determined sequences of finite rotation poles (Figure 1 and Table 2). The main source of magnetic anomaly data was the NOAA-NCEI archive of trackline geophysical measurements (NOAA National Geophysical Data Center, 1977), supplemented by additional surveys in the Indian Ocean (Yatheesh et al., 2019). We chose tracks that approximately followed the direction of plate motion, did not go over seamounts, and did not cross the fracture zones and ridge axis discontinuities listed in the Global Seafloor Fabric and Magnetic Lineation Data Base (Matthews et al., 2011). Each track was projected on a nearby plate tectonic flow line defined by the finite rotation poles. This projection ensured that the BMDs determined on each projected track were measured along the direction of plate motion.

Initial BMDs in each projected track were determined from the position of key anomaly picks taken from the Global Seafloor Fabric and Magnetic Lineation Data Base (Seton et al., 2014). These key anomaly picks were then interpolated assuming piecewise constant spreading rates to obtain a set of BMDs for all the polarity blocks defined by the CK95 GPTS. Anomalies predicted in each track by initial BMDs and an initial anomaly skewness angle (Schouten & McCamy, 1972) were compared to the measured anomalies. The initial BMDs and skewness were manually adjusted to improve the overall fit to the measured data. Tracks or track segments that did not display an unambiguous correlation to the overall predicted anomaly pattern were discarded, resulting in a data set of 154 original and projected tracks (location maps are in the Supporting Information).

Table 2. Ridge flank regions with distances to polarity block boundaries and sources for finite plate rotations used to define flow lines.

Ocean basin	Ridge flank region	Tracks	Chron boundaries	Sources for finite rotations
S. Atlantic	SAMAFR-AFR	23	C13ny--C34ny	(Müller et al., 1999)
	SAMAFR-SAM	22	C13ny--C34ny	
Indian Ocean	CAPSOM-CAP	18	C18n.1ny--C30ny	(Cande et al., 2010; Cande & Patriat, 2015)
	CAPSOM-SOM	7	C13ny--C29ry	
	CAPANT-CAP	17	C13ny--C34ny	
	CAPANT-ANT	9	C13ny--C34ny	
S. Pacific	PACANT-PAC	2	C20ny--C33ry	(Croon et al., 2008; Wright et al., 2016)
	PACANT-ANT	4	C13ny--C30ny	
	PACBAN-PAC[a]	13	C13ny--C33ry	
	PACBAN-BAN[a]	4	C13ny--C28ny	
N. Pacific	PACFAR-PAC	14	C18n.2ry--C33ny	(Wright et al., 2015, 2016)
	PACFAV-PAC[b]	7	C24n.1ny--C33ny	
	PACVAN-PAC	14	C13ny--C24n.1ny	
	Total	154		

[a]Finite rotations for Pacific-Bellingshausen plate pair (anomalies 33-28) followed by Pacific-Antarctica (26-13). [b]Finite rotations for Pacific-Farallon plate pair (anomalies 34-25) followed by Pacific-Vancouver (24-13).

The manually adjusted skewness angle and BMDs for each track were then iteratively modified by a Markov chain Monte Carlo (MCMC) algorithm to obtain a sample of BMDs that fit the magnetic anomaly data. The MCMC algorithm also adjusted a set of nodes that define an interpolated multiplier for the magnetic anomaly amplitudes (Figure 2). Accounting for the variation of anomaly amplitudes along tracks proved necessary to prevent the Monte Carlo algorithm from occasionally sampling unrealistically narrow polarity blocks. If the amplitudes of the predicted anomalies were not adjusted, a narrow, low-amplitude anomaly could only be fitted by making the corresponding polarity block narrower than it should be. The final product of Monte Carlo sampling is a best value (the sample average) and uncertainty (the sample standard deviation) of the BMDs in each projected track. Details on the MCMC procedure and figures with the geographic locations of block model boundaries in the original tracks are in the Supporting Information.

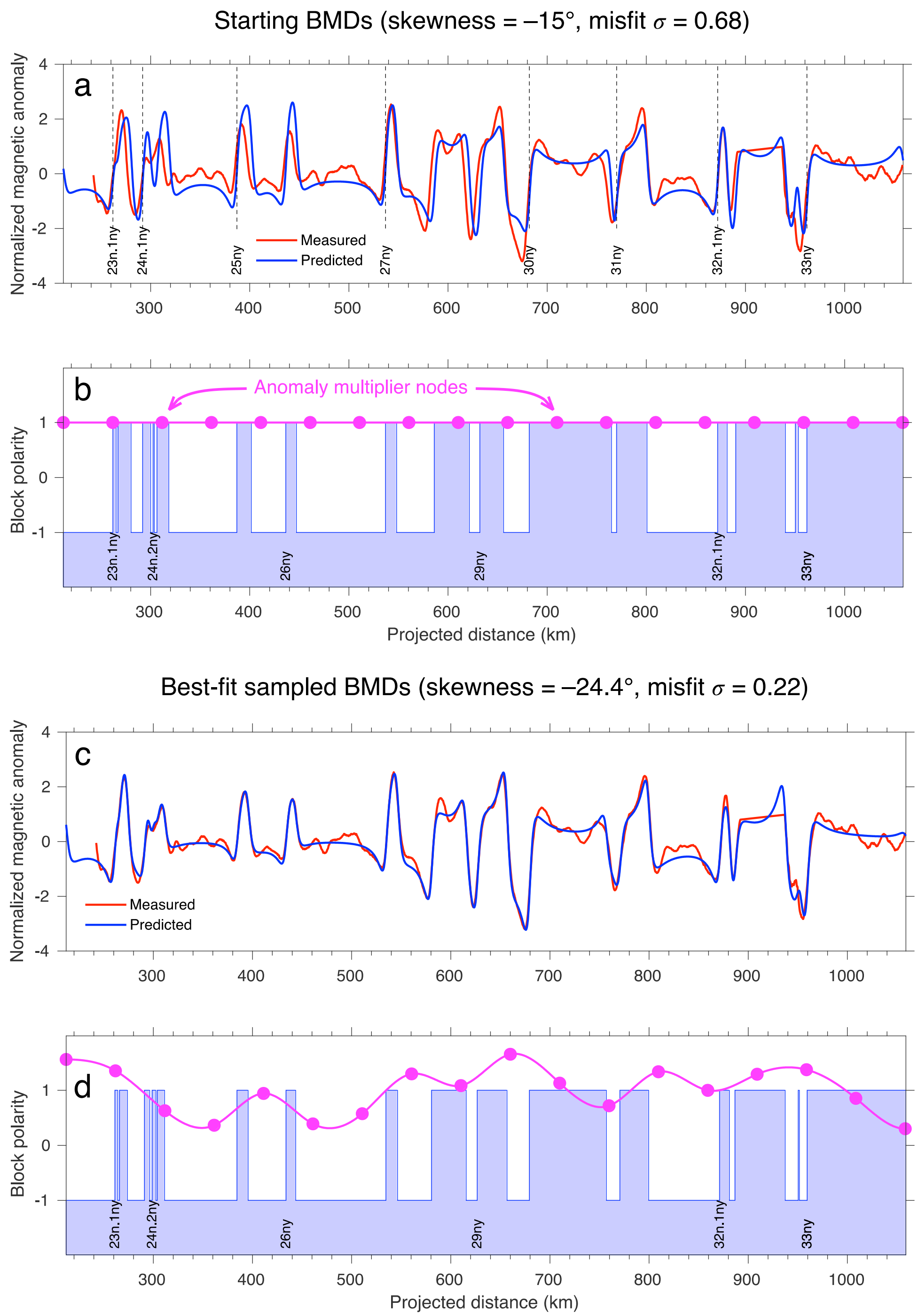

Figure 2. Comparison measured-predicted magnetic anomalies for starting BMDs (a, b) and best-fit BMDs sampled by a MCMC algorithm (c, d). The projected ship track is nbp9604_PAC_a in the PACVAN-PAC ridge flank region. The vertical dashed lines in (a) show the starting BMDs manually adjusted to approximately fit measured anomalies. The MCMC algorithm modifies iteratively the starting BMDs, the anomaly multiplier nodes, and the skewness angle to maximize the fit between measured and predicted anomalies.

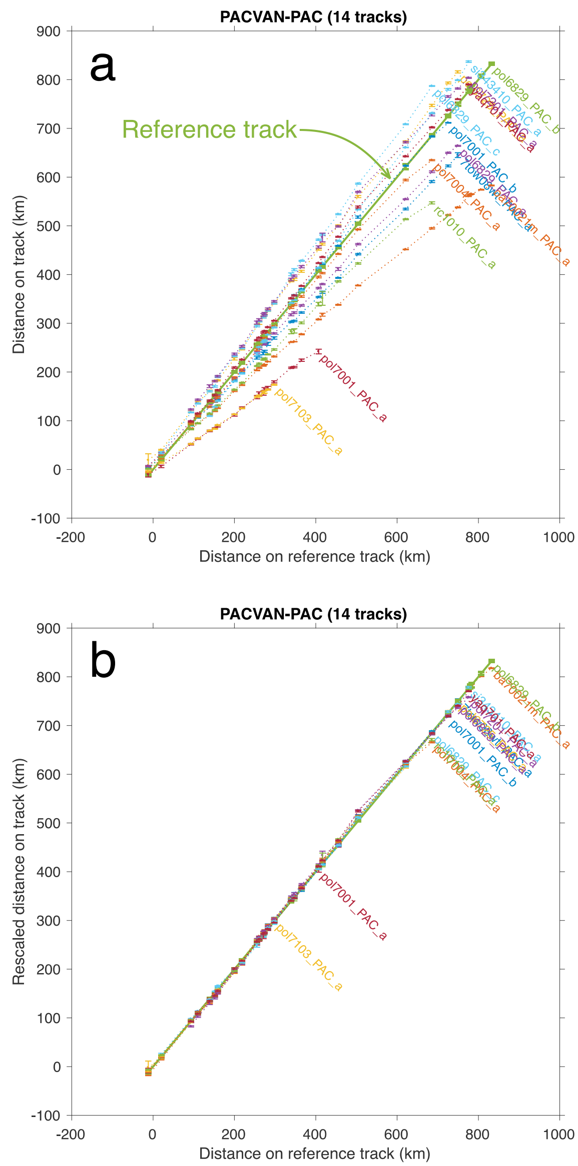

Figure 3. BMDs in projected ship tracks over a ridge flank region (PACVAN-PAC in the figure) plotted versus BMDs in a reference track show a systematic variation due to the change in spreading rate at different distances from the plate rotation pole (a). When rescaled to fit the spreading rate in the reference track, BMDs are consistent and can be averaged to obtain a summary BMD for the whole ridge flank region (b).

We then obtained summary BMDs over each of the 13 ridge flank regions listed in Table 2 by rescaling and averaging the BMDs estimated in each projected track. Rescaling the BMDs accounts for the systematic variation of local spreading rates as a function of the distance between the track and the plate rotation poles (Figure 3). The rescaling was based on a reference projected track in each ridge flank region. This reference track was either a single long track or multiple tracks that spanned the full range of anomalies recorded over the ridge flank region. The BMDs estimated in each of the other projected tracks were rescaled with a least-squares fit so that the average spreading rate in the interval covered by the track was the same as in the matching interval in the reference track. This simple rescaling resulted in a consistent set of BMDs in each ridge flank region (see Figure 3 for an example). The best value for the ridge flank region BMDs was set to the median of the rescaled BMDs on each track. We used the median because it is a central value estimator that is not affected by occasional outliers. The uncertainty of the ridge flank region BMDs was quantified from the standard deviation of the rescaled BMDs for each track. The standard deviation will be increased by outliers, but this is a useful characteristic as it will decrease the influence on GPTS construction of BMDs that contain outliers and are poorly determined.

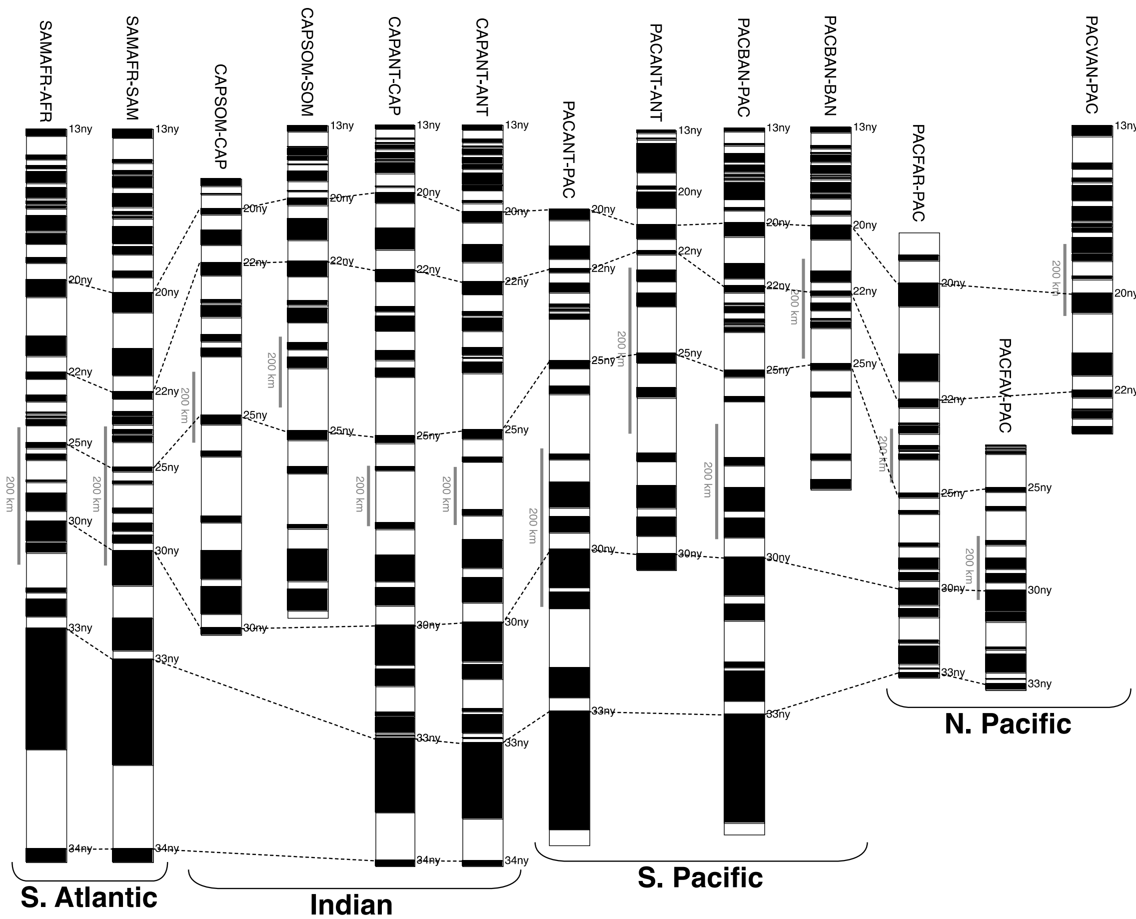

Figure 4. Summary block model distances in the 13 ridge flank regions used for GPTS construction.

Finally, we deleted from the summary BMDs polarity blocks narrower than 2 km. Narrow polarity blocks are poorly recorded by magnetic anomalies generated by a source layer whose top is at ~4.5 km water depth in 33 Ma crust (Parsons & Sclater, 1977). The width of these narrow blocks is mostly constrained by the distances to adjacent polarity block boundaries and does not provide independent information. The summary BMDs for 13 ridge flank regions are illustrated in Figure 4. Files listing the 154 tracks used here, the final positions and BMDs in each of the original and projected tracks, and the summary BMDs for each of the 13 ridge flank regions are available in two open access data publications (Malinverno et al., 2019a, 2019b).

4 Radioisotopic dates

The radioisotopic dates used here (Table 3) are from Table 28.1 of GTS12 (Vandenberghe et al., 2012) with a few modifications. GTS12 reports both a radioisotopic dating uncertainty and a stratigraphic position uncertainty expressed as a fraction of the stratigraphic thickness of the polarity chron (assumed here to represent two standard deviations). For GPTS construction, we then assigned to each radioisotopic date a total uncertainty from the sum of the variances due to radioisotopic dating uncertainty and stratigraphic uncertainty. The temporal uncertainty due to stratigraphic uncertainty was calculated as the product of the dimensionless stratigraphic uncertainty times the duration of the respective chron in CK95.

Table 3. Radioisotopic dates used to constrain the MQSD20 GPTS, modified after Table 28.1 of Vandenberghe et al. (2012).

Chron	Radioisotopic date		Stratigraphic position		Chron	Date uncert.	Total date
	Date (Ma)	Uncert. (2σ, Ma)	Up from base	Uncert. (2σ)	duration in CK95 (Ma)	due to stratigr. uncertainty (2σ, Ma)	uncertainty (2σ, Ma)
C13r [a]	34.8	0.2	0.19	0.1	1.11	0.11	0.23
C20n	43.35	0.5	0.1	0.1	1.253	0.13	0.52
C21n	46.24	0.5	0.75	0.1	1.642	0.16	0.53
C21r	48.41	0.21	0.1	0.1	1.131	0.11	0.24
C22n	48.96	0.33	0.45	0.1	0.677	0.07	0.34
C24n.1n	52.93	0.23	0	0.05	0.299	0.01	0.23
C24n.3r [b]	55.48	0.12	0.5	0.1	2.557	0.26	0.28
C24n.3r [b]	55.785	0.075	0.375	0.05	2.557	0.13	0.15
C26r	59.39	0.3	0.9	0.05	3.009	0.15	0.34
C28r	64.73	0.12	0.9	0.1	0.342	0.03	0.12
C29n	64.94	0.12	0.9	0.05	0.769	0.04	0.13
C29r	65.611	0.15	0.8	0.05	0.833	0.04	0.16
C29r [c]	65.84	0.12	0.57	0.05	0.833	0.04	0.13
C29r	65.99	0.12	0.5	0.05	0.833	0.04	0.13
C33n [d]	79.84	0.5	0	0.1	5.456	0.55	0.74
C33r [d]	83.6	0.5	0	0.1	3.925	0.39	0.64

[a] Average of two dates in C13r with updated stratigraphic positions (see Supplementary Information for details). [b] Chron was listed as C24r in Table 28.1 of Vandenberghe et al. (2012); it corresponds to C24n.3r in CK95 and in the nomenclature used in this paper. [c] A date of 66.28 Ma reported in Table 28.1 of Vandenberghe et al. (2012) for the same stratigraphic position does not correspond to a date in the original reference (Swisher et al., 1993) and was omitted. [d] Stratigraphic uncertainty was not reported in Table 28.1 of Vandenberghe et al. (2012), and was set conservatively as the maximum given elsewhere (0.1).

The two radioisotopic dates in chron C13r listed in Table 28.1 of GTS12 have been averaged to a single date (first row of Table 3). These dates were obtained in the Massignano quarry stratotype section from biotite-rich clayey layers of possible volcanic origin (Odin et al., 1991). GTS12 used a Fish Canyon sanidine age of 28.201 Ma to recalculate the original Ar/Ar radioisotopic dates as 34.4 ± 0.2 Ma (14.7 m stratigraphic height in Massignano quarry section, 0.4 up from base of C13r, 2σ uncertainty) and 35.2 ± 0.2 Ma. (12.7 m stratigraphic height, 0.14

up from base). We referred these dates to the stratigraphic framework of a drill core located about 110 m south of the Massignano stratotype section (Lanci et al., 1996). The drill core samples were taken every 12-15 cm, a much more detailed sampling interval than that possible in the Massignano outcrop, where strong weathering makes it difficult to obtain closely spaced, pristine samples. The C13r interval in the drill core was clearly established between stratigraphic depths of 14.2 m and 24.8 m (Figure 6 of Lanci et al., 1996). Using the conversion in Figure 3 of Lanci et al. (1996), the predicted stratigraphic height of C13r in the quarry section is 11.7 to 22.3 m. This estimate is in close agreement with the location of reversely magnetized samples in the outcrop (Figure 9 of Lowrie & Lanci, 1994). Based on the high-resolution magnetostratigraphy in the drill core, the stratigraphic positions of the two dates in C13r become 0.28 and 0.09 up from base.

If taken at face value, the two dates indicate a duration of C13r that is (35.2 – 34.4)/(0.28 – 0.09) = 4.21 Ma, which is almost four times the duration of C13r in CK95 (1.11 Ma). A >4 Ma duration of C13r also conflicts with the average sedimentation rate of 10.6 m/Ma estimated from astrochronology in the Massignano section (Brown et al., 2009, p. 123). As the C13r interval in Massignano is 9 to 10.6 m thick (Lanci et al., 1996; Montanari et al., 1993), the estimated sedimentation rate implies a duration of ~1 Ma.

Using directly the two C13r dates listed in GTS12 with the stated small uncertainties of 0.2 Ma will unduly bias the duration of C13r in the GPTS. To avoid this, we simply averaged the two dates (34.8 Ma) and located the average age midway between the two stratigraphic positions (0.19 up from the base of C13r). We did not change the radioisotopic date uncertainty, but increased the 2σ stratigraphic position uncertainty (0.05 in GTS12) to half the range of the two original dates, which is $(0.28 - 0.09) / 2 \approx 0.1$.

5 The MQSD20 GPTS

We obtain a new MQSD20 GPTS with a MCMC algorithm that generates a large ensemble of GPTSs. This ensemble will be asymptotically distributed as in the posterior PDF of Equation 1, and is used to calculate a reference GPTS and quantify its posterior uncertainty. Full details of the MCMC procedure are in the Supporting Information, and here we illustrate how the sampling proceeds when the GPTS is constrained by different types of information (Figure 5).

Figure 5a shows the progress of MCMC sampling if spreading rate variations are ignored and the data vector **d** in the likelihood function of Equation 1 only contains a set of radioisotopic dates (Table 3). The sampling starts from a perturbed version of the CK95 GPTS and proceeds by iteratively changing chron boundary ages, accepting or rejecting such changes as in the Metropolis acceptance probability of Equation 2. The sampled GPTSs fit the radioisotopic dates within their uncertainty, but the chron boundary ages and durations in intervals between radioisotopic age ties are uncostrained and extremely variable (e.g., between about 66 Ma and 80 Ma).

Figure 5b shows the MCMC sampling progress when the data vector **d** in the likelihood function of Equation 1 includes both radioisotopic dates and the BMDs estimated in each of the 13 ridge flank regions (Figure 4). In this case, the likelihood function is greater if the GPTS implies a smaller variation of spreading rates on each ridge flank (which depend on the BMDs). The variability of the sampled chron ages between radioisotopic age ties is much less than in Figure 5a, as it is constrained by the need to minimize spreading rate fluctuations. The final sample of GPTSs used to derive MQSD20 is constructed by combining the results of ten independent sampling chains such as that in Figure 5b (see the Supporting Information).

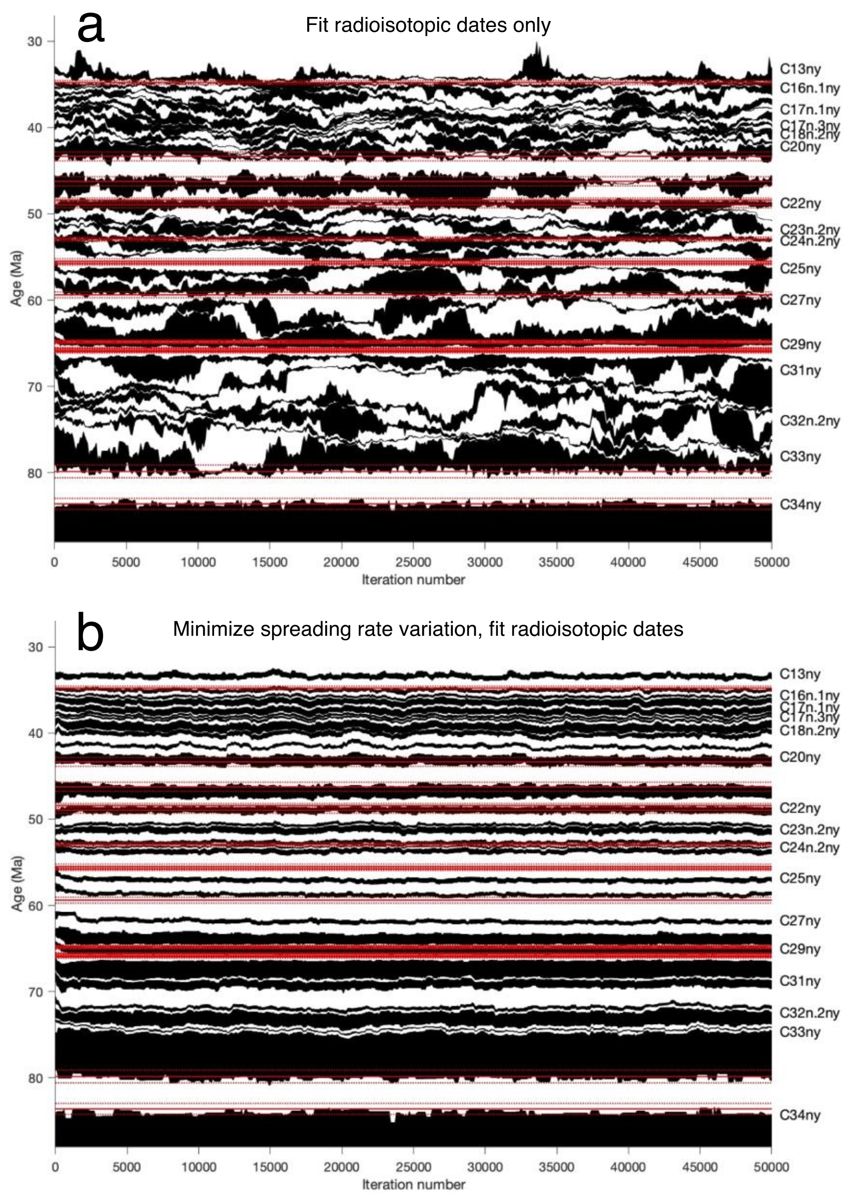

Figure 5. Progress of MCMC sampling of a GPTS. Each column in the images displays the GPTS sampled at the respective iteration number (black indicates normal and white reversed chrons). Solid red lines show radioisotopic dates and dotted red lines bracket their 2σ uncertainty (Table 3). Sampling is constrained to fit only the radioisotopic dates (a) or to fit radioisotopic dates while minimizing spreading rate variability over 13 ridge flank regions (b).

The MQSD20 chron boundary ages, chron durations, and respective uncertainties are in Table 4 and Figure 6. The reference GPTS chron boundary ages and chron durations are the average values of the ensemble obtained by MCMC sampling. GPTS uncertainties are quantified from the standard deviations of chron ages and durations in the ensemble. Near age ties, the uncertainties in the GPTS chron boundary ages are smaller than the uncertainties of the radioisotopic dates themselves (Figure 6), reflecting the additional constraints given by spreading rate information.

Table 4. MQSD20 GPTS ages, chron durations, and respective uncertainties.

Chron	End age (Ma)		Duration (Ma)		Chron	End age (Ma)		Duration (Ma)	
	Age	Uncert. (1σ)	Duration	Uncert. (1σ)		Age	Uncert. (1σ)	Duration	Uncert. (1σ)
C13n	33.076	0.178	0.599	0.102	C24n.1n	52.520	0.102	0.372	0.057
C13r	33.675	0.135	1.200	0.080	C24n.1r	52.892	0.091	0.187	0.041
C15n	34.875	0.112	0.324	0.053	C24n.2n	53.079	0.094	0.143	0.039
C15r	35.199	0.121	0.428	0.062	C24n.2r	53.222	0.096	0.232	0.041
C16n.1n	35.627	0.132	0.236	0.048	C24n.3n	53.455	0.097	0.514	0.063
C16n.1r	35.863	0.139	0.191	0.042	C24n.3r	53.969	0.104	2.855	0.160
C16n.2n	36.054	0.144	0.674	0.084	C25n	56.824	0.092	0.503	0.054
C16n.2r	36.728	0.161	0.322	0.053	C25r	57.327	0.100	1.220	0.091
C17n.1n	37.049	0.166	0.692	0.084	C26n	58.547	0.111	0.417	0.047
C17n.1r	37.741	0.183	0.193	0.040	C26r	58.963	0.109	2.677	0.128
C17n.2n	37.934	0.183	0.216	0.041	C27n	61.640	0.121	0.440	0.047
C17n.2r	38.150	0.185	0.137	0.040	C27r	62.080	0.120	1.201	0.089
C17n.3n	38.287	0.185	0.189	0.038	C28n	63.280	0.104	1.226	0.098
C17n.3r	38.477	0.186	0.359	0.059	C28r	64.506	0.044	0.343	0.034
C18n.1n	38.835	0.188	0.898	0.110	C29n	64.849	0.040	0.775	0.043
C18n.1r	39.734	0.202	0.164	0.059	C29r	65.623	0.039	0.789	0.067
C18n.2n	39.897	0.199	0.469	0.075	C30n	66.412	0.058	1.985	0.171
C18n.2r	40.366	0.202	1.014	0.111	C30r	68.397	0.179	0.288	0.058
C19n	41.380	0.192	0.338	0.060	C31n	68.685	0.188	0.913	0.104
C19r	41.718	0.187	0.917	0.099	C31r	69.598	0.213	2.124	0.168
C20n	42.634	0.176	1.109	0.105	C32n.1n	71.722	0.257	0.316	0.058
C20r	43.744	0.161	2.307	0.151	C32n.1r	72.038	0.263	0.325	0.066
C21n	46.050	0.149	1.438	0.132	C32n.2n	72.363	0.267	1.558	0.142
C21r	47.488	0.126	1.081	0.111	C32n.2r	73.921	0.294	0.399	0.071
C22n	48.569	0.091	0.717	0.088	C32r.1n	74.319	0.304	0.123	0.040
C22r	49.286	0.108	1.132	0.117	C32r.1r	74.442	0.304	0.353	0.069
C23n.1n	50.418	0.134	0.288	0.057	C33n	74.795	0.307	5.320	0.317
C23n.1r	50.705	0.135	0.183	0.049	C33r	80.115	0.272	3.902	0.314
C23n.2n	50.888	0.134	0.699	0.090	C34n	84.017	0.274		
C23n.2r	51.587	0.130	0.933	0.102					

The chron boundary ages and chron durations of MQSD20 are compared to those of CK95 (Cande & Kent, 1992, 1995) and of GTS12 (Ogg, 2012) in Figure 7. The differences in chron boundary ages with CK95 reach ~1 Ma for chrons C24 and earlier (ages ≥ 53 Ma), and are partly due to radioisotopic age recalibration. As MQSD20 used the same radioisotopic age ties as GTS12, the age differences are smaller (0.5 Ma or less), though they exceed the 2σ age uncertainty of MQSD20 for chrons C25-C29 (ages ~56-65 Ma). Chron duration differences are at most 0.3 Ma with respect to both CK95 and GTS12, and are generally within the the 2σ uncertainty of the chron durations in MQSD20.

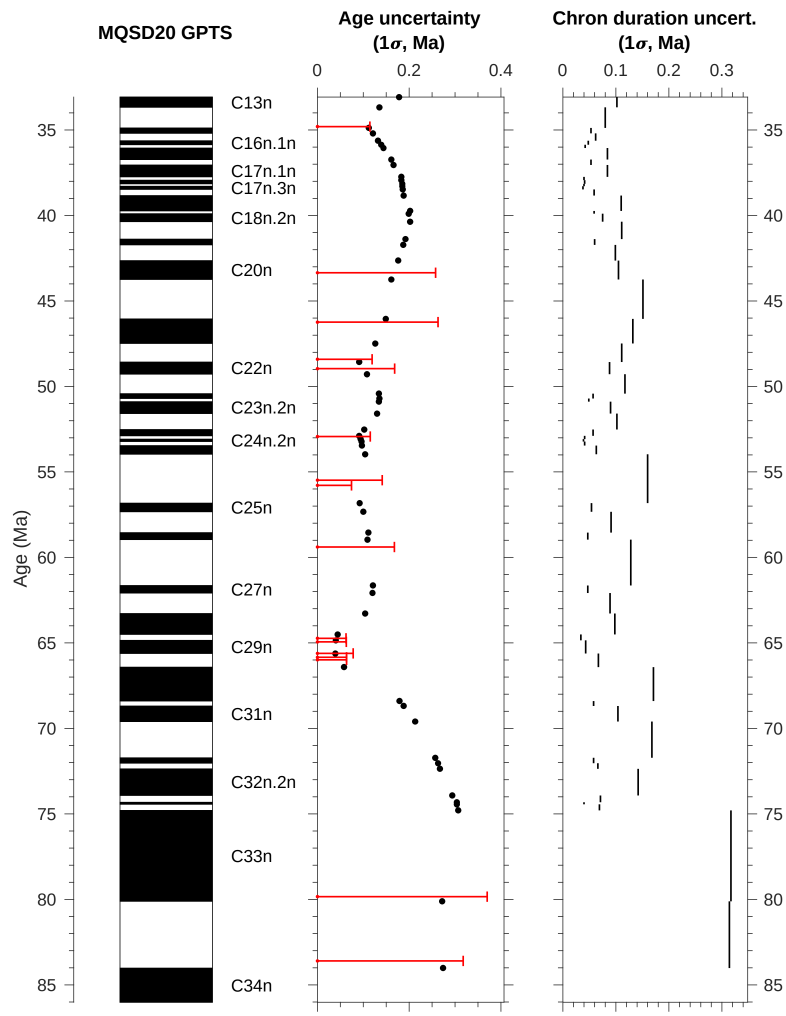

Figure 6. MQSD20 GPTS and its 1σ uncertainties in chron boundary ages and chron duration. Red error bars show the 1σ uncertainties of radiometric dates (Table 3).

The half-spreading rates implied by MQSD20, CK95, and GTS12 for the summary BMDs in the 13 ridge flank regions considered here are compared in Supporting Information Figures S17-S29. The overall variability of spreading rate in each ridge flank region can be quantified by a coefficient of variation (CV) that equals the standard deviation of spreading rate divided by its mean value. Table 5 lists the CVs of spreading rate computed using different GPTSs and the summary BMDs in the 13 ridge flank regions. As MQSD20 minimizes spreading rate variability, the CVs of spreading rate are less than those implied by CK95 and GTS12. The exception is PACVAN-PAC in the North Pacific (Figure 1), where MQSD20 has more variable spreading rates around chrons C17-C18 than CK95 and GTS12 (see Supporting Information Figure S29). The likely reason is that the duration of chrons C17-C18 in CK95 and GTS12 is mostly controlled by magnetic anomaly records in this area of the North Pacific, whereas MQSD20 includes information from other mid-ocean ridge flanks.

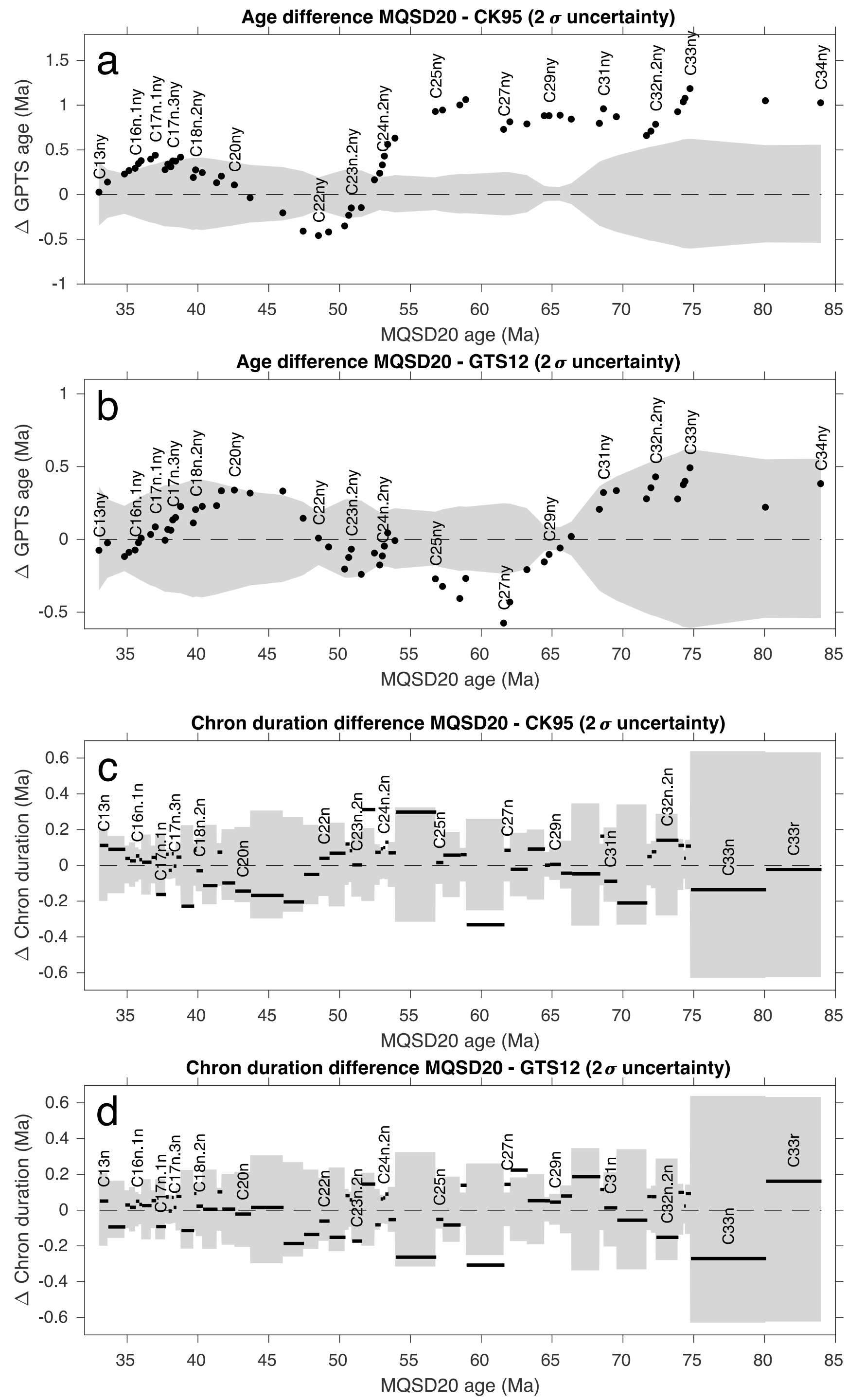

Figure 7. GPTS comparison between MQSD20, CK95, and GTS12. Differences in chron boundary ages are in (a) and (b); differences in chron durations are in (c) and (d). The shaded areas encompass the 2σ uncertainty of the MQSD20 GPTS.

Table 5. Coefficient of variation (CV) of spreading rate in each of the 13 ridge flank regions for different GPTSs.

Ridge flank region	MQSD20	CK95	GTS12
SAMAFR-AFR	0.31	0.46	0.47
SAMAFR-SAM	0.31	0.47	0.53
CAPSOM-CAP	0.28	0.33	0.31
CAPSOM-SOM	0.45	0.63	0.52
CAPANT-CAP	0.43	0.56	0.47
CAPANT-ANT	0.44	0.58	0.49
PACANT-PAC	0.24	0.38	0.30
PACANT-ANT	0.32	0.32	0.38
PACBAN-PAC	0.37	0.55	0.50
PACBAN-BAN	0.26	0.30	0.44
PACFAR-PAC	0.32	0.40	0.36
PACFAV-PAC	0.16	0.33	0.25
PACVAN-PAC	0.23	0.19	0.20

6 Discussion

6.1 Addressing the 50 Ma discrepancy

As it has been obtained independently from astronomical dating, the MQSD20 GPTS can be used to address conflicting results in astrochronology interpretations. We discuss here as an example the "50 Ma discrepancy" noted by Vanderberghe at al. (2012), which centers on the duration of chron C23n.2n. Whereas this chron lasts 696 kyr in the CK95 GPTS, it has been estimated to be less than 400 kyr in several astrochronology studies. From an analysis of the sedimentary record at ODP Site 1258, Westerhold and Röhl (2009) obtained a C23n.2n duration of 379 to 399 kyr, depending on the astronomical cycle chosen (long eccentricity or precession, respectively). Westerhold et al. (2015) confirmed this interpretation in a study that included other drill sites and listed a duration of 377 kyr for C23n.2n. From the ODP Site 1263 record, Lauretano et al. (2016) reported an even shorter C23n.2n duration of 295 kyr in their preferred age model (with an alternative estimate of 395 kyr). When spreading rates are calculated from the South Atlantic BMDs of CK95, these astronomically determined durations result in spreading rates that are more than twice as fast during chron C23n.2n than in adjacent chrons (Figure 6a of Westerhold et al., 2017). A possible explanation offered for this discrepancy is that the CK95 BMDs may be poorly determined around chron C23 (Westerhold et al., 2015; Westerhold & Röhl, 2009), as the width of the chron C23 block has the largest uncertainties reported in CK95 (17.3% of its width; see Table 4 of Cande & Kent, 1992).

Distances to both the young and old end of C23n.2n were estimated in 85 of the 154 ship tracks examined here. All the ridge flank region BMDs record the young and old end of C23n.2n except for PACFAV-PAC, which only spans chrons C24n and older. When spreading rate variations over all ridge flank regions are considered, the duration of C23n.2n in MQSD20 is 699 ± 180 ka (2σ; Table 4). Although we examined a larger magnetic anomaly data set and used a different set of radiometric dates, the duration of C23n.2n we obtain is effectively the same as that in CK95 (696 kyr). This supports the reliability of the CK95 BMDs and implies that a 300-400 kyr duration requires a doubling of spreading rates during C23n.2n in multiple mid-ocean ridges, which is implausible. The duration of C23n.2n in MQSD20 supports the solution of the 50 Ma discrepancy put forward by Westerhold et al. (2017), who concluded that chron C23n is too short in the magnetostratigraphic interpretation of Site 1258. Their revised astronomical time scale gives a C23n.2n duration of 712 ± 123 kyr, which is consistent with the MQSD20 results.

6.2 Spreading rate changes and global tectonic events at ~47 Ma (chron C21)

Figure 8 plots the summary BMDs in each of the 13 ridge flank regions as a function of age in MQSD20. The minimization of global spreading rate fluctuations highlights a major spreading rate change centered at about 47 Ma (chron C21n). Around this time, spreading rates decreased by a factor of 2-3 in the Indian Ocean (Supporting Information Figures S19-S22) while they approximately doubled in the South Atlantic (Figures S17 and S18) and in the North Pacific (Figures S27 and S29). These spreading rate changes coincide with a previously noted set of plate reorganizations (Wessel et al., 2006; Whittaker et al., 2007) that we summarize below.

The prominent decrease in Indian Ocean spreading rates around C21 is related to the onset of the collision between the India subcontinent and Eurasia (Copley et al., 2010; Molnar & Stock, 2009; Patriat & Achache, 1984). To the west, the contemporaneous spreading rate increase in the South Atlantic confirms a general pattern of spreading rate anticorrelation between the Indian and South Atlantic Ocean observed throughout the period 80-30 Ma (Figure 14 of Cande & Patriat, 2015). Moving eastward in the Indian Ocean, in the interval C22-C20 spreading rates decreased substantially in the Wharton Ridge separating the Indian and Australian plates (Jacob et al., 2014). At the same time, a major Australia-Antarctic plate reorganization took place (Whittaker et al., 2007), with Southeast Indian Ridge spreading rates markedly increasing immediately after C21 (Figure 2h of Cogné & Humler, 2006).

In the southeast Pacific Ocean, a major plate boundary reorganization took place around C21, when the Pacific-Antarctic ridge propagated northward breaking off a large fragment of the Pacific plate that became attached to the Antarctic plate (Cande et al., 1982). In the western Pacific, the onset of subduction in the Izu-Bonin-Mariana and Tonga Kermadec arcs has been dated to 45-50 Ma (Bloomer et al., 2013; Cosca et al., 1998; Ishizuka et al., 2011).

In the northern Pacific, an about twofold increase in spreading rate at C21time has been noted by others (Barckhausen et al., 2013; Wright et al., 2015). This spreading rate increase coincides with the prominent change in orientation in the Hawaiian-Emperor seamount chain (Hawaiian-Emperor Bend or HEB), whose date has been recently updated to ~47 Ma (O'Connor et al., 2013; Torsvik et al., 2017; Wessel et al., 2006). The HEB was originally explained by a change in absolute motion of the Pacific plate over a fixed hotspot, but later on several authors argued that it resulted from a slowing southward motion of the Hawaiian hotspot (Norton, 1995; Tarduno et al., 2003; Wright et al., 2015). Torsvik et al. (2017), however, recently concluded that both a southward shift of the Hawaiian hotspot and a change in Pacific plate motion direction are necessary to explain the HEB. The substantial increase in northern Pacific spreading rates at the same time of the HEB strongly suggests a connection. We conjecture that even if the direction of absolute Pacific plate motion did not change, a substantial acceleration in Pacific spreading rate at the time of the HEB over a southward drifting Hawaiian hotspot may have turned the orientation of the Hawaiian-Emperor seamount chain closer to an E-W direction.

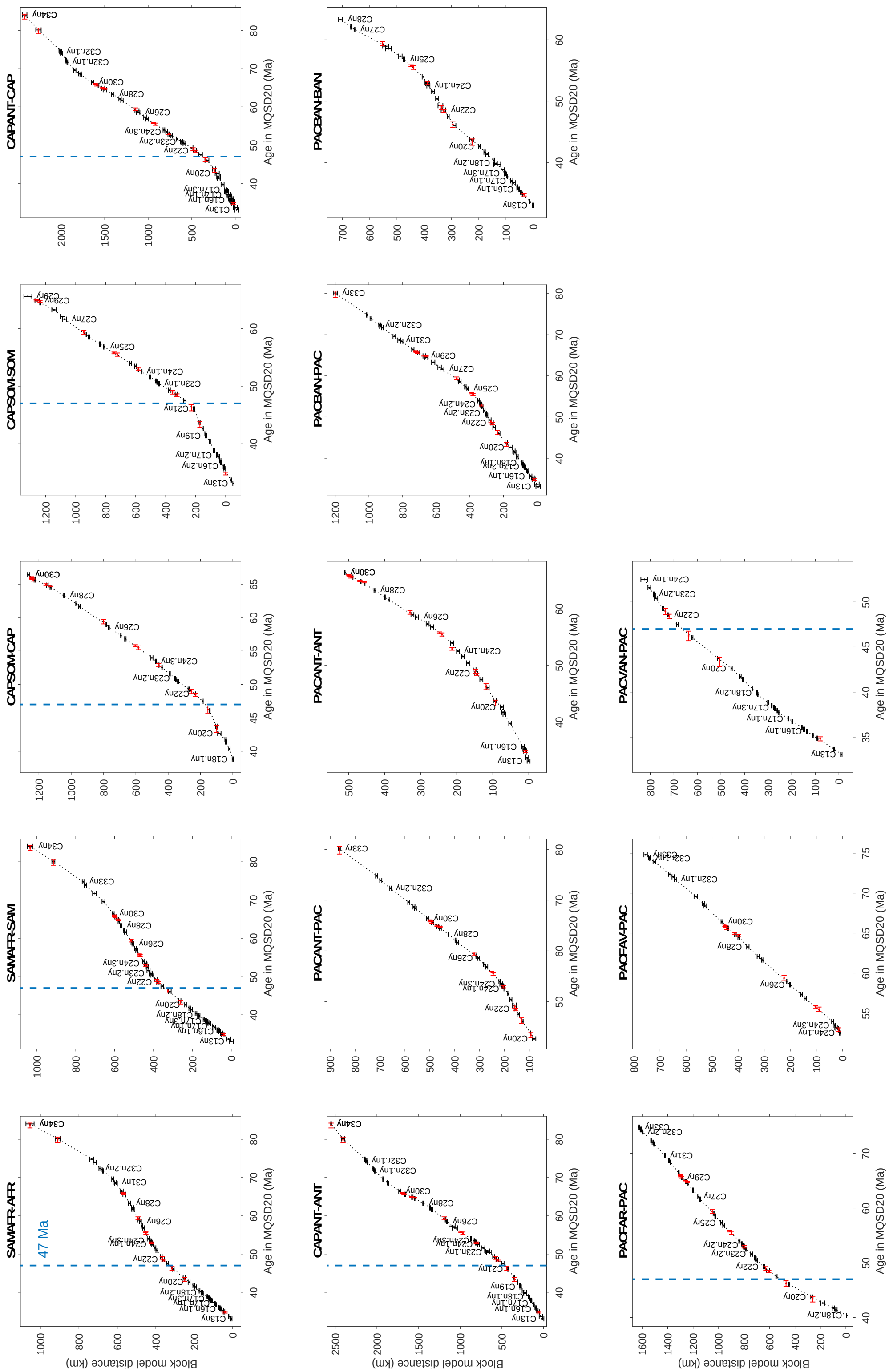

Figure 8. Summary block model distances in 13 ridge flank regions versus MQSD20 GPTS ages. The slope of these distance-age plots is the half-spreading rate. Red symbols are radioisotopic ages (Table 3). Dashed lines highlight a change in spreading rate around 47 Ma in the South Atlantic (SAMAFR-AFR and SAMAFR-SAM), Indian (CAPSOM-CAP, CAPSOM-SOM, CAPANT-CAP, and CAPANT-ANT), and North Pacific Oceans (PACFAR-PAC and PACVAN-PAC).

Contemporaneous worldwide spreading rate changes and plate boundary reorganizations suggest a global connection. As plate motion changes are likely controlled by changes in plate boundary forces (e.g., Gordon et al., 1978), we speculate that the effects of the India-Eurasia collision may have propagated throughout the global plate tectonic system. A comprehensive explanation of the connection between the 47 Ma events is beyond the scope of this paper; however, we stress the importance of a time scale constrained by the global magnetic anomaly record to time and correlate major plate tectonic events.

7 Conclusions

We estimated here a new set of magnetic polarity block model distances (BMDs) spanning the chron C33-C13 interval in 154 ship tracks projected onto plate tectonic flow lines. The ship track data were assembled in summary BMDs over 13 ridge flank regions in the southern and northern Pacific, the southern Atlantic, and the Indian Ocean. This new set of BMDs extends substantially the South Atlantic-based distances originally compiled by Cande & Kent (1992). We used these BMDs to construct a Late Cretaceous-Eocene MQSD20 GPTS that minimizes the variability of spreading rates over all ridge flank regions and fits an up-to-date set of radioisotopic dates. At ~47 Ma, MQSD20 shows a marked spreading rate decrease in the Indian Ocean and a contemporaneous increase in the South Atlantic and Northern Pacific. This spreading rate change coincides with the India-Eurasia collision and with the bend in the Hawaii-Emperor seamount chain.

The MQSD20 GPTS deliberately did not include astrochronology constraints in order to provide an independent source of information to check sediment cycle interpretations. The next step forward in GPTS construction will be to directly incorporate in the time scale information from astrochronology. Such an integration procedure will improve the usual approach, which is to build the time scale on a best data set that is typically taken to supersede other sources of information that are deemed less accurate. For example, future time scale development is often viewed as astronomical dating replacing GPTSs based on marine magnetic anomalies (e.g., Gradstein, 2012 p. 13; Hilgen et al., 2012 p. 947). A GPTS constructed on the basis of magnetic anomalies from multiple spreading centers, rather than from a single mid-ocean ridge, points to a better approach where diverse data sources are combined rather than selectively discarded. In this view, the GPTS is the result of an integration of astrochronology, radioisotopic dates, and magnetic anomaly data, where each piece of information is weighted by a measure of its uncertainty (e.g., Malinverno et al., 2012). The global set of BMDs and the Monte Carlo methods presented here provide the basis for this advance in time scale construction.

Acknowledgments, Samples, and Data

This study was supported by award OCE-1535937 of the U.S. National Science Foundation. Data supporting the conclusions of this study are in two open access data publications that list the 154 ship tracks used here, the geographic positions and distances to polarity block model boundaries (BMDs) in each of the original and projected ship tracks, and the summary BMDs for each of the 13 ridge flank regions (Malinverno et al., 2019a, 2019b). The authors declare no conflict of interest.

References

Baksi, A. K. (1994). Concordant sea-floor spreading rates obtained from geochronology, astrochronology and space geodesy. *Geophys. Res. Lett.*, *21*, 133–136.

Barckhausen, U., Bagge, M., & Wilson, D. S. (2013). Seafloor spreading anomalies and crustal ages of the Clarion-Clipperton Zone. *Marine Geophysical Research*, *34*(2), 79–88. https://doi.org/10.1007/s11001-013-9184-6

Billups, K., Pälike, H., Channell, J. E. T., Zachos, J. C., & Shackleton, N. J. (2004). Astronomic calibration of the Late Oligocene through Early Miocene geomagnetic polarity time scales. *Earth Planet. Sci. Lett.*, *224*, 33–44. https://doi.org/10.1016/j.epsl.2004.05.004

Bloomer, S. H., Taylor, B., Macleod, C. J., Stern, R. J., Fryer, P., Hawkins, J. W., & Johnson, L. (2013). Early Arc Volcanism and the Ophiolite Problem: A Perspective from Drilling in the Western Pacific. In *Active Margins and Marginal Basins of the Western Pacific* (pp. 1–30). American Geophysical Union (AGU). https://doi.org/10.1029/GM088p0001

Brooks, S., Gelman, A., Jones, G. L., & Meng, X.-L. (2011). *Handbook of Markov Chain Monte Carlo*. Boca Raton, Florida: Chapman & Hall/CRC.

Brown, R. E., Koeberl, C., Montanari, A., & Bice, D. M. (2009). Evidence for a change in Milankovitch forcing caused by extraterrestrial events at Massignano, Italy, Eocene-Oligocene boundary GSSP. In C. Koeberl & A. Montanari (Eds.), *The Late Eocene Earth-Hothouse, Icehouse, and Impacts* (pp. 119–137). Boulder, Colorado: Geological Society of America Special Paper 452. Retrieved from https://doi.org/10.1130/2009.2452(08)

Cande, S. C., & Kent, D. V. (1992). A new geomagnetic polarity time scale for the Late Cretaceous and Cenozoic. *J. Geophys. Res.*, *97*(B10), 13,917-13,951.

Cande, S. C., & Kent, D. V. (1995). Revised calibration of the geomagnetic polarity time scale for the Late Cretaceous and Cenozoic. *J. Geophys. Res.*, *100*(B4), 6093–6095.

Cande, S. C., & Patriat, P. (2015). The anticorrelated velocities of Africa and India in the Late Cretaceous and early Cenozoic. *Geophys. J. Int.*, *200*, 227–243. https://doi.org/10.1093/gji/ggu392

Cande, S. C., Herron, E. M., & Hall, B. R. (1982). The early Cenozoic tectonic history of the southeast Pacific. *Earth and Planetary Science Letters*, *57*(1), 63–74. https://doi.org/10.1016/0012-821X(82)90173-X

Cande, S. C., LaBrecque, J. L., & Haxby, W. F. (1988). Plate kinematics of the South Atlantic: Chron C34 to present. *J. Geophys. Res.*, *93*(B4), 13,479-13,492.

Cande, S. C., Patriat, P., & Dyment, J. (2010). Motion between the Indian, Antarctic and African plates in the early Cenozoic. *Geophys. J. Int.*, *183*, 127–149. https://doi.org/10.1111/j.1365-246X.2010.04737.x

Chib, S., & Greenberg, E. (1995). Understanding the Metropolis-Hastings algorithm. *The American Statistician*, *49*, 327–335.

Cogné, J.-P., & Humler, E. (2006). Trends and rhythms in global seafloor generation rate. *Geochem. Geophys. Geosyst.*, *7*, Q03011. https://doi.org/10.1029/2005GC001148

Copley, A., Avouac, J.-P., & Royer, J.-Y. (2010). India-Asia collision and the Cenozoic slowdown of the Indian plate: Implications for the forces driving plate motions. *Journal of Geophysical Research: Solid Earth*, *115*(B3). https://doi.org/10.1029/2009JB006634

Cosca, M., Arculus, R., Pearce, J., & Mitchell, J. (1998). 40Ar/ 39Ar and K–Ar geochronological age constraints for the inception and early evolution of the Izu–Bonin – Mariana arc system. *Island Arc*, *7*(3), 579–595. https://doi.org/10.1111/j.1440-1738.1998.00211.x

Croon, M. B., Cande, S. C., & Stock, J. M. (2008). Revised Pacific-Antarctic plate motions and geophysics of the Menard Fracture Zone. *Geochem. Geophys. Geosyst.*, *9*, Q07001. https://doi.org/10.1029/2008GC002019

Gee, J. S., & Kent, D. V. (2007). Source of oceanic magnetic anomalies and the geomagnetic polarity timescale. In G. Schubert (Ed.), *Treatise on Geophysics, vol. 5* (pp. 455–507). Amsterdam: Elsevier.

Gelman, A. B., Carlin, J. S., Stern, H. S., & Rubin, D. B. (2004). *Bayesian Data Analysis* (2nd ed.). Boca Raton, Florida: Chapman and Hall/CRC.

Gilks, W. R., Richardson, S., & Spiegelhalter, D. J. (1996). *Markov chain Monte Carlo in practice*. London: Chapman and Hall.

Glen, W. (1982). *The Road to Jaramillo*. Stanford, CA: Stanford University Press.

Gordon, R. G. (1993). Orbital dates and steady rates. *Nature*, *364*, 760–761.

Gordon, R. G., Cox, A., & Harter, C. E. (1978). Absolute motion of an individual plate estimated from its ridge and trench boundaries. *Nature*, *274*(5673), 752–755. https://doi.org/10.1038/274752a0

Gradstein, F. M. (2012). Introduction. In F. M. Gradstein, J. G. Ogg, M. D. Schmitz, & G. M. Ogg (Eds.), *The Geologic Time Scale 2012* (pp. 1–29). Amsterdam: Elsevier.

Gradstein, F. M., Ogg, J. G., Schmitz, M. D., & Ogg, G. M. (2012). *The Geologic Time Scale 2012*. Amsterdam: Elsevier.

Heirtzler, J. R., Dickson, G. O., Herron, E. M., Pitman, W. C., & LePichon, X. (1968). Marine magnetic anomalies, geomagnetic field reversals, and motions of the ocean floor and continents. *J. Geophys. Res.*, *73*, 2119–2136.

Herbert, T. D., Premoli Silva, I., Erba, E., & Fischer, A. G. (1995). Orbital chronology of Cretaceous-Paleocene marine sediments. In W. A. Berggren, D. V. Kent, M. P. Aubry, & J. Hardenbol (Eds.), *Geochronology, Timescales, and Stratigraphic Correlation* (pp. 81–93). Tulsa, Oklahoma: Society for Sedimentary Geology.

Hilgen, F. J., Kuiper, K. F., & Lourens, L. J. (2010). Evaluation of the astronomical time scale for the Paleocene and earliest Eocene. *Earth Planet. Sci. Lett.*, *300*, 139–151. https://doi.org/10.1016/j.epsl.2010.09.044

Hilgen, F. J., Lourens, L. J., & Van Dan, J. A. (2012). The Neogene Period. In F. M. Gradstein, J. G. Ogg, M. D. Schmitz, & G. M. Ogg (Eds.), *The Geologic Time Scale 2012* (pp. 923–978). Amsterdam: Elsevier.

Hinnov, L. A., & Hilgen, F. J. (2012). Cyclostratigraphy and astrochronology. In F. M. Gradstein, J. G. Ogg, M. D. Schmitz, & G. M. Ogg (Eds.), *The Geologic Time Scale 2012* (pp. 63–83). Amsterdam: Elsevier.

Huestis, S. P., & Acton, G. D. (1997). On the construction of geomagnetic timescales from non-prejudicial treatment of magnetic anomaly data from multiple ridges. *Geophys. J. Int.*, *129*, 176–182.

Husson, D., Galbrun, B., Laskar, J., Hinnov, L. A., Thibault, N., Gardin, S., & Locklair, R. E. (2011). Astronomical calibration of the Maastrichtian (Late Cretaceous). *Earth Planet. Sci. Lett.*, *305*, 328–340. https://doi.org/10.1016/j.epsl.2011.03.008

Ishizuka, O., Tani, K., Reagan, M. K., Kanayama, K., Umino, S., Harigane, Y., et al. (2011). The timescales of subduction initiation and subsequent evolution of an oceanic island arc. *Earth and Planetary Science Letters*, *306*(3), 229–240. https://doi.org/10.1016/j.epsl.2011.04.006

Jacob, J., Dyment, J., & Yatheesh, V. (2014). Revisiting the structure, age, and evolution of the Wharton Basin to better understand subduction under Indonesia. *Journal of Geophysical Research: Solid Earth*, *119*(1), 169–190. https://doi.org/10.1002/2013JB010285

Jovane, L., Sprovieri, M., Coccioni, R., Florindo, F., Marsili, A., & Laskar, J. (2010). Astronomical calibration of the middle Eocene Contessa Highway section (Gubbio, Italy). *Earth Planet. Sci. Lett.*, *298*, 77–88. https://doi.org/10.1016/j.epsl.2010.07.027

Krijgsman, W., Hilgen, F. J., Raffi, I., Sierro, F. J., & Wilson, D. S. (1999). Chronology, causes and progression of the Messinian salinity crisis. *Nature*, *400*, 652–655.

Lanci, L., Lowrie, W., & Montanari, A. (1996). Magnetostratigraphy of the Eocene/Oligocene boundary in a short drill-core. *Earth Planet. Sci. Lett.*, *143*, 37–48.

Langereis, C. G., van Hoof, A. A. M., & Hilgen, F. J. (1994). Steadying the rates. *Nature*, *369*, 615.

Lauretano, V., Hilgen, F. J., Zachos, J. C., & Lourens, L. J. (2016). Astronomically tuned age model for the early Eocene carbon isotope events: A new high-resolution δ13C benthic record of ODP Site 1263 between ~49 and ~54 Ma. *Newsletters on Stratigraphy*, 383–400. https://doi.org/10.1127/nos/2016/0077

Lowrie, W., & Lanci, L. (1994). Magnetostratigraphy of Eocene-Oligocene boundary sections in Italy: No evidence for short subchrons within chrons 12R and 13R. *Earth Planet. Sci. Lett.*, *126*, 247–258.

Malinverno, A. (2002). Parsimonious Bayesian Markov chain Monte Carlo inversion in a nonlinear geophysical problem. *Geophys. J. Int.*, *151*, 675–688. https://doi.org/10.1046/j.1365-246X.2002.01847.x

Malinverno, A., & Briggs, V. A. (2004). Expanded uncertainty quantification in inverse problems: Hierarchical Bayes and empirical Bayes. *Geophysics*, *69*, 1005–1016. https://doi.org/10.1190/1.1778243

Malinverno, A., & Leaney, W. S. (2005). Monte Carlo Bayesian look-ahead inversion of walkaway vertical seismic profiles. *Geophys. Prosp.*, *53*, 689–703. https://doi.org/10.1111/j.1365-2478.2005.00496.x

Malinverno, A., Hildebrandt, J., Tominaga, M., & Channell, J. E. T. (2012). M-sequence geomagnetic polarity time scale (MHTC12) that steadies global spreading rates and incorporates astrochronology constraints. *J. Geophys. Res.*, B06104. https://doi.org/10.1029/2012JB009260

Malinverno, A., Quigley, K., Staro, A., & Dyment, J. (2019a). Location and distances to oceanic magnetic polarity block boundaries (anomalies 13ny-34ny) on a global ship track data set (South Atlantic, Indian, South Pacific, and North Pacific Oceans). *Interdisciplinary Earth Data Alliance (IEDA)*. https://doi.org/10.1594/IEDA/326490

Malinverno, A., Quigley, K., Staro, A., & Dyment, J. (2019b). Summary distances to oceanic magnetic polarity block boundaries (anomalies 13ny-34ny) on a global set of mid-ocean ridge flanks (South Atlantic, Indian, South Pacific, and North Pacific Oceans). *Interdisciplinary Earth Data Alliance (IEDA)*. https://doi.org/10.1594/IEDA/326491

Matthews, K. J., Müller, R. D., Wessel, P., & Whittaker, J. M. (2011). The tectonic fabric of the ocean basins. *J. Geophys. Res.*, *116*, B12109. https://doi.org/10.1029/2011JB008413

Metropolis, N., Rosenbluth, A. W., Rosenbluth, M. N., Teller, A. H., & Teller, E. (1953). Equation of state calculations by fast computing machines. *J. Chem. Phys.*, *21*, 1087–1092.

Molnar, P., & Stock, J. M. (2009). Slowing of India's convergence with Eurasia since 20 Ma and its implications for Tibetan mantle dynamics. *Tectonics*, *28*(3). https://doi.org/10.1029/2008TC002271

Montanari, A., Asaro, F., Michel, H. V., & Kennett, J. P. (1993). Iridium anomalies of Late Eocene age at Massignano (Italy) and ODP Site 689B (Maud Rise, Antarctic). *Palaios*, *8*, 420–437.

Mosegaard, K., & Tarantola, A. (1995). Monte Carlo sampling of solutions to inverse problems. *J. Geophys. Res.*, *100*, 12,431-12,447.

Müller, R. D., Royer, J.-Y., Cande, S. C., Roest, W. R., & Maschenkov, S. (1999). New constraints on the Late Cretaceous/Early Tertiary plate tectonic evolution of the Caribbean. In P. Mann (Ed.), *Caribbean Basins* (pp. 33–59). Amsterdam: Elsevier.

NOAA National Geophysical Data Center. (1977). *Marine Trackline Geophysical Database*. NOAA National Centers for Environmental Information. Retrieved from https://doi.org/10.7289/V5CZ35DR

Norton, I. O. (1995). Plate motions in the North Pacific: The 43 Ma nonevent. *Tectonics*, *14*(5), 1080–1094. https://doi.org/10.1029/95TC01256

O'Connor, J. M., Steinberger, B., Regelous, M., Koppers, A. A. P., Wijbrans, J. R., Haase, K. M., et al. (2013). Constraints on past plate and mantle motion from new ages for the Hawaiian-Emperor Seamount Chain. *Geochemistry, Geophysics, Geosystems*, *14*(10), 4564–4584. https://doi.org/10.1002/ggge.20267

Odin, G. S., Montanari, A., Deino, A., Drake, R., Guise, P. G., Kreuzer, H., & Rex, D. C. (1991). Reliability of volcano-sedimentary biotite ages across the Eocene-Oligocene boundary (Apennines, Italy). *Chem. Geol.*, *86*, 203–224.

Ogg, J. G. (2012). Geomagnetic polarity time scale. In F. M. Gradstein, J. G. Ogg, M. D. Schmitz, & G. M. Ogg (Eds.), *The Geologic Time Scale 2012* (pp. 85–113). Amsterdam: Elsevier.

Ogg, J. G., & Smith, A. G. (2004). The geomagnetic polarity time scale. In F. M. Gradstein, J. G. Ogg, & A. G. Smith (Eds.), *A Geologic Time Scale 2004* (pp. 63–86). Cambridge: Cambridge University Press.

Opdyke, N. D., & Channell, J. E. T. (1996). *Magnetic Stratigraphy*. San Diego: Academic Press.

Pälike, H., Shackleton, N. J., & Röhl, U. (2001). Astronomical forcing in Late Eocene marine sediments. *Earth Planet. Sci. Lett.*, *193*, 589–602.

Parsons, B., & Sclater, J. G. (1977). An analysis of the variation of ocean floor bathymetry and heat flow with age. *J. Geophys. Res.*, *82*, 803–827.

Patriat, P., & Achache, J. (1984). India–Eurasia collision chronology has implications for crustal shortening and driving mechanism of plates. *Nature*, *311*(5987), 615–621. https://doi.org/10.1038/311615a0

Piana Agostinetti, N., & Malinverno, A. (2010). Receiver function inversion by trans-dimensional Monte Carlo sampling. *Geophys. J. Int.*, *181*, 858–872. https://doi.org/10.1111/j.1365-246X.2010.04530.x

Röhl, U., Norris, R. D., & Ogg, J. G. (2003). Cyclostratigraphy of upper Paleocene and lower Eocene sediments at Blake Nose Site 1051 (western North Atlantic). In S. L. Wing, P. D. Gingerich, B. Schmitz, & E. Thomas (Eds.), *Causes and Consequences of Globally Warm Climates in the Early Paleogene*. Boulder, Colorado: Geological Society of America Special Paper 369.

Sambridge, M., & Mosegaard, K. (2002). Monte Carlo methods in geophysical inverse problems. *Rev. Geophys.*, *40(3)*, 1009. https://doi.org/10.1029/2000RG000089

Schouten, H., & McCamy, K. (1972). Filtering marine magnetic anomalies. *J. Geophys. Res.*, *77*, 7089–7099.

Sen, M. K., & Stoffa, P. L. (2013). *Global Optimization Methods in Geophysical Inversion* (2nd ed.). Cambridge, New York: Cambridge University Press.

Seton, M., Whittaker, J. M., Wessel, P., Müller, R. D., DeMets, C., Merkouriev, S., et al. (2014). Community infrastructure and repository for marine magnetic identifications. *Geochem. Geophys. Geosyst.*, *15*, 1629–1641. https://doi.org/10.1002/2013GC005176

Swisher, C. C., Dingus, L., & Butler, R. F. (1993). $^{40}Ar/^{39}Ar$ dating and magnetostratigraphic correlation of the terrestrial Cretaceous-Paleogene boundary and Puercan Mammal Age, Hell Creek-Tullock formations, eastern Montana. *Can. J. Earth Sci.*, *30*, 1981–1996.

Tarduno, J. A., Duncan, R. A., Scholl, D. W., Cottrell, R. D., Steinberger, B., Thordarson, T., et al. (2003). The Emperor Seamounts: Southward Motion of the Hawaiian Hotspot Plume in Earth's Mantle. *Science*, *301*(5636), 1064–1069. https://doi.org/10.1126/science.1086442

Torsvik, T. H., Doubrovine, P. V., Steinberger, B., Gaina, C., Spakman, W., & Domeier, M. (2017). Pacific plate motion change caused the Hawaiian-Emperor Bend. *Nature Communications*, *8*(1), 1–12. https://doi.org/10.1038/ncomms15660

Vandenberghe, N., Hilgen, F. J., & Speijer, R. P. (2012). The Paleogene Period. In F. M. Gradstein, J. G. Ogg, M. D. Schmitz, & G. M. Ogg (Eds.), *The Geologic Time Scale 2012* (pp. 855–921). Amsterdam: Elsevier.

Wei, W. (1995). Revised age calibration points for the geomagnetic polarity time scale. *Geophys. Res. Lett.*, *22*, 957–960. https://doi.org/10.1029/95GL00377

Wessel, P., Harada, Y., & Kroenke, L. W. (2006). Toward a self-consistent, high-resolution absolute plate motion model for the Pacific. *Geochemistry, Geophysics, Geosystems*, *7*(3). https://doi.org/10.1029/2005GC001000

Westerhold, T., & Röhl, U. (2009). High resolution cyclostratigraphy of the early Eocene – new insights into the origin of the Cenozoic cooling trend. *Clim. Past*, *5*, 309–327, www.clim-past.net/5/309/2009/.

Westerhold, T., Röhl, U., Laskar, J., Raffi, I., Bowles, J., Lourens, L. J., & Zachos, J. C. (2007). On the duration of magnetochrons C24r and C25n and the timing of early Eocene global warming events: Implications from the Ocean Drilling Program Leg 208 Walvis Ridge depth transect. *Paleoceanogr.*, *22*, PA2201. https://doi.org/10.1029/2006PA001322

Westerhold, T., Röhl, U., Raffi, I., Fornaciari, E., Monechi, S., Reale, V., et al. (2008). Astronomical calibration of the Paleocene time. *Palaeogeogr., Palaeoclim., Palaeoecol.*, *257*, 377–403. https://doi.org/10.1016/j.palaeo.2007.09.016

Westerhold, T., Röhl, U., Frederichs, T., Bohaty, S. M., & Zachos, J. C. (2015). Astronomical calibration of the geological timescale: closing the middle Eocene gap. *Climate of the Past*, *11*(9), 1181–1195. https://doi.org/10.5194/cp-11-1181-2015

Westerhold, T., Röhl, U., Frederichs, T., Agnini, C., Raffi, I., Zachos, J. C., & Wilkens, R. H. (2017). Astronomical calibration of the Ypresian timescale: implications for seafloor spreading rates and the chaotic behavior of the solar system? *Clim. Past*, *13*, 1129–1152. https://doi.org/10.5194/cp-13-1129-2017

Whittaker, J. M., Müller, R. D., Leitchenkov, G., Stagg, H., Sdrolias, M., Gaina, C., & Goncharov, A. (2007). Major Australian-Antarctic Plate Reorganization at Hawaiian-Emperor Bend Time. *Science; Washington*, *318*(5847), 83–86. http://dx.doi.org.ezproxy.cul.columbia.edu/10.1126/science.1143769

Wilson, D. S. (1993). Confirmation of the astronomical calibration of the magnetic polarity timescale from sea-floor spreading rates. *Nature*, *364*, 788–790.

Wright, N. M., Müller, R. D., Seton, M., & Williams, S. E. (2015). Revision of Paleogene plate motions in the Pacific and implications for the Hawaiian-Emperor bend. *Geology*, *43*, 455–458. https://doi.org/10.1130/G36303.1

Wright, N. M., Müller, R. D., Seton, M., & Williams, S. E. (2016). The Late Cretaceous to recent tectonic history of the Pacific Ocean basin. *Earth-Sci. Rev.*, *154*, 138–173. https://doi.org/10.1016/j.earscirev.2015.11.015

Yatheesh, V., Dyment, J., Bhattacharya, G. C., Royer, J.-Y., Kamesh Raju, K. A., Ramprasad, T., et al. (2019). Detailed Structure and Plate Reconstructions of the Central Indian Ocean Between 83.0 and 42.5 Ma (Chrons 34 and 20). *J. Geophys. Res.*, *124*, 4305–4322. https://doi.org/10.1029/2018JB016812

Zachos, J. C., Pagani, M., Sloan, L., Thomas, E., & Billups, K. (2001). Trends, rhythms, and aberrations in global climate 65 Ma to present. *Science*, *292*, 686–693.

Zachos, J. C., Dickens, G. R., & Zeebe, R. E. (2008). An early Cenozoic perspective on greenhouse warming and carbon-cycle dynamics. *Nature*, *451*, 279–283. https://doi.org/10.1038/nature06588

Journal of Geophysical Research

Supporting information for

A Late Cretaceous-Eocene Geomagnetic Polarity Time Scale (MQSD20) that steadies spreading rates on multiple mid-ocean ridge flanks

A. Malinverno[1], K. W. Quigley[2], A. Staro[3], and J. Dyment[4]

[1]Lamont-Doherty Earth Observatory of Columbia University, Palisades, New York, USA

[2]Brown University, Providence, Rhode Island, USA

[3]Dipartimento di Scienze della Terra, Università degli Studi di Milano, Italy

[4]Université de Paris, Institut de Physique du Globe de Paris, CNRS, Paris, France

Contents of this file

Introduction

The Supporting Information includes text that details the implementation of Markov chain Monte Carlo (MCMC) sampling for two cases. Text S1 describes the sampling of block model distances along a ship track projected onto a flow line to fit measured magnetic anomalies. Text S2 describes the sampling of ages in a geomagnetic polarity time scale (GPTS) to minimize global variations in spreading rate and fit radioisotopic dates. The notation used in the text is listed in Table S1. Figures S1 to S16 are maps showing the locations of original and projected ship tracks and of selected polarity block boundaries in 13 ridge flank regions. Figure S17 to S29 plot a comparison of half-spreading rates in 13 ridge flank regions for three GPTSs: MQSD20 (this paper), CK95 (Cande & Kent 1992, 1995), and GTS12 (Ogg 2012).

Text S1. MCMC sampling of block model distances

The parameter vector

This sampling generates a number of block model distances (BMDs) that result in a good fit between observed and modeled magnetic anomalies in each of the projected ship tracks. In any given ship track, the parameter vector **m** includes

- A vector of BMDs for the anomalies in the track.
- The standard deviation σ_e of the misfits between observed and predicted magnetic anomalies. This hyperparameter (Gelman et al. 2004; Malinverno & Briggs 2004) is included in **m** because it is not known a priori. Sampling will determine how closely the magnetic anomaly data can be fitted.
- A set of nodes spaced every ~50 km that define a multiplier for the magnetic anomaly amplitudes (Figure 2 in the main text). Adjusting the amplitude of the predicted anomalies to match those observed is necessary to prevent the Monte Carlo algorithm from sampling unrealistically narrow polarity blocks in areas of low-amplitude anomalies (see the main text).

Data and likelihood function

The observed data **d** in the likelihood function are the magnetic anomaly data, highpass filtered to eliminate long-wavelength components that are not generated by magnetized crustal blocks and normalized to zero mean and unit variance. The predicted data $\mathbf{d}_{\mathsf{pred}}$ are magnetic anomalies computed by upward continuation of crustal blocks of constant positive or negative magnetization. The horizontal distances to the block boundaries are defined by the BMDs, and the blocks are assumed to be be between 5,000 m and 5,500 m below sea level. The predicted anomalies are phase-shifted for the given skewness angle, multiplied by the anomaly multiplier values, and normalized. The likelihood function is defined as a multivariate normal PDF:

$$p(\mathbf{d}|\mathbf{m}) = (2\pi\sigma_e^2)^{-N_d/2} \exp\left[-\frac{1}{2\sigma_e^2}(\mathbf{d}-\mathbf{d}_{\mathsf{pred}})^{\mathsf{T}}(\mathbf{d}-\mathbf{d}_{\mathsf{pred}})\right], \tag{1}$$

where $\mathbf{x}^{\mathsf{T}}$ denotes the transpose of the vector **x**, N_d is the length of the data vectors, and σ_e^2 is the variance of the misfits between observed and predicted data.

Generating candidate parameter vectors

The generation of candidate parameters $\mathbf{m}^*$ starts by choosing at random between one of the BMDs (with probability 0.4), one of the nodes of the magnetic anomaly multipliers (probability 0.4), the anomaly skewness angle (probability 0.1), or the standard deviation of the data misfits σ_e (probability 0.1). A candidate value for the parameter to perturb is then chosen at random from its prior distribution. The prior distributions of the parameters in **m** are uniform between reasonable minimum and maximum bounds. Each of the BMDs has a uniform prior between the distances to the surrounding BMDs ±1 km (to avoid zero-width magnetic blocks). The anomaly multiplier nodes have a uniform prior between 0.3 and 1.7. The skewness angle has a uniform prior between bounds of ±30° around the initial value. The misfit standard deviation has a log-uniform prior between a minimum equal to 1/3 of σ_e for the initial BMDs and a maximum of 1 (a very poor fit for standardized data).

MCMC sampling

Starting the sampling from an initial value of the parameters that approximately fits the data, the MCMC algorithm generates a sample of BMDs that fit the observed magnetic anomalies as closely as possible (see Figure 2 in the main text). The MCMC algorithm was run for 20,000 iterations, and the sampled BMDs were saved every 50 iterations to result in a final sample of 400 BMDs in each ship track. (As only one parameter in the candidate vector is changed at each iteration, consecutive samples are very similar and it is unnecessary to save them all.) The mean and standard deviation of the sampled values define a best value and an uncertainty for the BMDs along the projected ship track, which are the input to the construction of summary BMDs in each ridge flank region (see the main text). Maps of the 154 original and projected ship tracks and geographic positions of selected polarity block boundaries in each of the original tracks are in Figures S1-S16.

Text S2. MCMC sampling of the Geomagnetic Polarity Time Scale

The parameter vector

This sampling generates a number of geomagnetic polarity time scales (GPTSs) that fit a set of radioisotopic dates (see Table 3 in the main text) and that minimize the global variation of spreading rates. The parameter vector $\mathbf{m}$ includes

- A GPTS vector $\mathbf{t}$ of 59 ages of polarity chron boundaries (from C13ny to C34ny).
- A vector $\mathbf{c}$ of 13 coefficients of variation (CVs) that are the ratio between the standard deviation and the average of the spreading rates; these CVs quantify the long-term variations of spreading rate in each of the mid-ocean ridge flank regions.

The CVs are the ratio of the standard deviation over the average spreading rate. There are two major sources of variability in the spreading rates calculated over a ridge flank for a given GPTS: short-term variations due to uncertainties in the estimated BMDs and long-term changes due to changes in large-scale plate motion. Both these sources of variation need to be taken into account in the calculation of the likelihood. The size of long-term spreading rate variations will be different on different mid-ocean ridge flanks, and the 13 CVs in the parameter vector are hyperparameters that are not assumed to be known a priori (Gelman et al. 2004; Malinverno & Briggs 2004). Sampling will determine the magnitude of the long-term spreading rate variations over each ridge flank region.

The observed data vector in the likelihood

The vector of observed data $\mathbf{d}$ in the likelihood function is the combination of several data vectors:

- Thirteen vectors of spreading rates $\mathbf{u}^{[j]}$ ($j = 1, 2, \ldots, 13$) in each of the mid-ocean ridge flank regions computed from the BMDs in $\mathbf{b}$ and the GPTS ages in $\mathbf{t}$.
- A vector $\mathbf{r}$ of 16 radioisotopic dates from magnetostratigraphy (Table 3 in the main text).

As the uncertainties of spreading rates over each of the 13 ridge flank regions and the uncertainties of radioisotopic dates are uncorrelated, we can write the total likelihood as the product of each likelihood:

$$p(\mathbf{d}|\mathbf{m}) = p(\mathbf{u}^{[1]}|\mathbf{m})p(\mathbf{u}^{[2]}|\mathbf{m}) \ldots p(\mathbf{u}^{[13]}|\mathbf{m})p(\mathbf{r}|\mathbf{m}). \quad (2)$$

Likelihood of spreading rates

We describe here the likelihood function of spreading rates in a mid-ocean ridge flank region. For simplicity of notation, we omit in this section the superscript $[j]$ that denotes the ridge flank region (e.g., we write $\mathbf{u}^{[j]}$ as $\mathbf{u}$). The likelihood for a vector $\mathbf{u}$ of N_u spreading rates in the j-th ridge flank region is a multivariate normal PDF with a mean equal to a weighted average spreading rate $\overline{u}$ and a covariance matrix $\mathbf{C}_u$ as in

$$p(\mathbf{u}|\mathbf{m}) = [(2\pi)^{N_u} \det \mathbf{C}_u]^{-1/2} \exp\left[-\frac{1}{2}(\mathbf{u}-\overline{u})^{\mathsf{T}}\mathbf{C}_u^{-1}(\mathbf{u}-\overline{u})\right], \tag{3}$$

The half-spreading rates in the vector $\mathbf{u}$ of Equation 3 are computed from the vector $\mathbf{b}$ of BMDs in the j-th ridge flank region and the GPTS in $\mathbf{t}$ as

$$u_i = \frac{b_{i+1} - b_i}{t_{i+1} - t_i}, \tag{4}$$

where the ages t_i are the ages of the GPTS chron boundaries that correspond to the BMDs in $\mathbf{b}$. The spreading rate calculation can be written as

$$\mathbf{u} = \mathbf{H}\,\mathbf{b}, \tag{5}$$

where $\mathbf{H}$ is a matrix that depends on the GPTS in $\mathbf{t}$

$$\mathbf{H} = \begin{bmatrix} -\frac{1}{t_2 - t_1} & \frac{1}{t_2 - t_1} & 0 & \dots & 0 & 0 \\ 0 & -\frac{1}{t_3 - t_2} & \frac{1}{t_3 - t_2} & \dots & 0 & 0 \\ \vdots & \vdots & \vdots & \ddots & \vdots & \vdots \\ 0 & 0 & 0 & \dots & -\frac{1}{t_{N_u+1} - t_{N_u}} & \frac{1}{t_{N_u+1} - t_{N_u}} \end{bmatrix}. \tag{6}$$

The covariance matrix $\mathbf{C}_u$ in Equation 3 accounts for two sources of variation in spreading rates over their average: uncertainties in the estimated BMDs in $\mathbf{b}$ and long-term variations in spreading rate quantified by the CVs in the vector $\mathbf{c}$. The uncertainties in the BMDs are described by a diagonal covariance matrix $\mathbf{C}_b$ that contains the variances obtained by assembling rescaled distances from projected ship tracks in the j-th ridge flank region (as described in the main text). From the properties of the multivariate normal distribution, the covariance matrix of the spreading rates $\mathbf{u}$ in Equation 5 that accounts for uncertainties in $\mathbf{b}$ is

$$\mathbf{C}_1 = \mathbf{H}\,\mathbf{C}_b\,\mathbf{H}^{\mathsf{T}}. \tag{7}$$

The weighted average spreading rate $\overline{u}$ in Equation 3 is obtained by weighing each value of spreading rate in $\mathbf{u}$ by the respective variance in the diagonal of $\mathbf{C}_1$.

The long-term variations of spreading rates are quantified by a diagonal covariance matrix $\mathbf{C}_2$ defined as

$$\mathbf{C}_2 = (c_j\overline{u})^2\mathbf{I}, \tag{8}$$

where c_j is the CV of spreading rates for the j-th ridge flank region and $\mathbf{I}$ is the $N_u \times N_u$ identity matrix.

The covariance matrix $\mathbf{C}_u$ in the likelihood of Equation 3 combines the two sources of spreading rate variation as

$$\mathbf{C}_u = \mathbf{C}_1 + \mathbf{C}_2. \tag{9}$$

Because of the structure of $\mathbf{H}$ (Equation 6), the matrix $\mathbf{C}_1$ is tridiagonal. We simplify the treatment and speed up calculations by discarding the off-diagonal elements of $\mathbf{C}_1$, so that $\mathbf{C}_u$ is also diagonal. This simplification does not impact significantly our results. We ran tests comparing Monte Carlo sampling results obtained using a tridiagonal or a diagonal $\mathbf{C}_1$, and found that they were very similar.

Likelihood of radioisotopic dates

The likelihood for a vector $\mathbf{r}$ of N_r measured radioisotopic dates is a multivariate normal PDF as in

$$p(\mathbf{r}|\mathbf{m}) = [(2\pi)^{N_r} \det \mathbf{C}_r]^{-1/2} \exp\left[-\frac{1}{2}(\mathbf{r} - \mathbf{r}_{\mathsf{pred}})^{\mathsf{T}} \mathbf{C}_r^{-1} (\mathbf{r} - \mathbf{r}_{\mathsf{pred}})\right]. \tag{10}$$

The vector of predicted dates $\mathbf{r}_{\mathsf{pred}}$ is obtained by linearly interpolating the GPTS ages in $\mathbf{t}$ to the stratigraphic positions of each date (Table 3 in the main text). The covariance matrix $\mathbf{C}_r$ is a diagonal matrix containing the total variances of each radioisotopic date. This total variance is the sum of the variance due to radioisotopic measurement uncertainty and the variance due to stratigraphic uncertainty (see the main text).

Generating candidate parameter vectors

Candidate parameters $\mathbf{m}^*$ are obtained by sampling at each iteration a candidate GPTS vector $\mathbf{t}^*$ and a candidate CV vector $\mathbf{c}^*$. The candidate GPTS is determined in two steps. The first step is to randomly choose a random perturbation Δt^* to be applied to a randomly chosen chron boundary. The perturbations Δt^* are designed to sample a lognormal prior PDF of chron durations. The parameters of the lognormal prior PDF are the mean and standard deviation of the logarithms of the C13-C33 chron durations in the CK95 time scale (Cande & Kent 1992, 1995), which are 0.7138 and 1.108, respectively, for chron durations in Ma. The second step is to choose one of two moves with equal probability: either add the perturbation Δt^* to a single chosen chron boundary or to a range of chron boundaries around the chosen one. In the latter case, the perturbation is distributed over nearby chron boundaries, following a Gaussian function that equals Δt^* at the chosen chron boundary and has a standard deviation of 1 Ma. This combination of local and extended GPTS perturbations improves the convergence of the MCMC algorithm to sample the posterior PDF of the GPTS.

Similarly, the candidate CV vector $\mathbf{c}^*$ is determined by adding a random perturbation Δc^* to a randomly chosen CV. The perturbations are designed to sample a prior PDF that is log-uniform in a broad interval of possible values of CV (0.02 to 0.8).

MCMC sampling and convergence assessment

To ensure that the MCMC algorithm converged to sampling the posterior PDF of the GPTS, we followed the recommended strategy outlined in Section 11.10 of Gelman et al. (2004). We ran 10 independent sampling chains, where each chain was started from a randomly perturbed version of the CK95 GPTS, obtained by randomly changing the original chron boundary ages in an interval spanning ±30% of the chron durations. Each sampling chain ran for 200,000 iterations, and the sampled GPTSs were saved every 100 iterations.

To assess whether the chains converged to sample the posterior PDF, we computed for each sampled parameter of interest (GPTS ages in the vector **t**) a $\widehat{R}$ statistic that compares the variance of a parameter sampled within each chain to the variance of samples between different chains. The practical recommendation of Gelman et al. (2004) is that convergence is reached if the $\widehat{R}$ statistic is less than 1.1 for all parameters. In our GPTS sampling, this threshold is reached after about 30,000 iterations. We conservatively discard the first 50,000 iterations in each chain and assemble all the remaining samples in all the chains to compute a mean and standard deviation of GPTS chron boundary ages and chron durations (Table 4 in the main text).

Table S1. List of symbols.

$\mathbf{b}$	Vector of block model distances (BMDs)
$\mathbf{c}$	Vector of coefficients of variation of spreading rates (CVs)
$\mathbf{C}_b$	Covariance matrix of BMD uncertainties
$\mathbf{C}_u$	Covariance matrix of spreading rate uncertainties
$\mathbf{C}_r$	Covariance matrix of radioisotopic date uncertainties
$\mathbf{d}$	Vector of observed data
$\mathbf{d}_{\mathsf{pred}}$	Vector of data predicted by the parameter vector $\mathbf{m}$
$\mathbf{m}$	Model parameter vector
$\mathbf{m}^*$	Candidate model parameter vector in MCMC sampling
$\mathbf{r}$	Vector of observed radioisotopic dates
$\mathbf{r}_{\mathsf{pred}}$	Vector of radioisotopic dates predicted by the parameter vector $\mathbf{m}$
$\mathbf{t}$	Vector of chron boundary ages in the GPTS
$\mathbf{u}$	Vector of spreading rates in a ridge flank region
$\overline{u}$	Weighted average of spreading rates in a ridge flank region
σ_e	Standard deviation of misfit between observed and predicted data

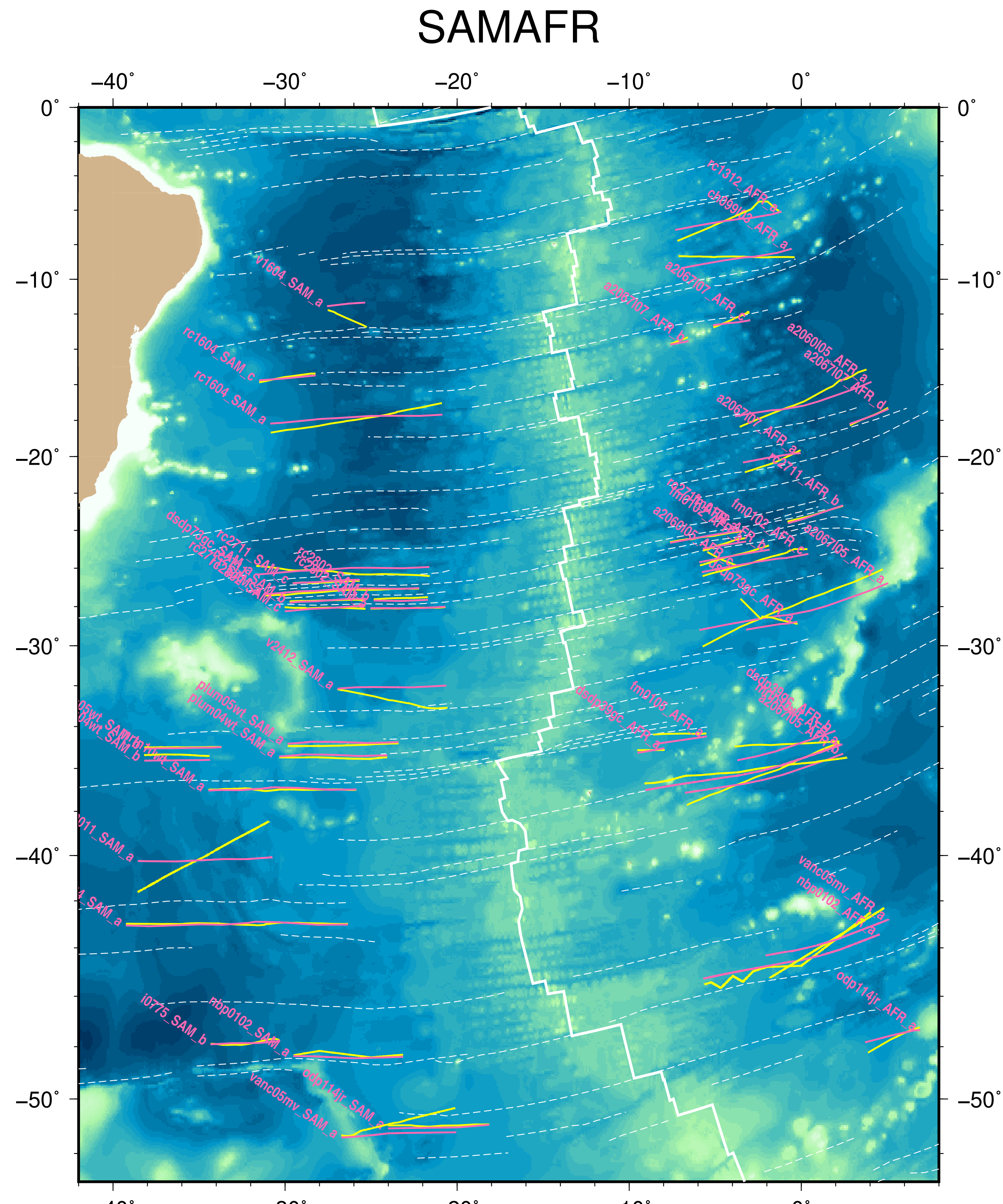

Figure S1. Original ship tracks (yellow) and tracks projected onto flow lines (magenta) in the SAMAFR-SAM and SAMAFR-AFR ridge flank regions.

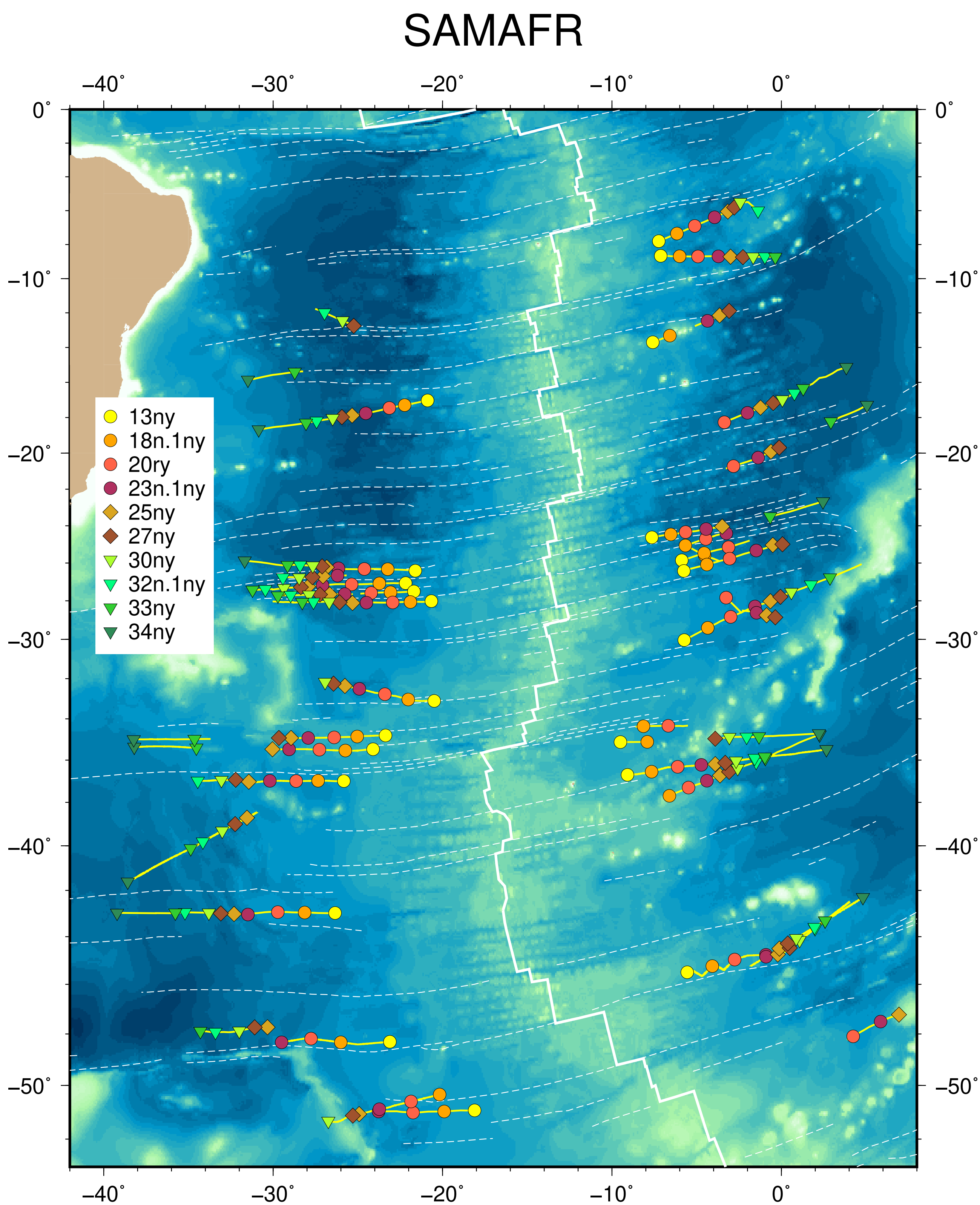

Figure S2. Location of selected magnetic block boundaries on original ship tracks in the SAMAFR-SAM and SAMAFR-AFR ridge flank regions.

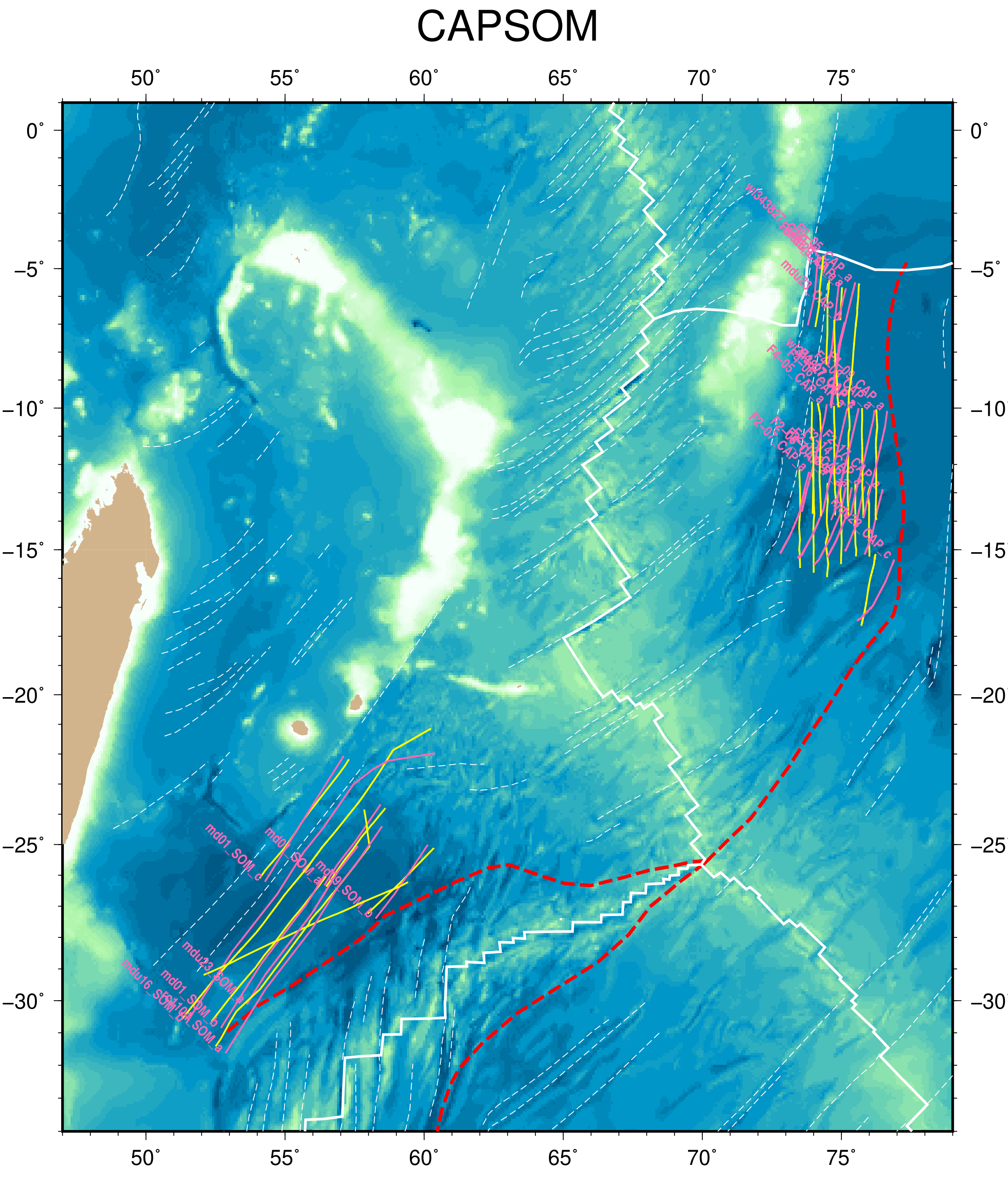

Figure S3. Original ship tracks (yellow) and tracks projected onto flow lines (magenta) in the CAPSOM-SOM and CAPSOM-CAP ridge flank regions.

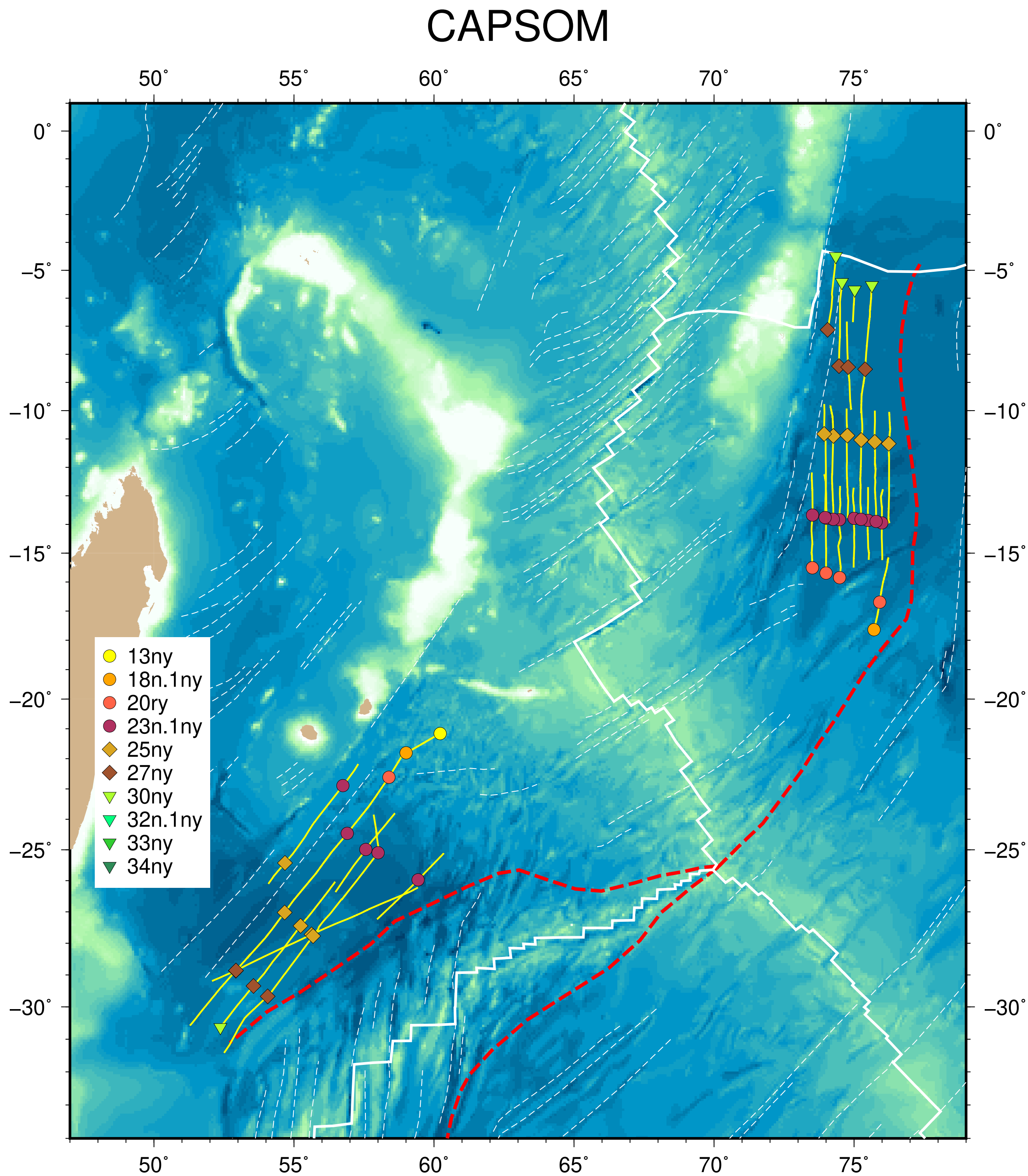

Figure S4. Location of selected magnetic block boundaries on original ship tracks in the CAPSOM-SOM and CAPSOM-CAP ridge flank regions.

CAPANT

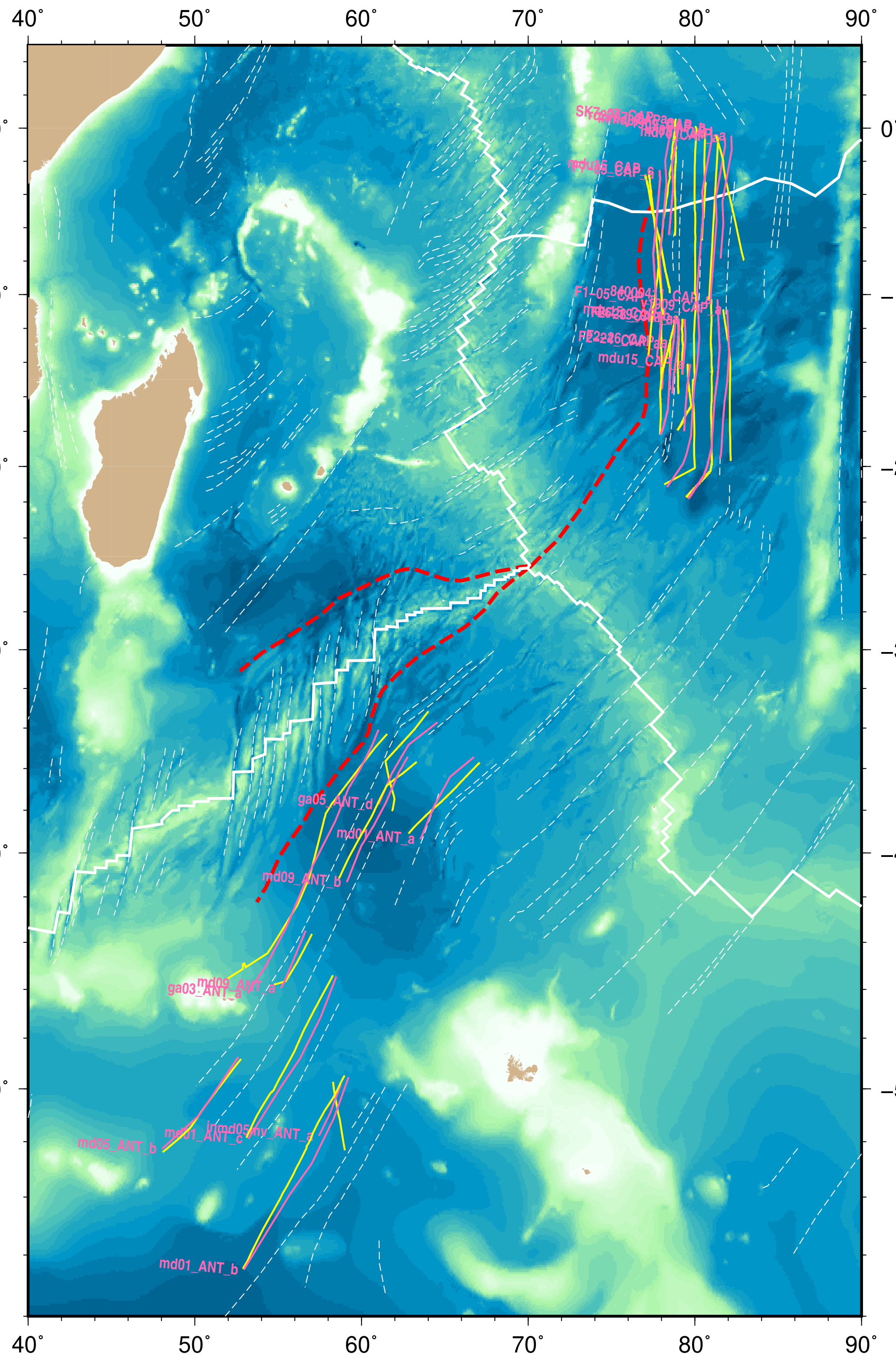

Figure S5. Original ship tracks (yellow) and tracks projected onto flow lines (magenta) in the CAPANT-ANT and CAPANT-CAP ridge flank regions.

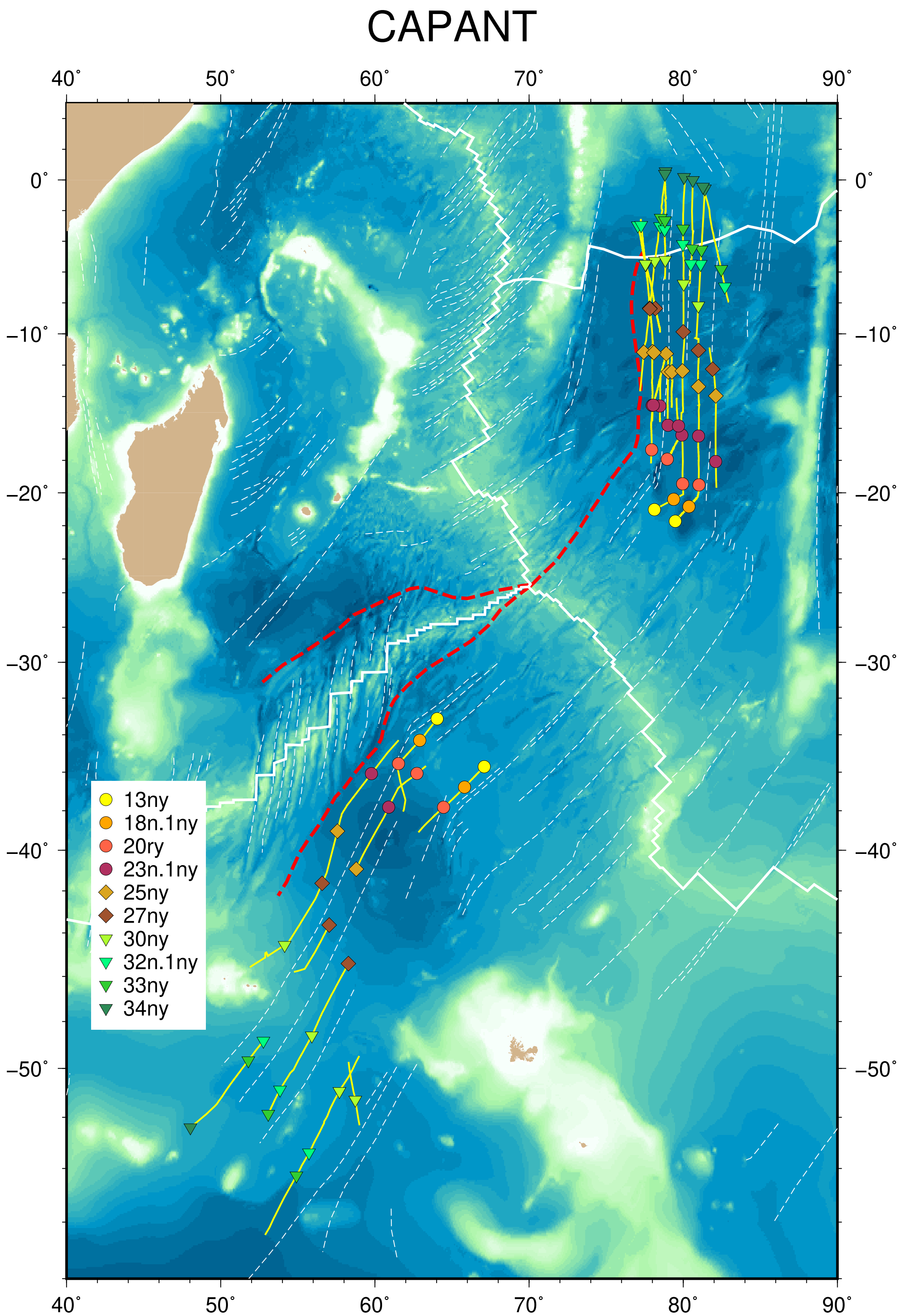

Figure S6. Location of selected magnetic block boundaries on original ship tracks in the CAPANT-ANT and CAPANT-CAP ridge flank regions.

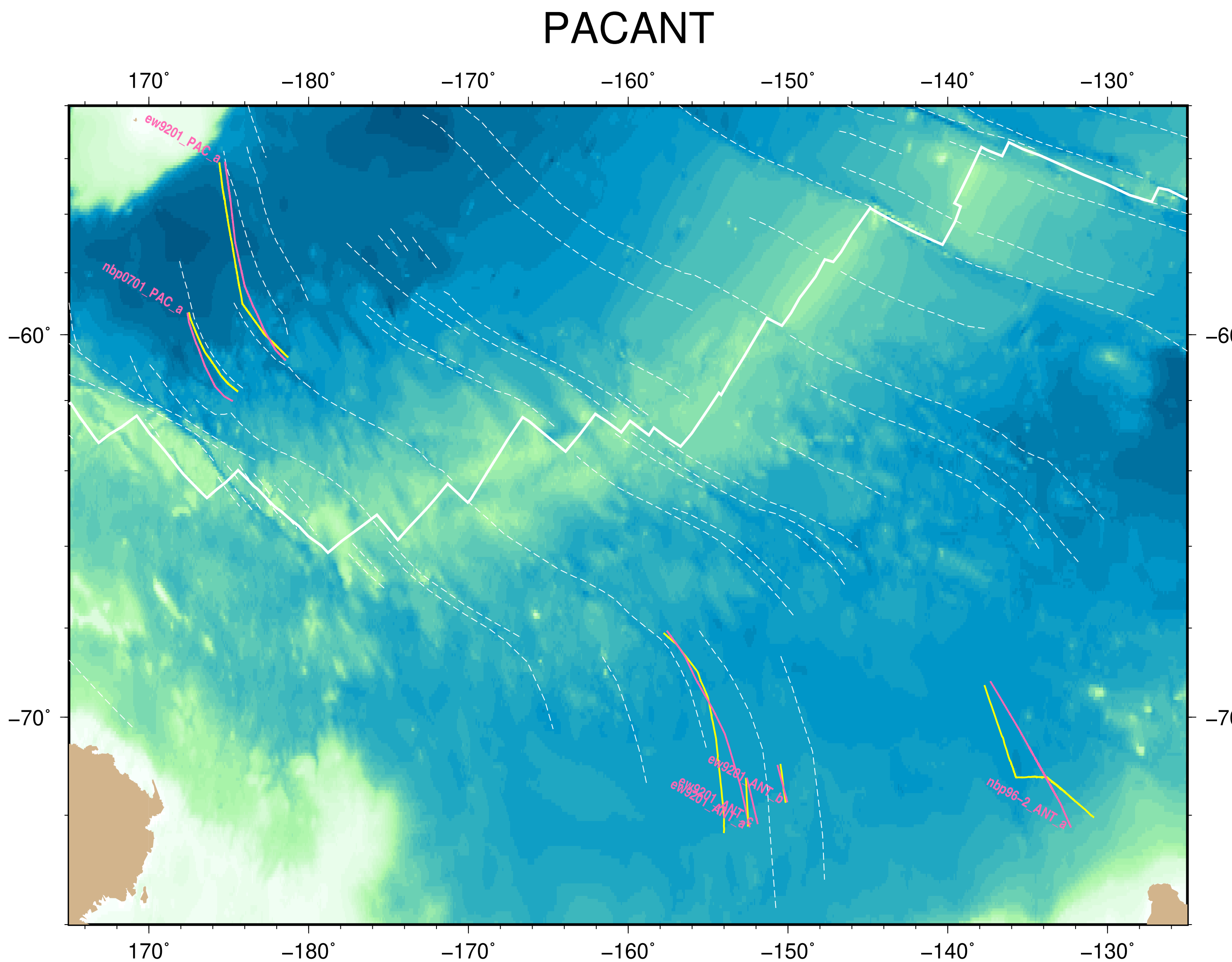

Figure S7. Original ship tracks (yellow) and tracks projected onto flow lines (magenta) in the PACANT-PAC and PACANT-ANT ridge flank regions.

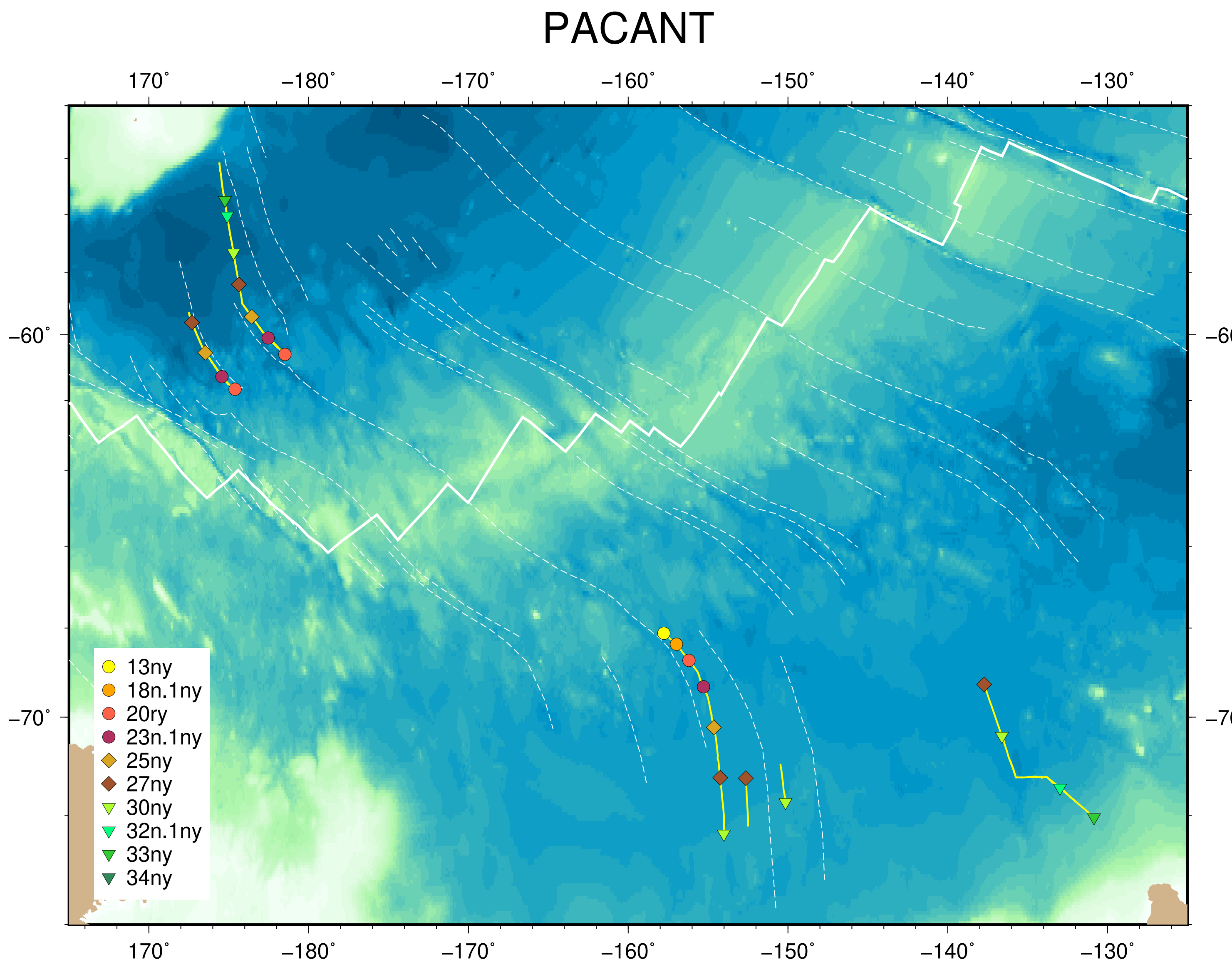

Figure S8. Location of selected magnetic block boundaries on original ship tracks in the PACANT-PAC and PACANT-ANT ridge flank regions.

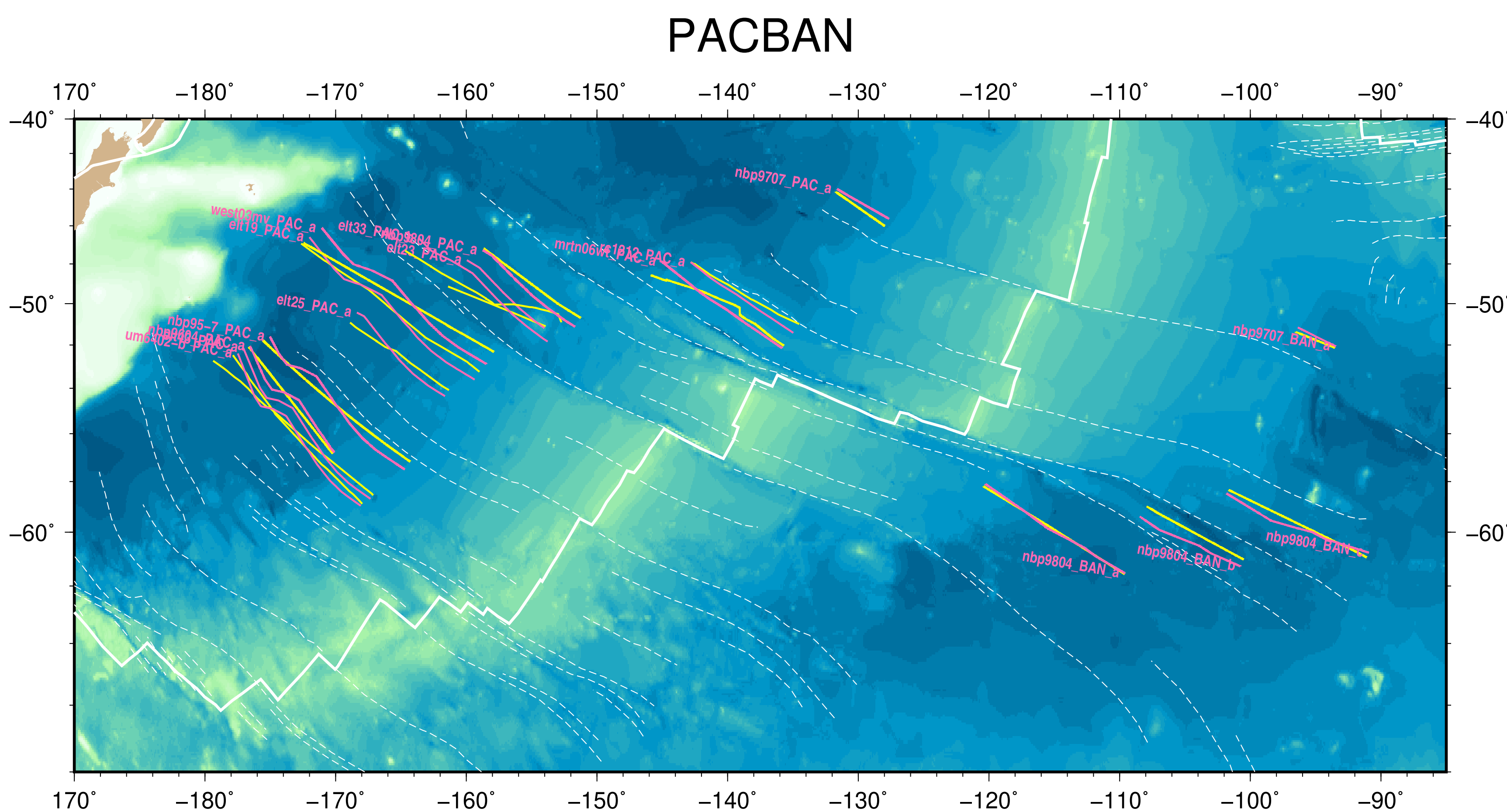

Figure S9. Original ship tracks (yellow) and tracks projected onto flow lines (magenta) in the PACBAN-PAC and PACBAN-BAN ridge flank regions.

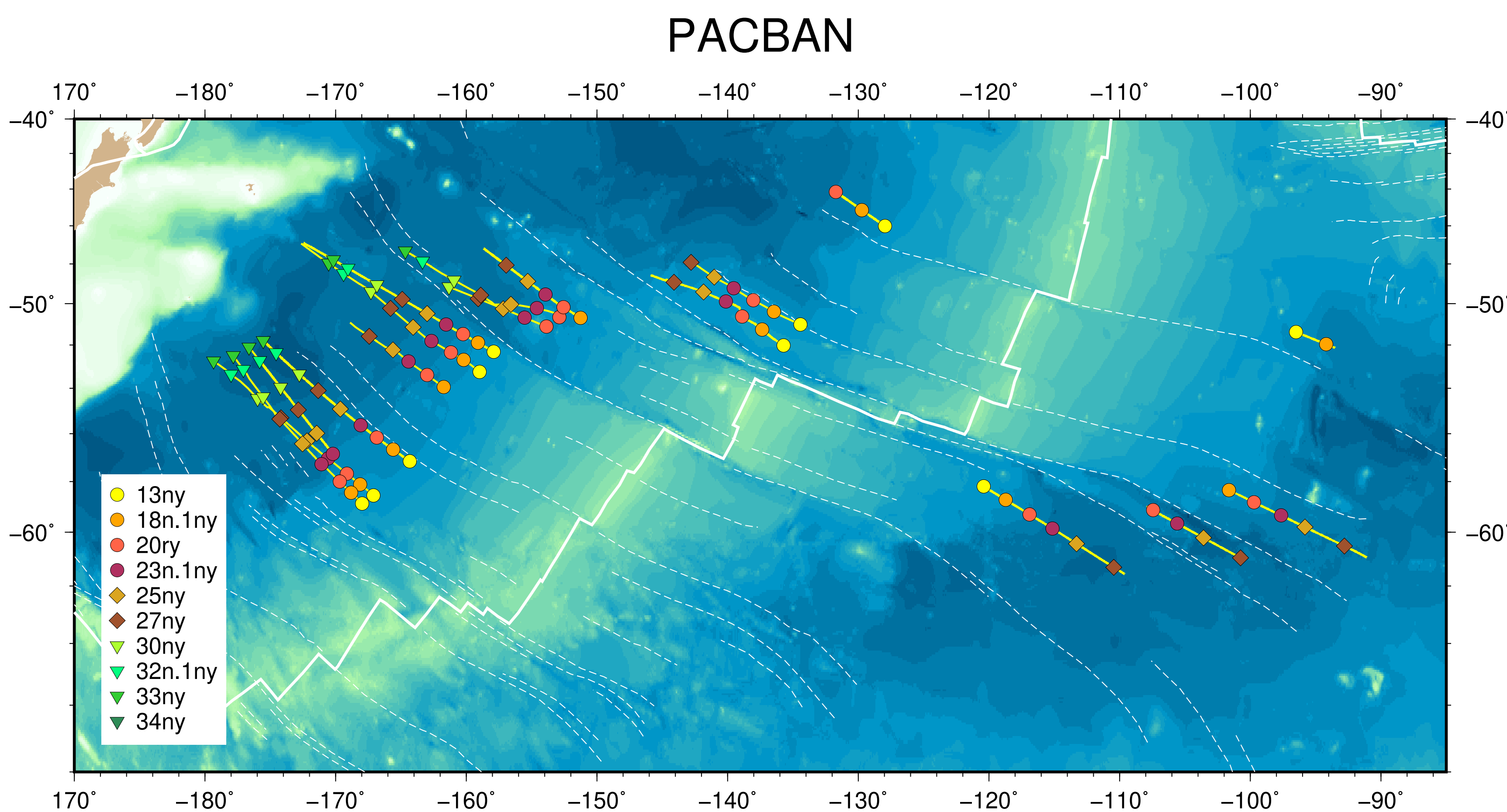

Figure S10. Location of selected magnetic block boundaries on original ship tracks in the PACBAN-PAC and PACBAN-BAN ridge flank regions.

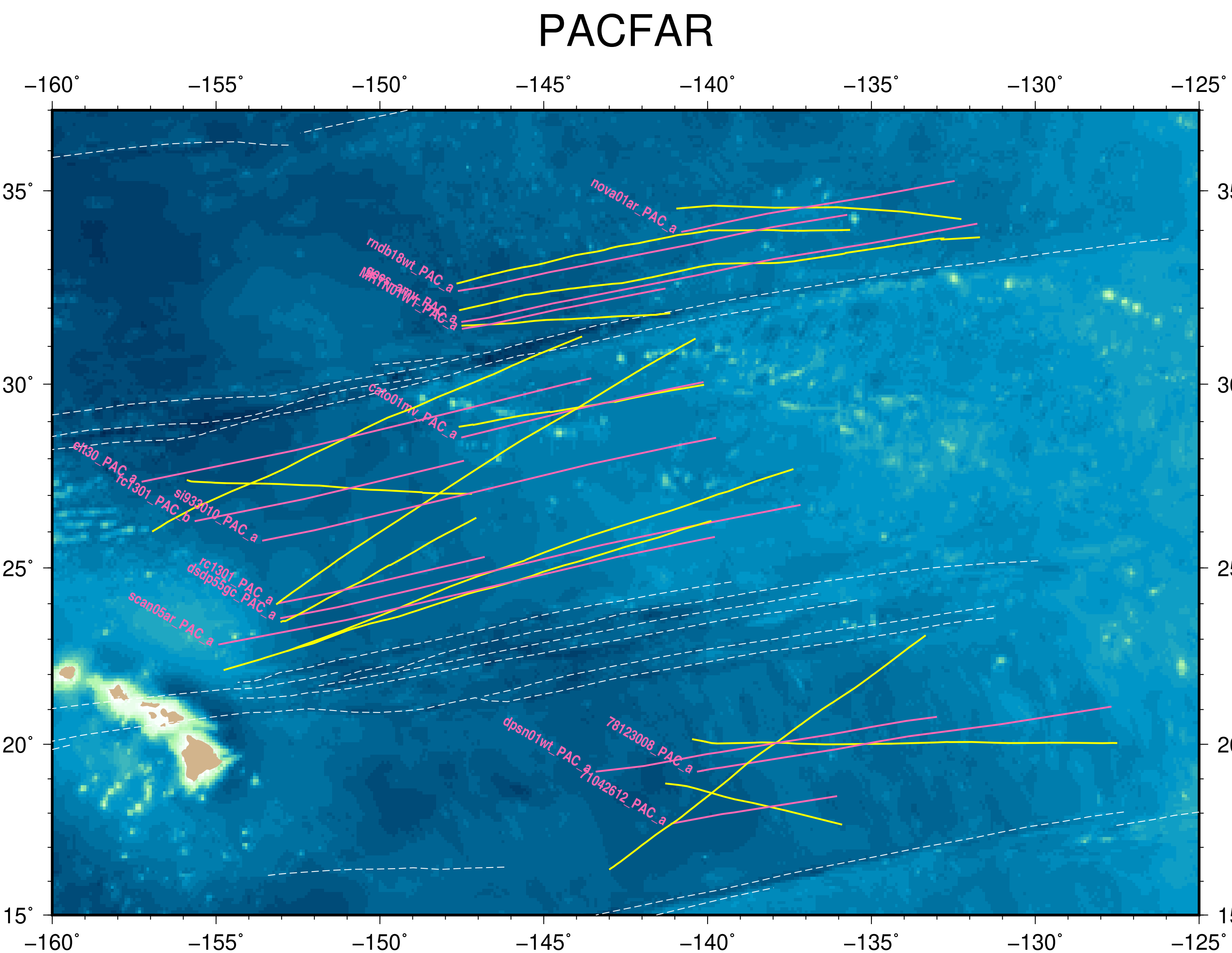

Figure S11. Original ship tracks (yellow) and tracks projected onto flow lines (magenta) in the PACFAR-PAC ridge flank region.

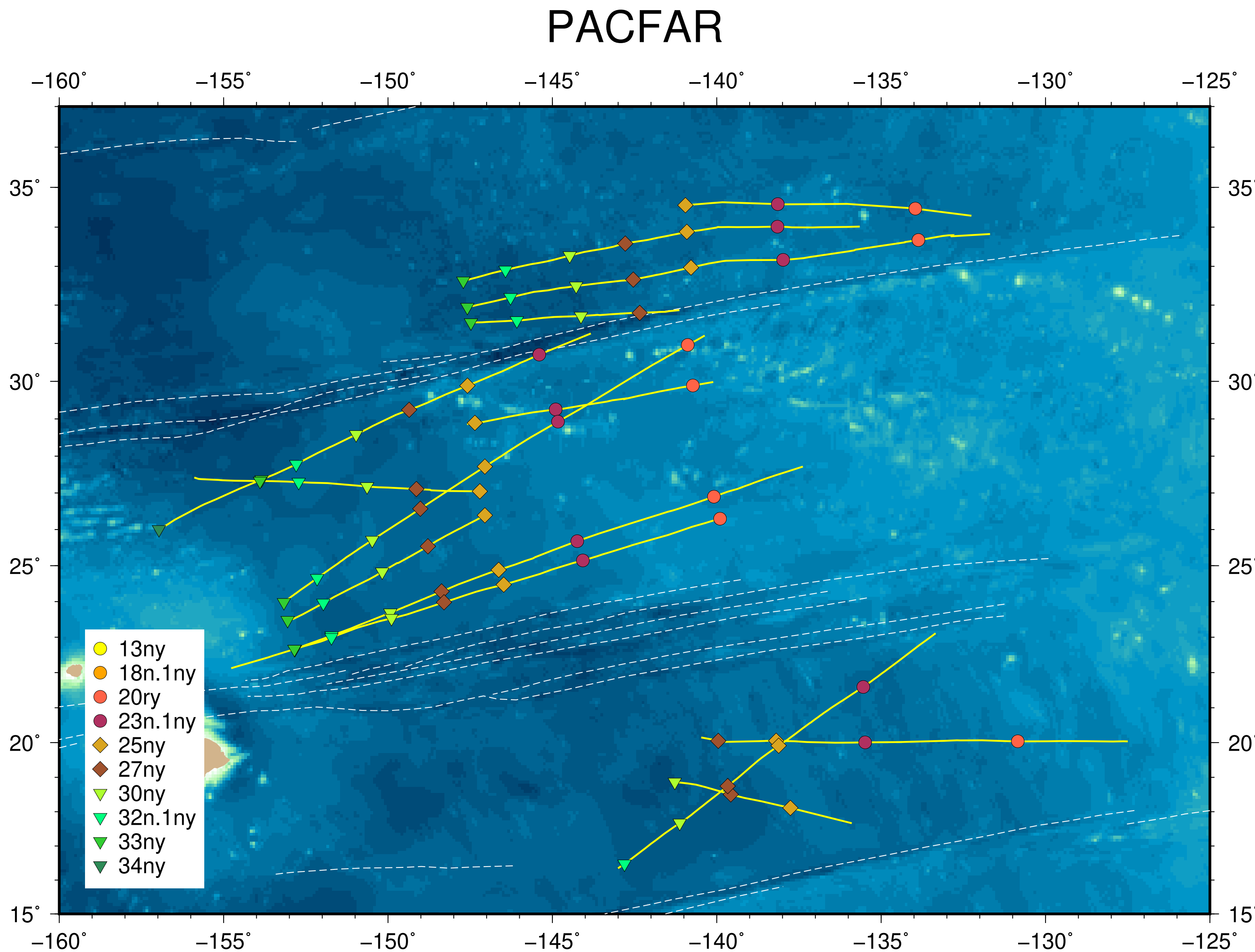

Figure S12. Location of selected magnetic block boundaries on original ship tracks in the PACFAR-PAC ridge flank region.

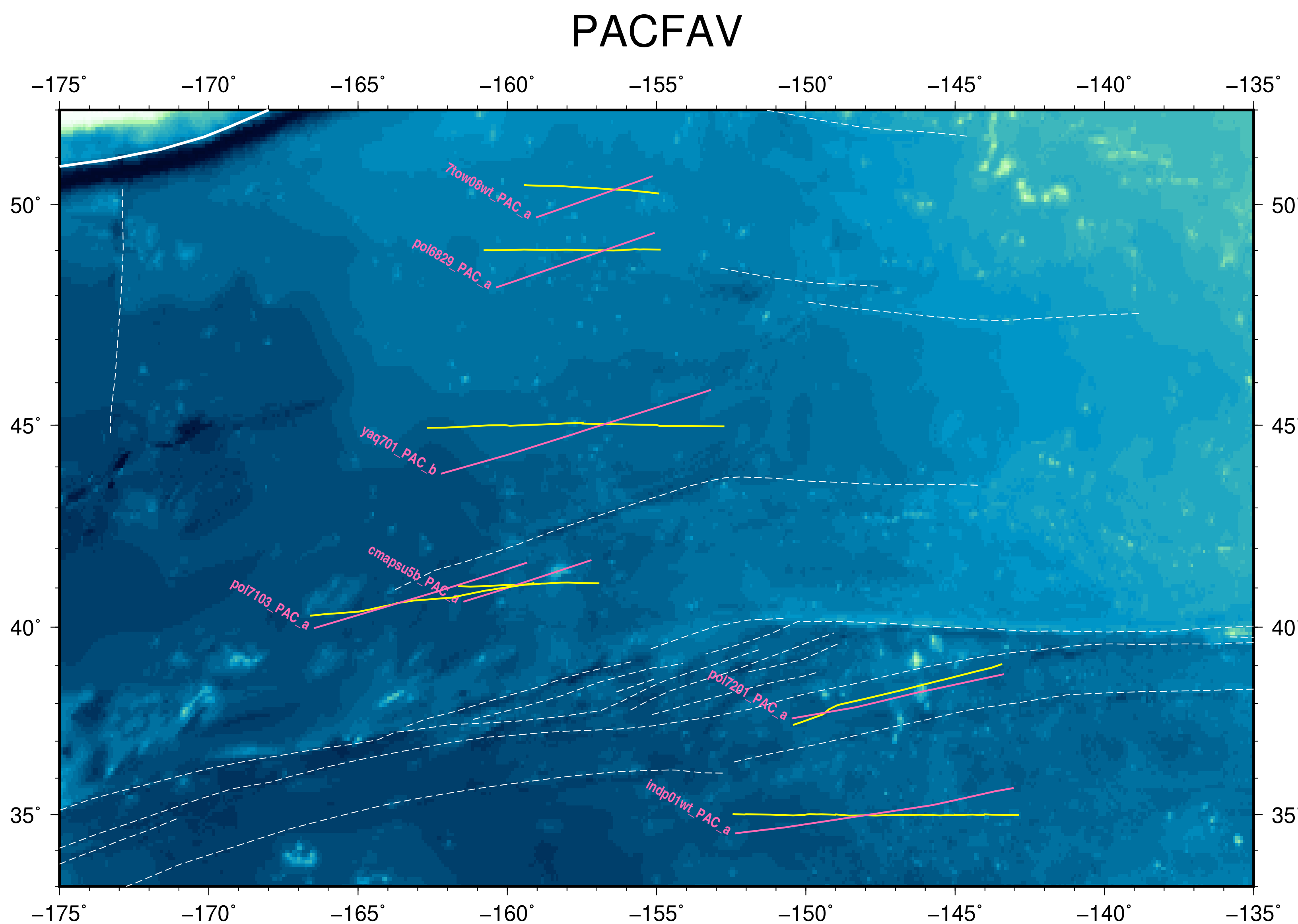

Figure S13. Original ship tracks (yellow) and tracks projected onto flow lines (magenta) in the PACFAV-PAC ridge flank region.

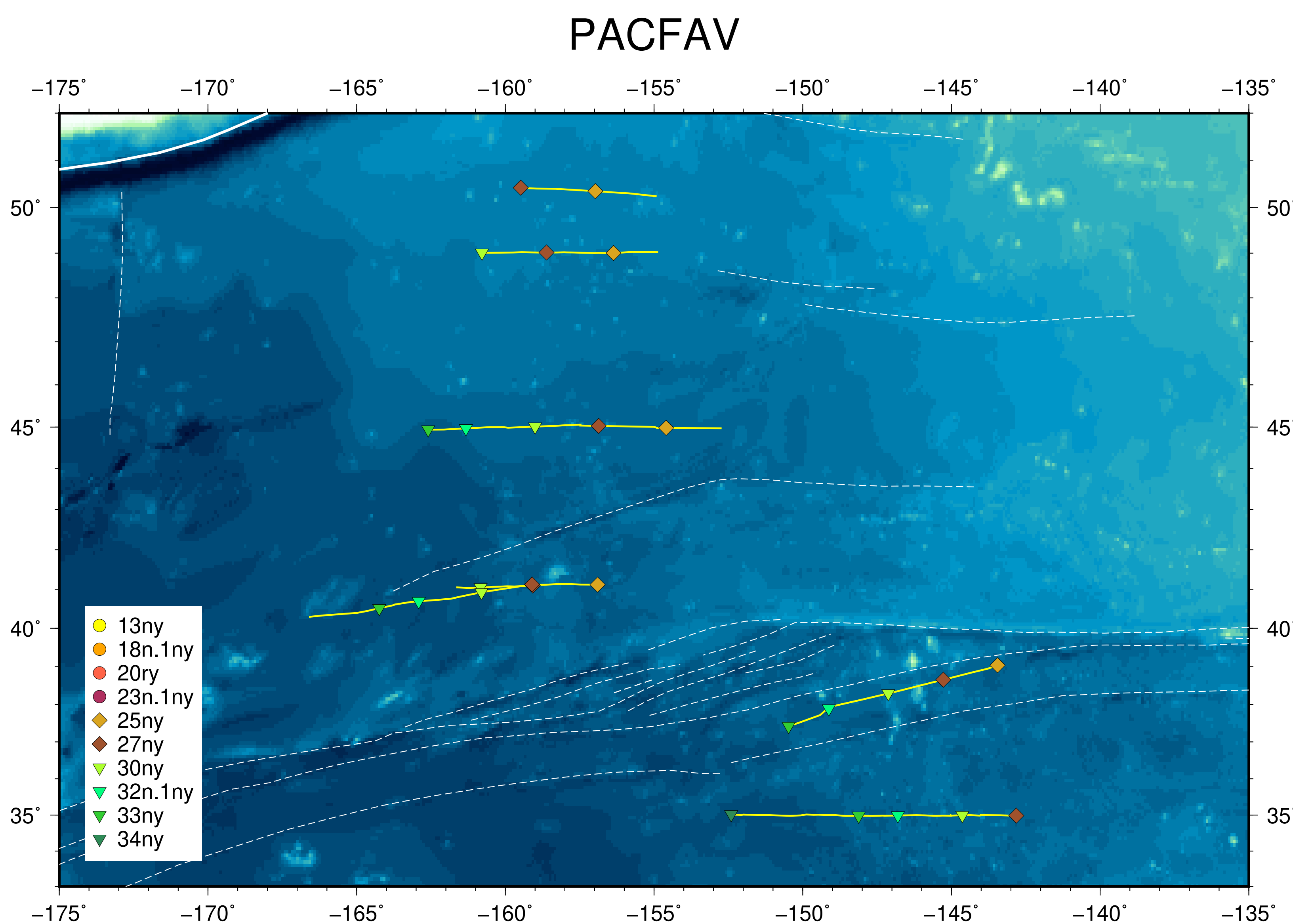

Figure S14. Location of selected magnetic block boundaries on original ship tracks in the PACFAV-PAC ridge flank region.

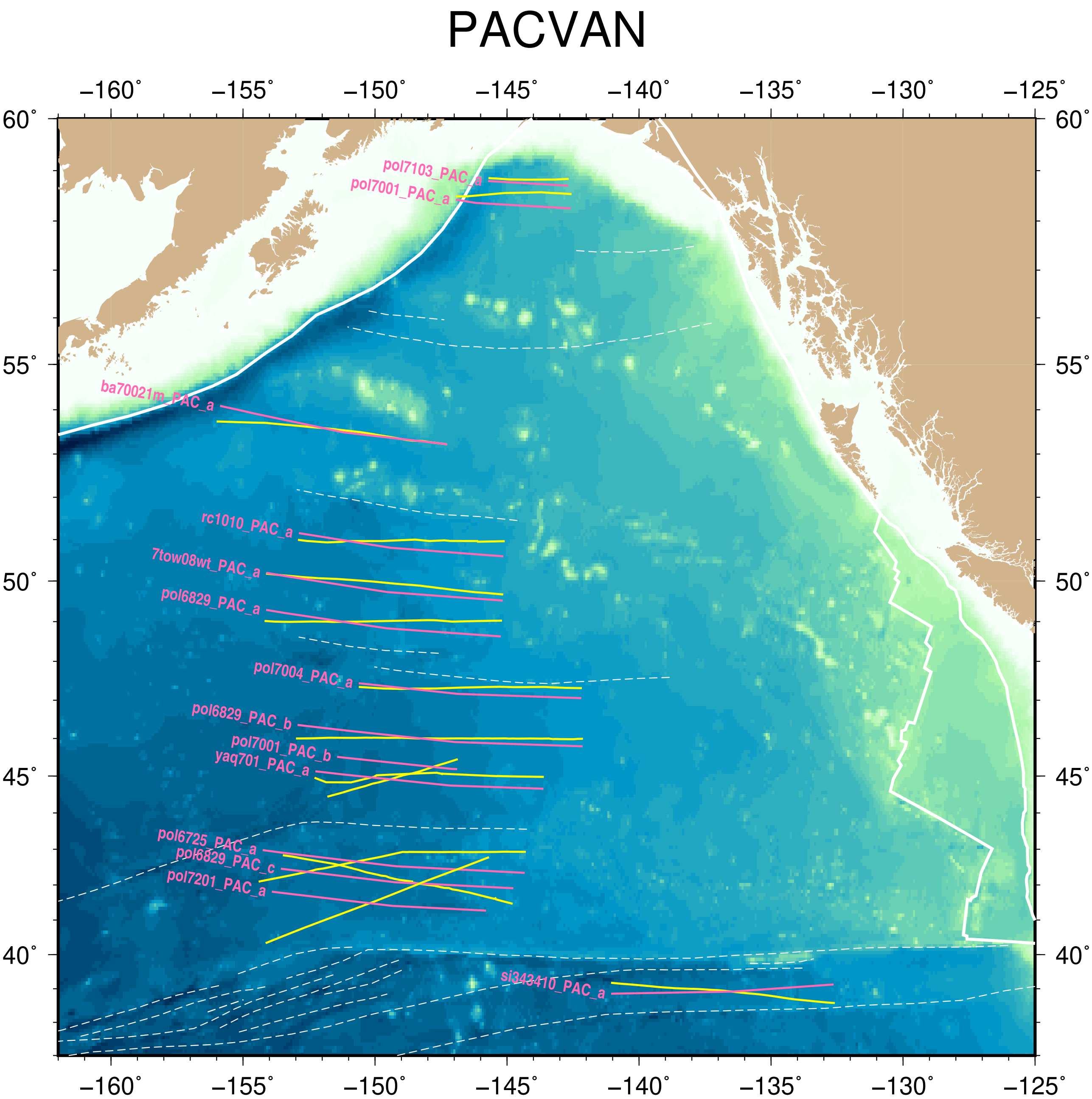

Figure S15. Original ship tracks (yellow) and tracks projected onto flow lines (magenta) in the PACVAN-PAC ridge flank region.

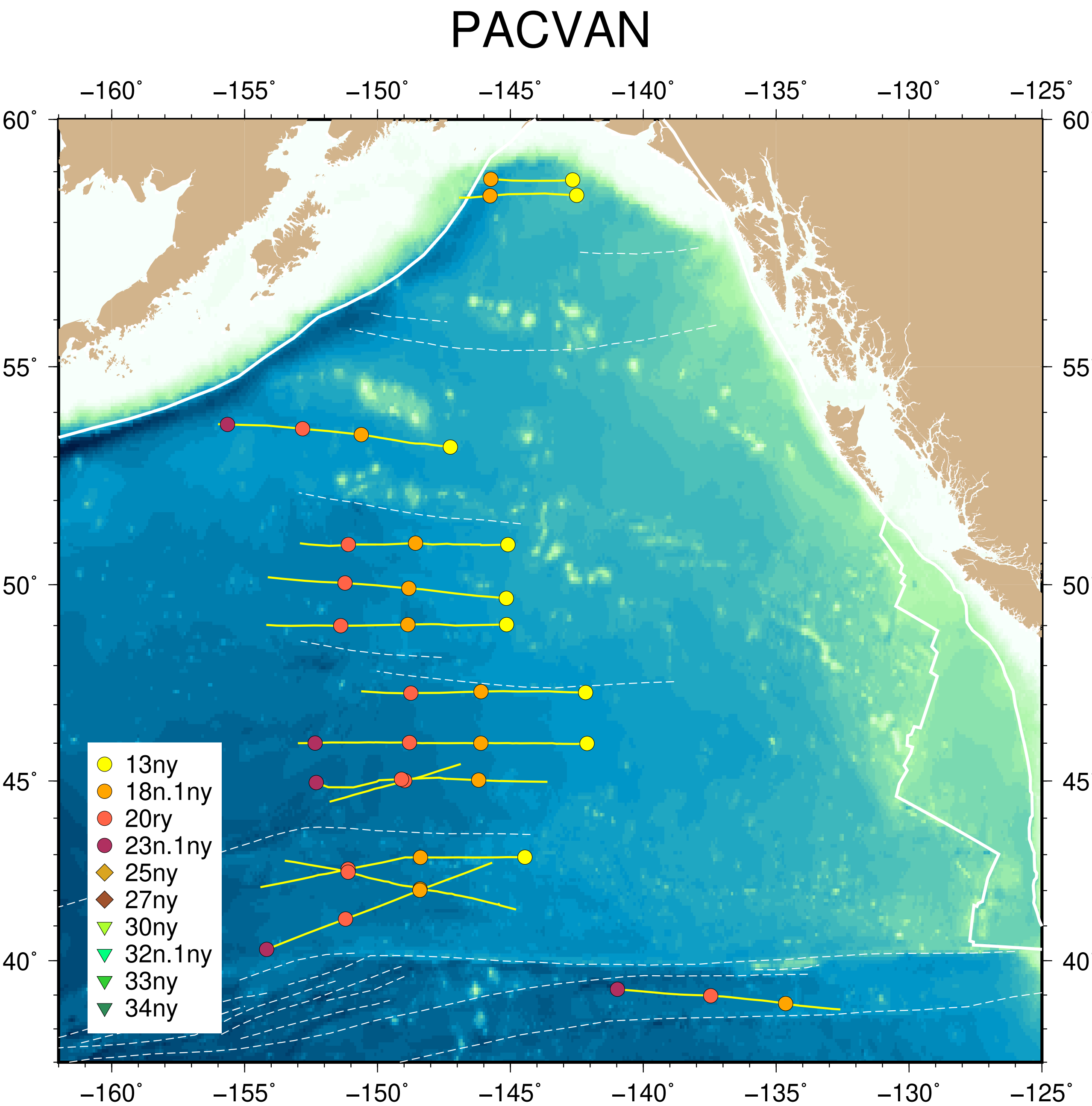

Figure S16. Location of selected magnetic block boundaries on original ship tracks in the PACVAN-PAC ridge flank region.

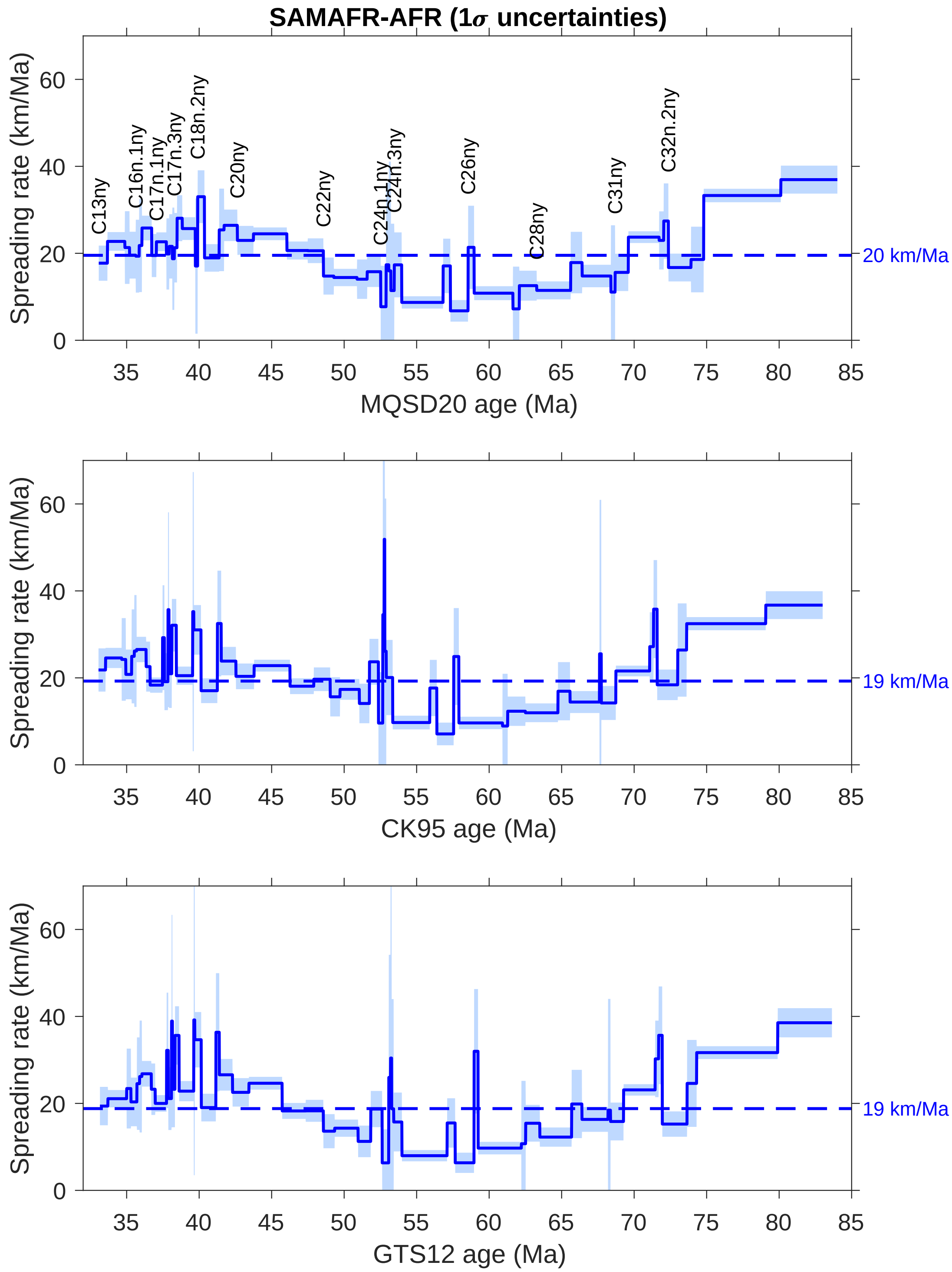

Figure S17. Half-spreading rates in the SAMAFR-AFR ridge flank region for different GPTSs: MQSD20 (this paper), CK95 (Cande & Kent 1992, 1995), and GTS12 (Ogg 2012). The shaded areas show 1σ uncertainties in spreading rate, computed from the uncertainties in BMDs as the square root of the diagonal of matrix $\mathbf{C}_1$ (Equation 7).

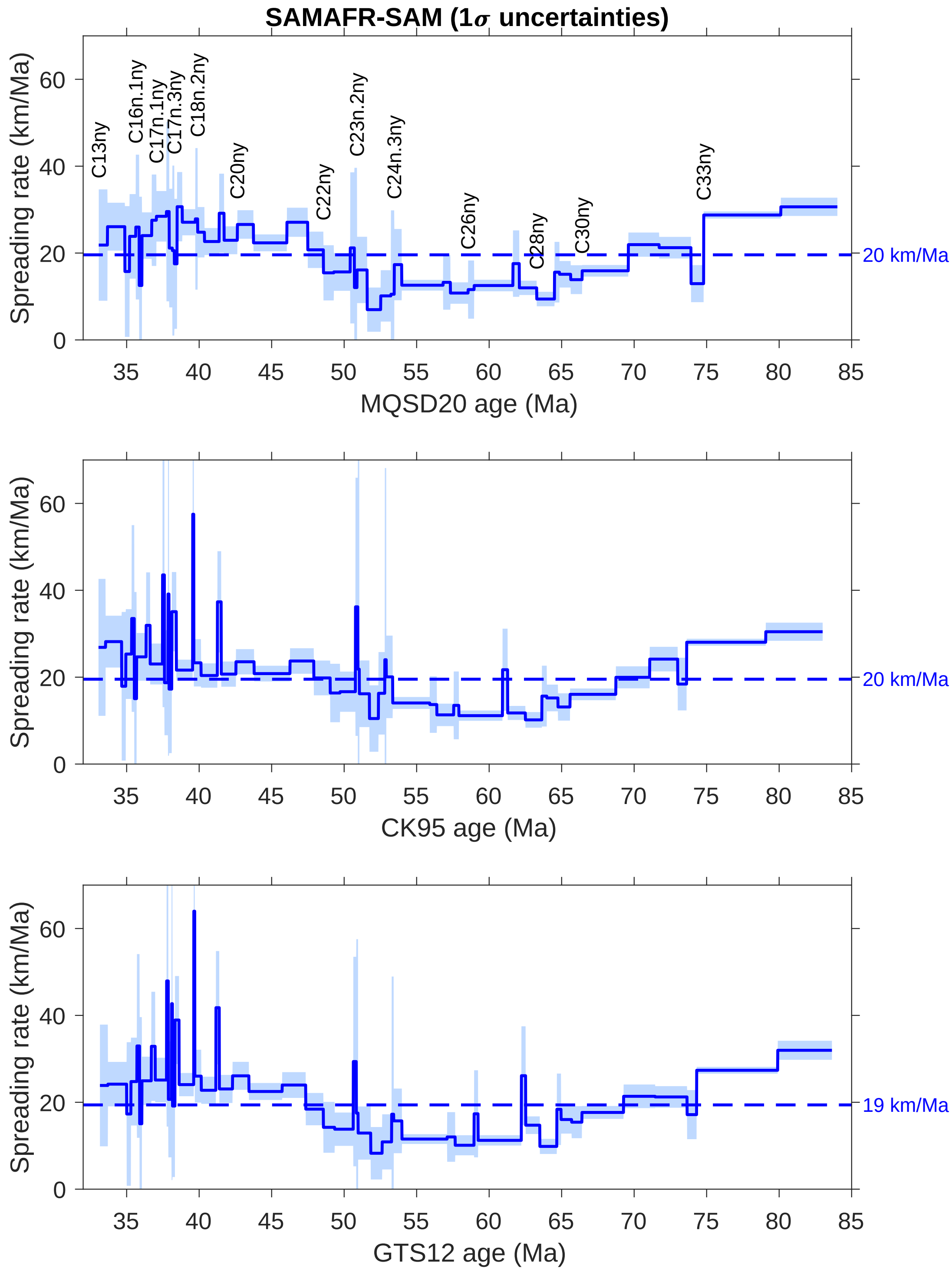

Figure S18. Half-spreading rates in the SAMAFR-SAM ridge flank region for different GPTSs: MQSD20 (this paper), CK95 (Cande & Kent 1992, 1995), and GTS12 (Ogg 2012). The shaded areas show 1σ uncertainties in spreading rate, computed from the uncertainties in BMDs as the square root of the diagonal of matrix $\mathbf{C}_1$ (Equation 7).

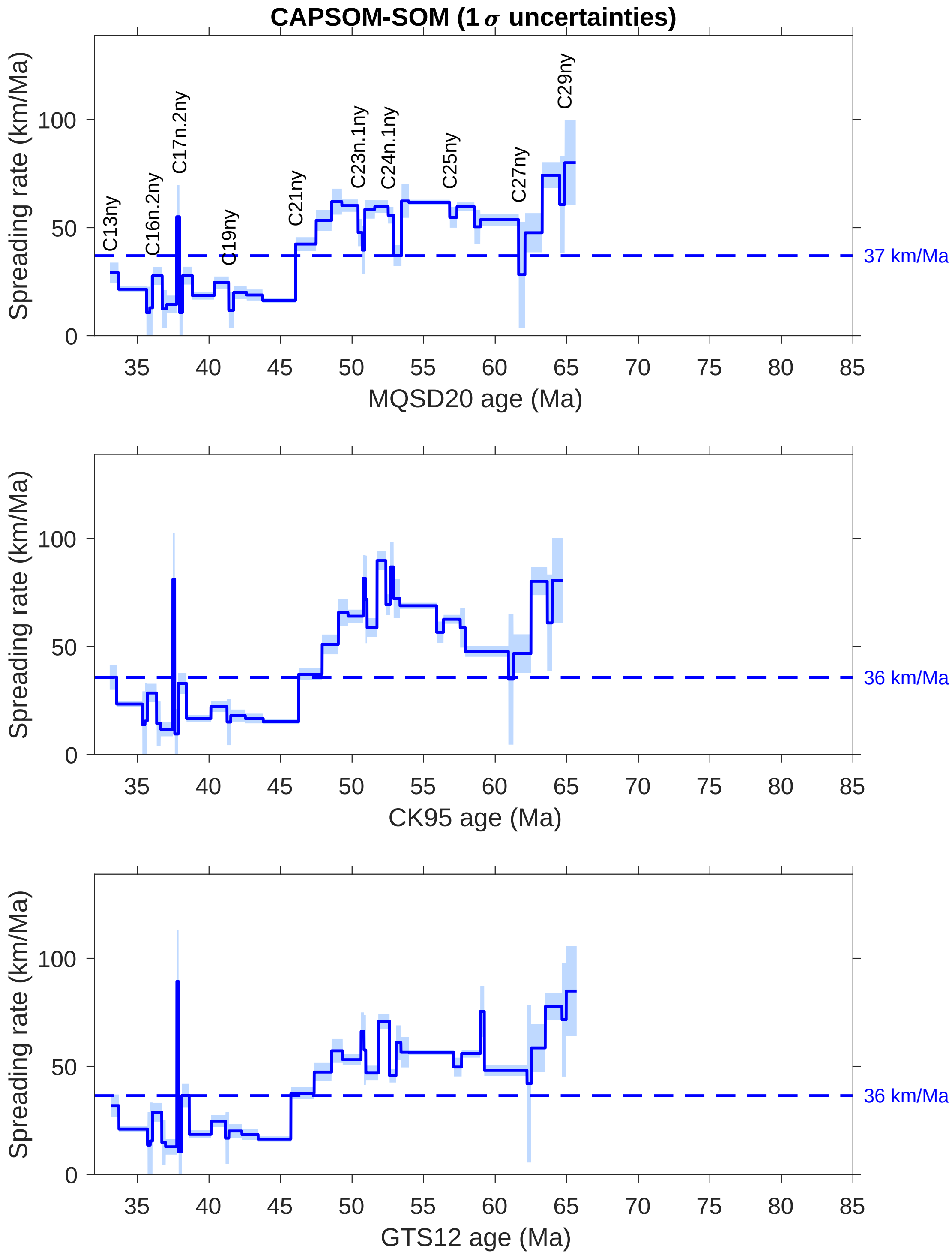

Figure S19. Half-spreading rates in the CAPSOM-SOM ridge flank region for different GPTSs: MQSD20 (this paper), CK95 (Cande & Kent 1992, 1995), and GTS12 (Ogg 2012). The shaded areas show 1σ uncertainties in spreading rate, computed from the uncertainties in BMDs as the square root of the diagonal of matrix $\mathbf{C}_1$ (Equation 7).

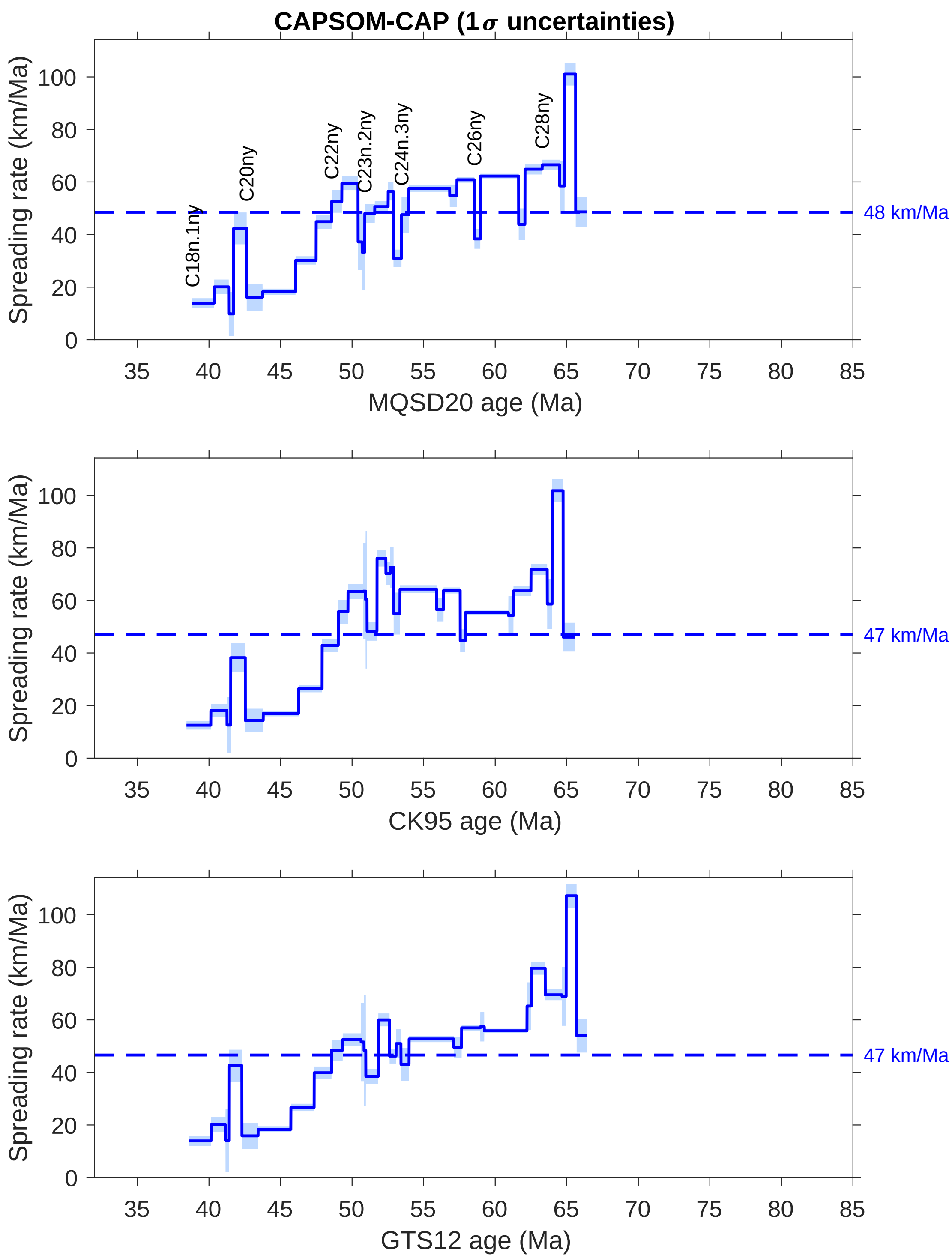

Figure S20. Half-spreading rates in the CAPSOM-CAP ridge flank region for different GPTSs: MQSD20 (this paper), CK95 (Cande & Kent 1992, 1995), and GTS12 (Ogg 2012). The shaded areas show 1σ uncertainties in spreading rate, computed from the uncertainties in BMDs as the square root of the diagonal of matrix $\mathbf{C}_1$ (Equation 7).

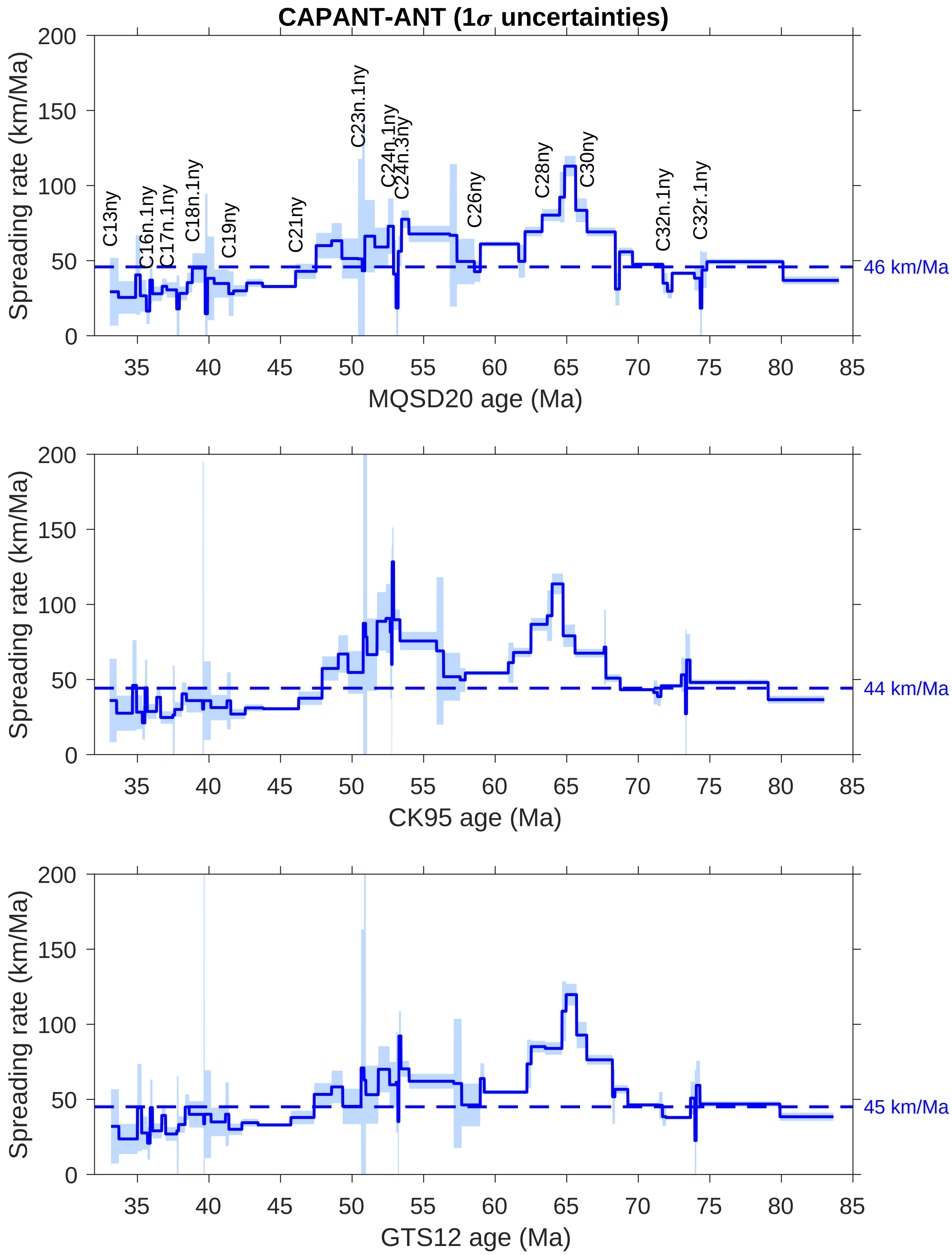

Figure S21. Half-spreading rates in the CAPANT-ANT ridge flank region for different GPTSs: MQSD20 (this paper), CK95 (Cande & Kent 1992, 1995), and GTS12 (Ogg 2012). The shaded areas show 1σ uncertainties in spreading rate, computed from the uncertainties in BMDs as the square root of the diagonal of matrix $\mathbf{C}_1$ (Equation 7).

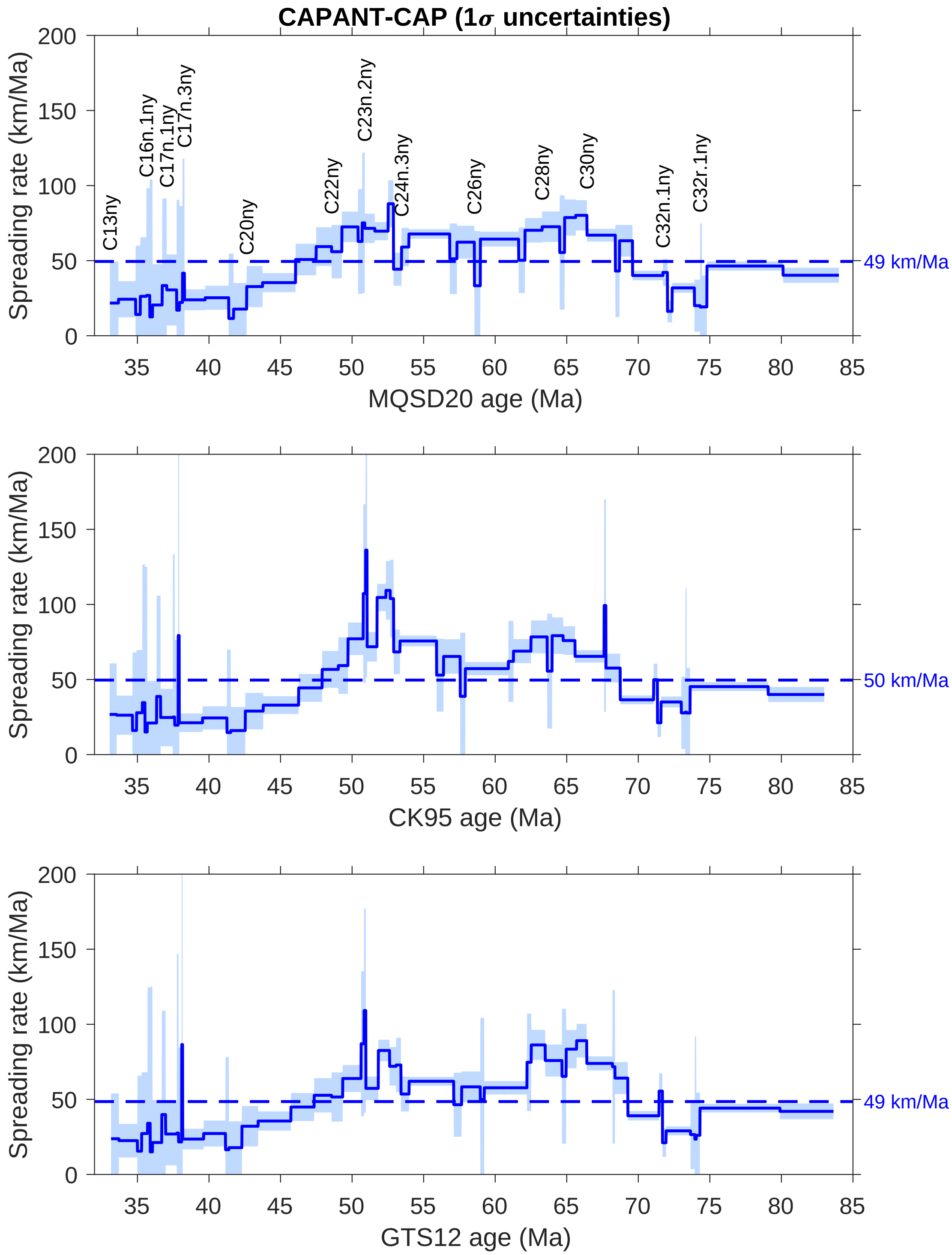

Figure S22. Half-spreading rates in the CAPANT-CAP ridge flank region for different GPTSs: MQSD20 (this paper), CK95 (Cande & Kent 1992, 1995), and GTS12 (Ogg 2012). The shaded areas show 1σ uncertainties in spreading rate, computed from the uncertainties in BMDs as the square root of the diagonal of matrix $\mathbf{C}_1$ (Equation 7).

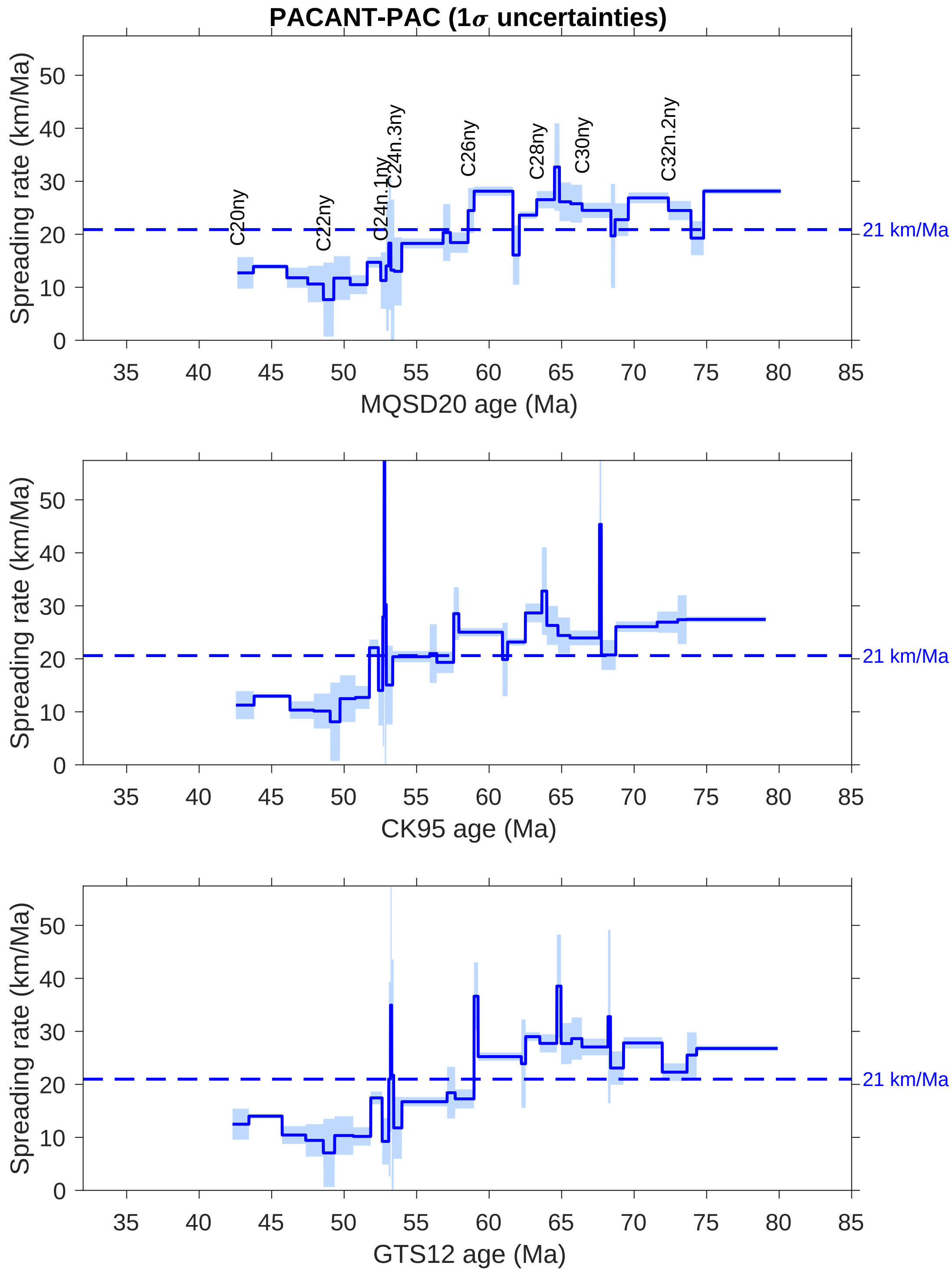

Figure S23. Half-spreading rates in the PACANT-PAC ridge flank region for different GPTSs: MQSD20 (this paper), CK95 (Cande & Kent 1992, 1995), and GTS12 (Ogg 2012). The shaded areas show 1σ uncertainties in spreading rate, computed from the uncertainties in BMDs as the square root of the diagonal of matrix $\mathbf{C}_1$ (Equation 7).

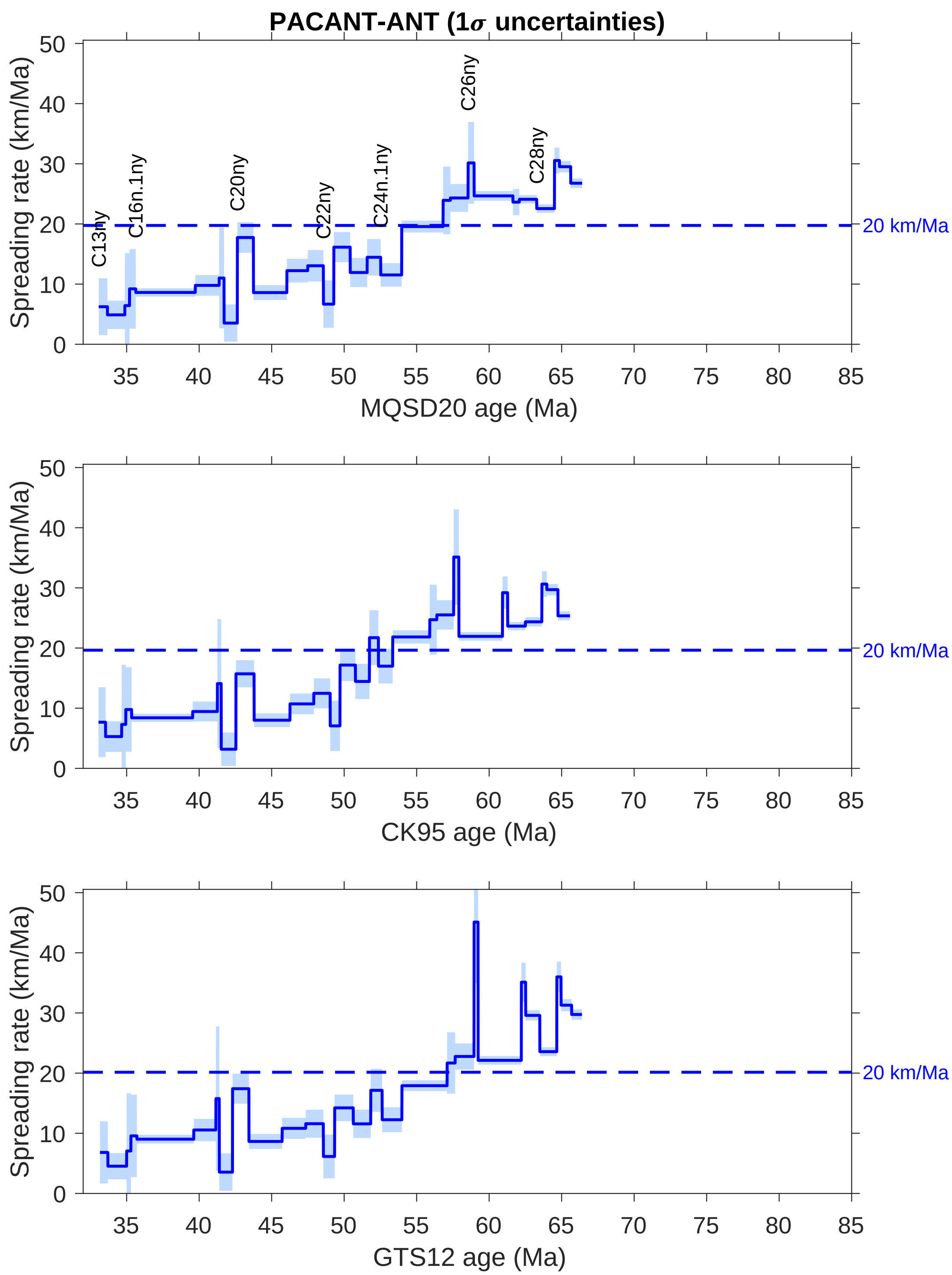

Figure S24. Half-spreading rates in the PACANT-ANT ridge flank region for different GPTSs: MQSD20 (this paper), CK95 (Cande & Kent 1992, 1995), and GTS12 (Ogg 2012). The shaded areas show 1σ uncertainties in spreading rate, computed from the uncertainties in BMDs as the square root of the diagonal of matrix $\mathbf{C}_1$ (Equation 7).

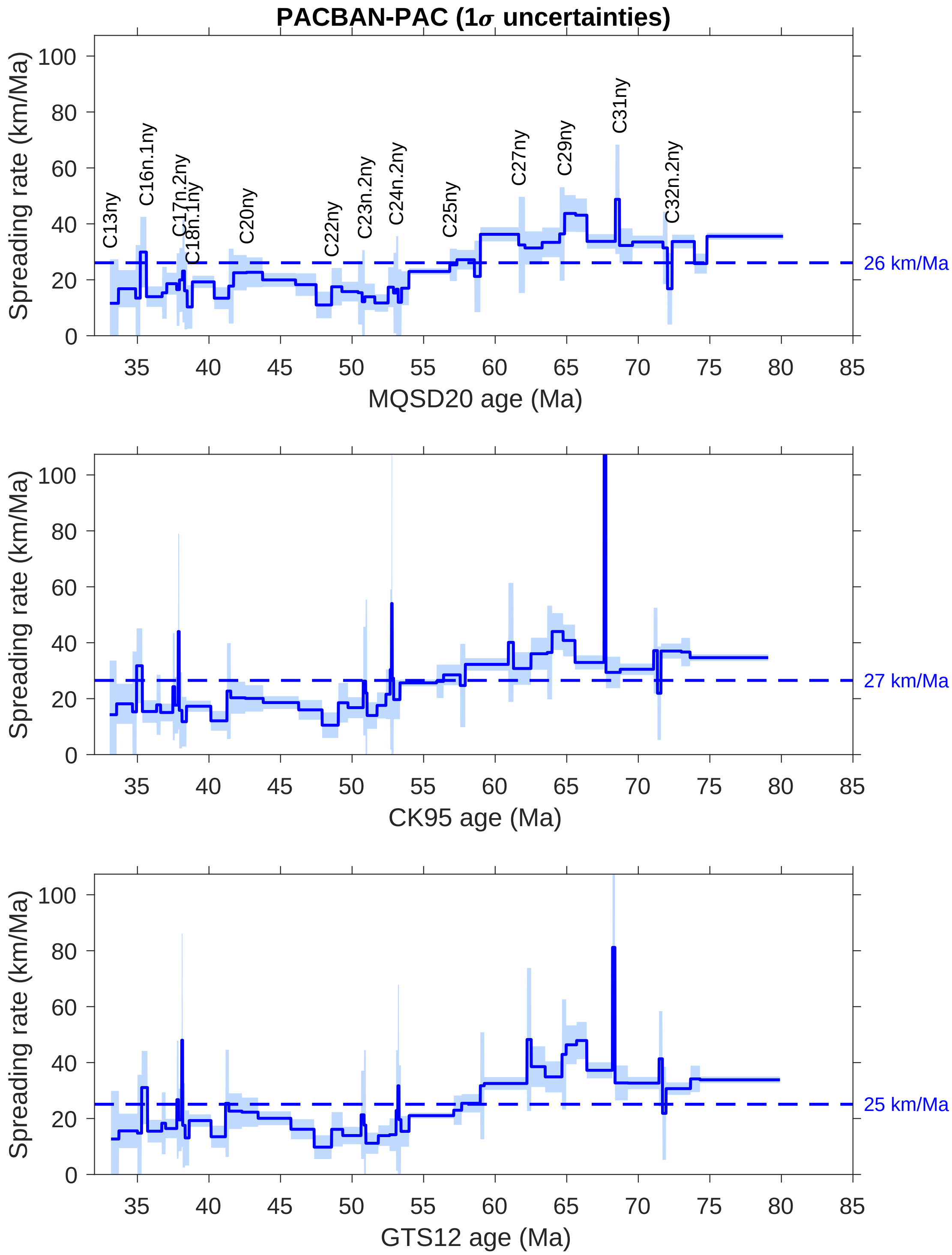

Figure S25. Half-spreading rates in the PACBAN-PAC ridge flank region for different GPTSs: MQSD20 (this paper), CK95 (Cande & Kent 1992, 1995), and GTS12 (Ogg 2012). The shaded areas show 1σ uncertainties in spreading rate, computed from the uncertainties in BMDs as the square root of the diagonal of matrix $\mathbf{C}_1$ (Equation 7).

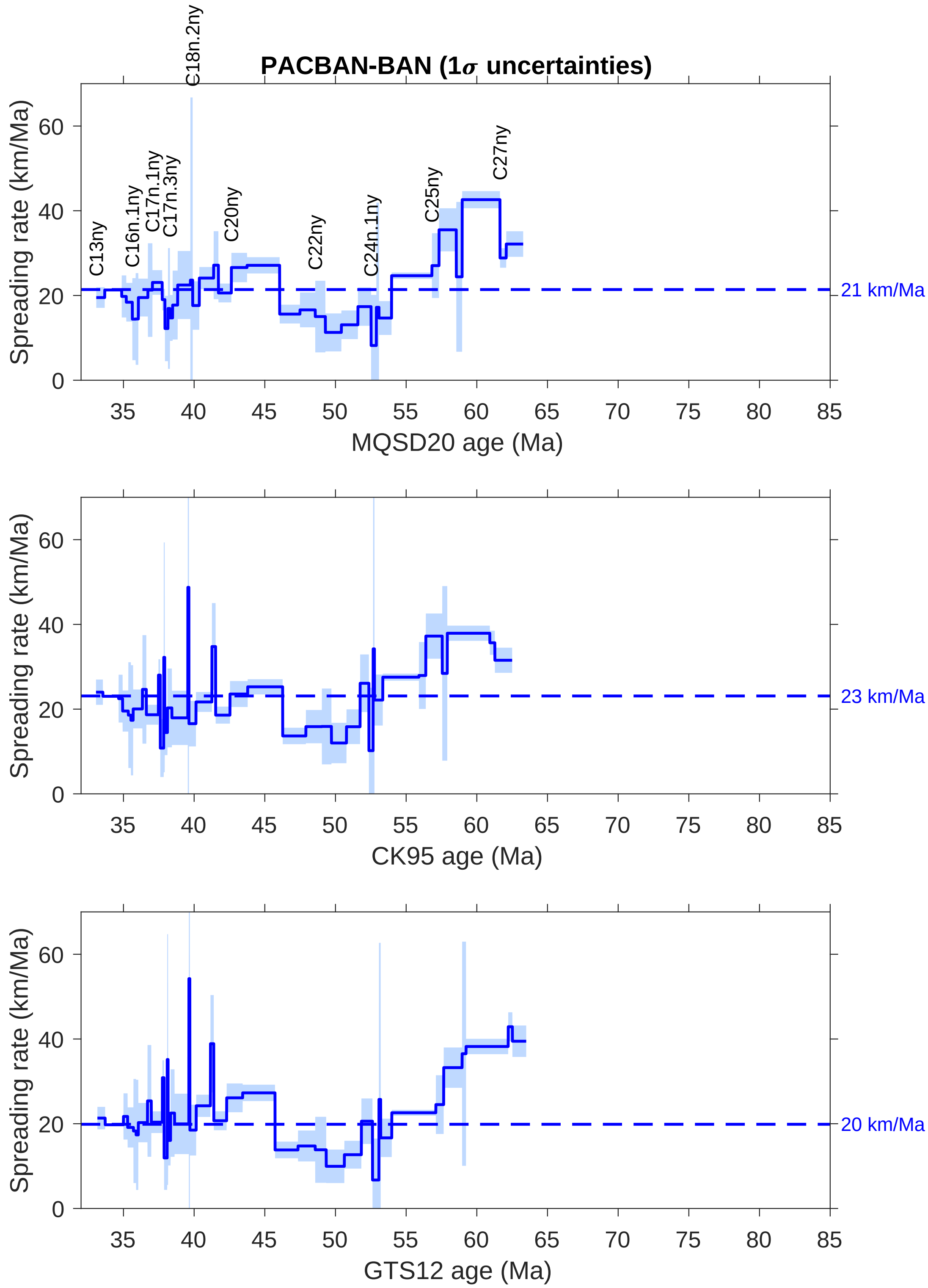

Figure S26. Half-spreading rates in the PACBAN-BAN ridge flank region for different GPTSs: MQSD20 (this paper), CK95 (Cande & Kent 1992, 1995), and GTS12 (Ogg 2012). The shaded areas show 1σ uncertainties in spreading rate, computed from the uncertainties in BMDs as the square root of the diagonal of matrix $\mathbf{C}_1$ (Equation 7).

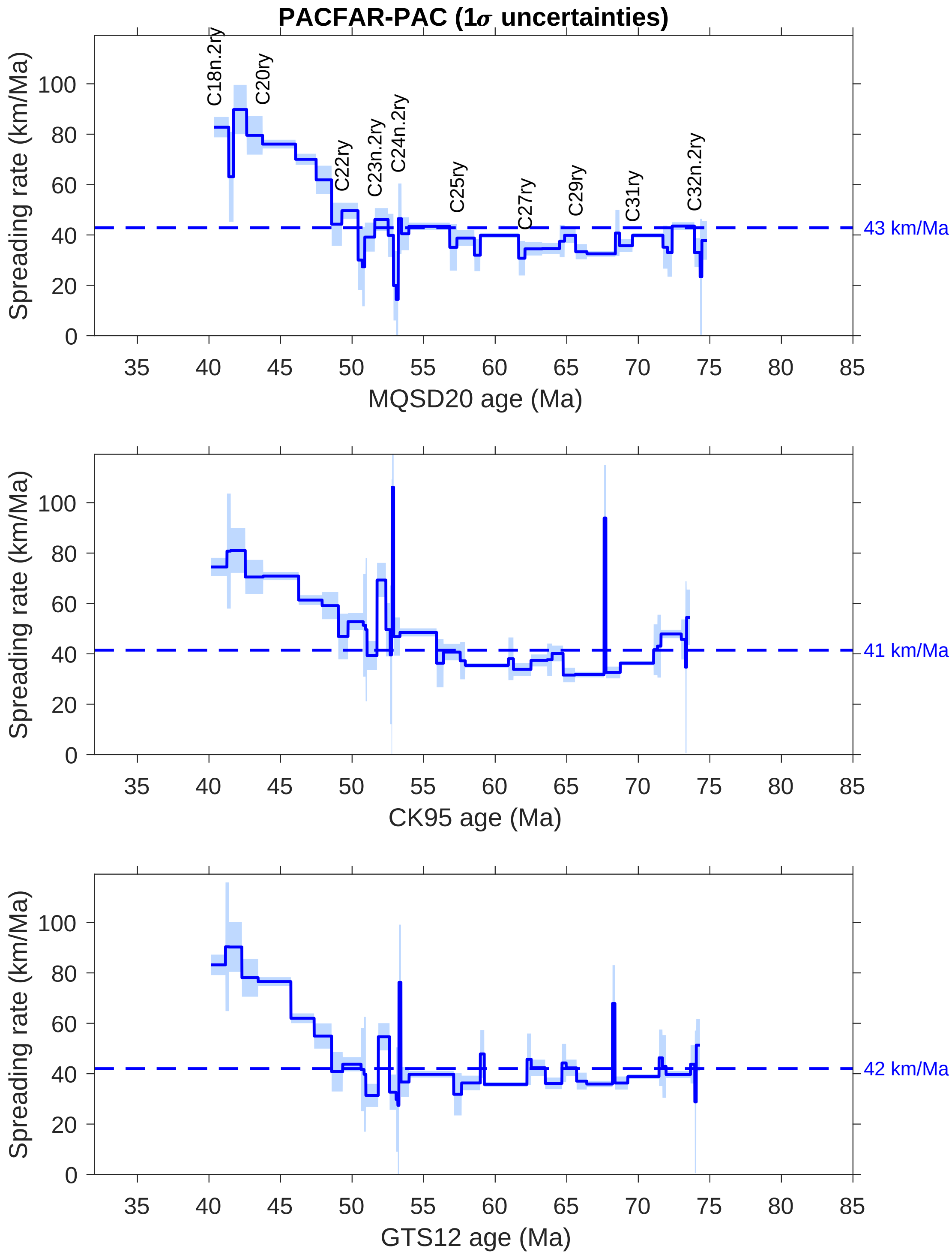

Figure S27. Half-spreading rates in the PACFAR-PAC ridge flank region for different GPTSs: MQSD20 (this paper), CK95 (Cande & Kent 1992, 1995), and GTS12 (Ogg 2012). The shaded areas show 1σ uncertainties in spreading rate, computed from the uncertainties in BMDs as the square root of the diagonal of matrix $\mathbf{C}_1$ (Equation 7).

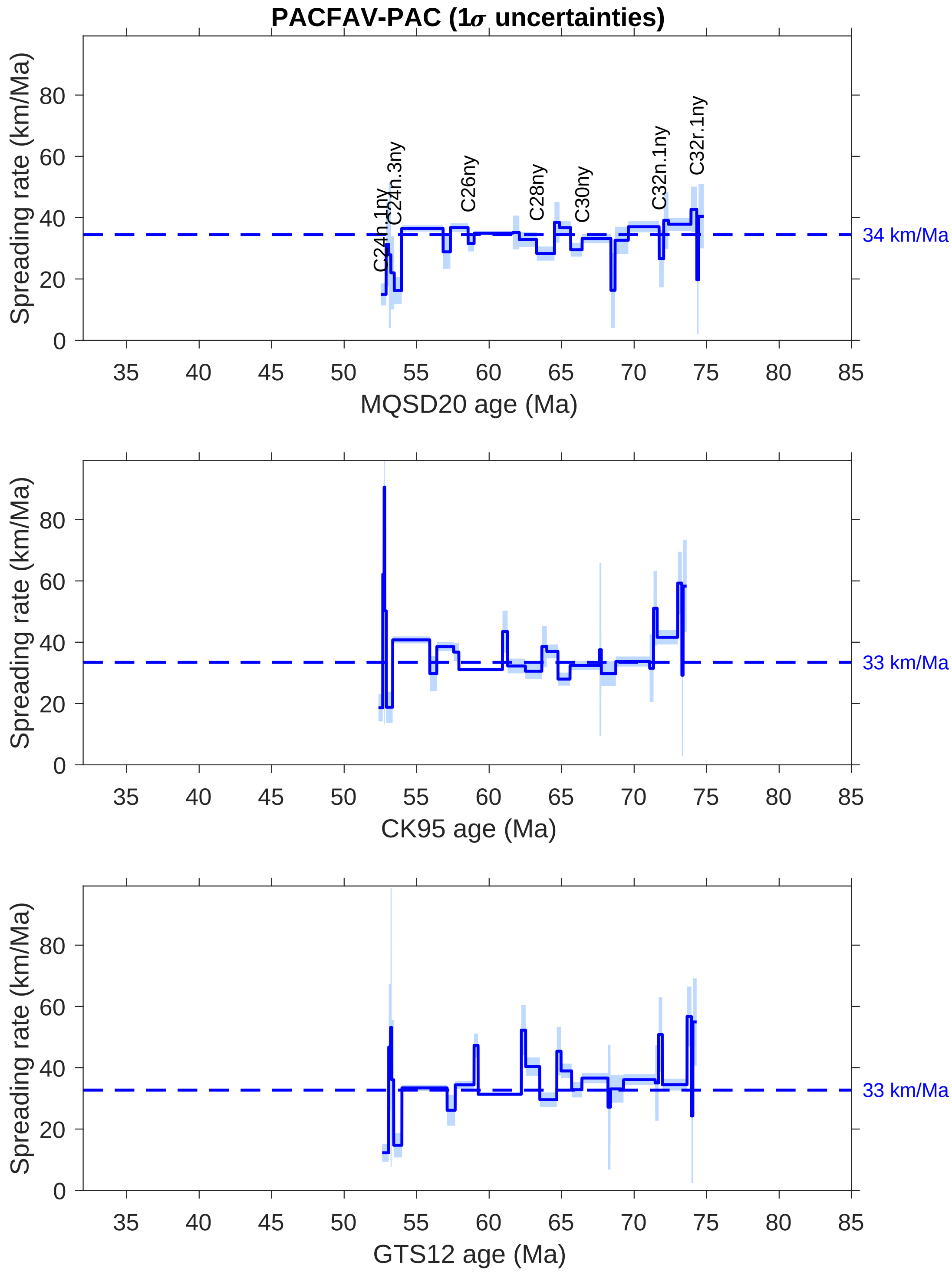

Figure S28. Half-spreading rates in the PACFAV-PAC ridge flank region for different GPTSs: MQSD20 (this paper), CK95 (Cande & Kent 1992, 1995), and GTS12 (Ogg 2012). The shaded areas show 1σ uncertainties in spreading rate, computed from the uncertainties in BMDs as the square root of the diagonal of matrix $\mathbf{C}_1$ (Equation 7).

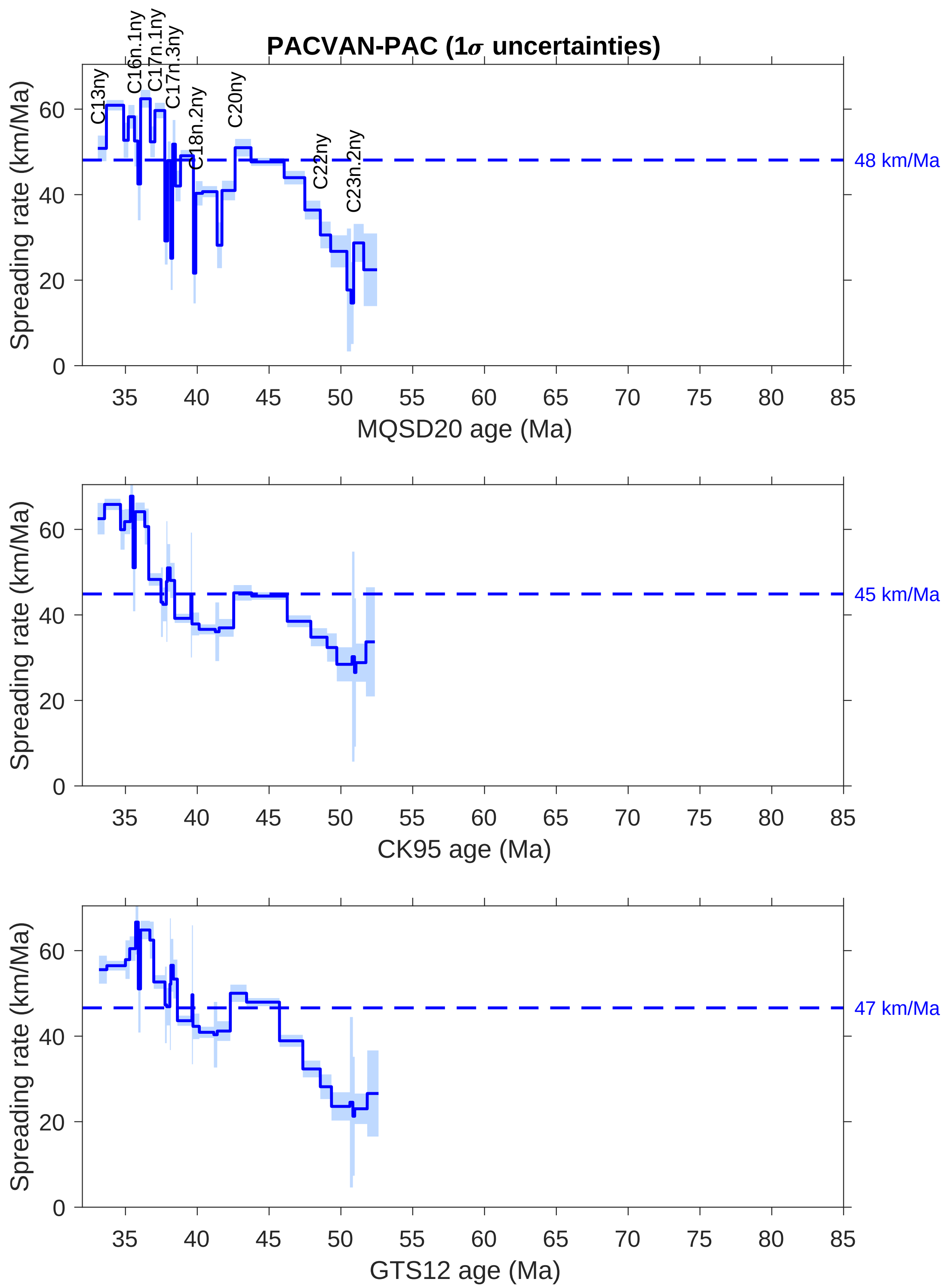

Figure S29. Half-spreading rates in the PACVAN-PAC ridge flank region for different GPTSs: MQSD20 (this paper), CK95 (Cande & Kent 1992, 1995), and GTS12 (Ogg 2012). The shaded areas show 1σ uncertainties in spreading rate, computed from the uncertainties in BMDs as the square root of the diagonal of matrix $\mathbf{C}_1$ (Equation 7).